UAB
Universitat Autònoma de Barcelona

Cross-Interactions between Amyloid-β and Endogenous Neuropeptides in Alzheimer's Amyloid Pathway

Mohsen Habibnia

ADVERTIMENT. L'accés als continguts d'aquesta tesi queda condicionat a l'acceptació de les condicions d'ús establertes per la següent llicència Creative Commons: https://creativecommons.org/licenses/?lang=ca

ADVERTENCIA. El acceso a los contenidos de esta tesis queda condicionado a la aceptación de las condiciones de uso establecidas por la siguiente licencia Creative Commons: https://creativecommons.org/licenses/?lang=es

WARNING. The access to the contents of this doctoral thesis it is limited to the acceptance of the use conditions set by the following Creative Commons license: https://creativecommons.org/licenses/?lang=en

Cross-Interactions between Amyloid-β and Endogenous Neuropeptides in Alzheimer's Amyloid Pathway

Universitat Autònoma de Barcelona
Departamento de Bioquímica y Biología Molecular
Institut de Neurociències (INc-UAB)

Doctoral Thesis presented by **Mohsen Habibnia** for the Ph.D. degree in Biochemistry, Molecular Biology and Biomedicine from the Autonomous University of Barcelona.

The research presented in this dissertation was conducted at the UAB Biophysics Unit, Faculty of Medicine, and the Institute of Neurosciences (INc-UAB), supervised by **Dr. Alex Perálvarez Marín**.

Summer 2026

Table of Contents

ACKNOWLEDGEMENTS 1

SUMMARY 2

LIST OF ABBREVIATIONS 3

GENERAL INTRODUCTION 5

1. Alzheimer's Disease 5

2. Amyloid Cascade Hypothesis 6

2.1. APP processing: Amyloidogenic vs. non-amyloidogenic pathways 7

2.2. Aβ Function 8

2.3. Aβ Clearance, degradation, and homeostasis 10

3. Tau Pathology and Aβ 12

4. What Drives Aβ Aggregation at The Molecular Level? 14

4.1. Hotspots: Aggregation-Prone Regions (APRs) 14

4.2. Aggregation-Prone Motifs: Central Hydrophobic Cluster (CHC) 15

4.3. Amyloid Core Regions 15

5. Endogenous Neuropeptides' Cross-Interactions with Aβ 16

5.1. Physiological Roles of Endogenous Neuropeptides in Brain Homeostasis and Aβ Regulation 19

5.2. Alterations in Neuropeptide Networks in Alzheimer's Disease 20

5.3. Interactions Between Neuropeptides and Aβ Aggregation Kinetics 21

6. Aβ-Induced Membrane Disruption 21

6.1. Effects of Specific Lipid Bilayers on Aβ Pore Formation 22

6.2. Biophysical Background of Aβ–Membrane Interactions 24

7. Biophysical Methodology to Study Heterotypic Cross-Interaction 25

7.1. Circular dichroism spectroscopy 25

7.2. Electron microscopy 26

7.3. Studying Amyloid-β Fibrils 26

7.4. Aggregation Kinetics: ThT Assay 27

7.5. Cell Viability: MTT Assay 30

7.6. Liposome Leakage Assay 30

GENERAL OBJECTIVES 34

CHAPTER I 36

Decoding the Molecular and Structural Determinants of the Neurokinin A and $A\beta_{42}$ Peptide Cross-Interaction in the Amyloid Cascade Pathway 36

CHAPTER II 64

Biophysical Analysis of Angiotensin II and Amyloid-β Cross-Interaction in Aggregation and Membrane Disruption 64

CHAPTER III 86

Electrostatic control of membrane disruption and amorphous coaggregation by dynorphin A variants 86

GENERAL DISCUSSION 101

1. General Discussion 101

1.1. NKA–$A\beta_{42}$: Aromatic gating of the amyloid nucleation site 102

1.2. AngII–Aβ: Vascular-amyloid crosstalk and conformation-selective modulation 104

1.3. DynA and SCA23 clinical variants: Pathological co-aggregation and synergistic membrane disruption 105

1.4. An integrated framework: Neuropeptide heterotypic interactions as gatekeepers of the amyloid cascade 108

CONCLUSIONS 112

Chapter I: Heterotypic interaction between Neurokinin A and amyloid-β42 112

Chapter II: Heterotypic interaction between Angiotensin II and amyloid-β peptides 113

Chapter III: Heterotypic interaction between Dynorphin A variants and amyloid-β42 115

General conclusions 117

FUTURE PERSPECTIVES 118

REFERENCES 120

ACKNOWLEDGEMENTS

I would like to express my deepest gratitude to my supervisor, **Dr. Alex Perálvarez Marín**, whose unwavering guidance, insightful feedback, and constant encouragement shaped every stage of this research. I am indebted to my doctoral committee members, **Dr. Josep B Cladera**, **Dr. Irantzu Pallares Goitiz**, and **Dr. Marc Torrent Burgas**, for their constructive criticism and expert perspectives that strengthened this work.

My sincere thanks also go to my colleagues and lab mates in the **APM Lab**, as well as **Dr. Ramon Bandras**, **Dr. Nuria Benseny Cases**, and **Dr. David Garcia Quintana** for the stimulating discussions, technical assistance, and shared moments that made the journey both productive and enjoyable.

On a personal note, I owe an immense debt to **my family** for their endless patience, love, and belief in me even during the most challenging periods.

SUMMARY

Central to the Alzheimer's Disease pathogenesis is the amyloid cascade hypothesis, a process which involves the deposition of insoluble amyloid-beta (Aβ) peptides into senile plaques. Aβ does not aggregate in a vacuum; it shares its anatomical and physiological niche with a multitude of neuropeptides and proteins, and engages in specific, heterotypic cross-interactions with these endogenous bioactive peptides. Some of these peptides function as "anti-amyloidogenic" chaperons and exert neuroprotective effects against the Aβ-induced toxicities, and some may act as "pro-amyloidogenic" factors and accelerate the aggregation.

In this Ph.D. Thesis, the heterotypic cross-interactions of Aβ with different endogenous neuropeptides, including Neurokinin A and its variant NKW, Angiotensin II, and Dynorphin A and its SCA23-linked clinical variants (L5S, R6W, R9C), have been characterized by various methodologies to examine the biophysical principles governing these interactions.

LIST OF ABBREVIATIONS

ACE	Angiotensin converting enzyme
ACEI	Angiotensin-converting enzyme inhibitor
ACH	Amyloid cascade hypothesis
ACF	Autocorrelation function
AD	Alzheimer's Disease
AICD	Amyloid precursor protein intracellular domain
AngII	Angiotensin II
ANOVA	One-way analysis of Variance
APOE	Apolipoprotein E
APP	Amyloid precursor protein
APR	Aggregation-prone regions
ARB	Angiotensin receptor blocker
Aβ	Amyloid-β
BACE1	β-secretase
BBB	Blood-brain barrier
BDNF	Brain-derived neurotrophic factor
BigDyn	Big dynorphin
CAA	Cerebral amyloid angiopathy
CD	Circular dichroism
CHC	Central hydrophobic cluster
Chol	Cholesterol
CNS	Central nervous system
CPP	Cell penetrating peptides
CSF	Cerebrospinal fluid
CTF83	C-terminal fragment 83
CTFβ (C99)	99-residue C-terminal fragment of APP
CtHSA	Serum albumin C-terminus fragment
CysC	Cystatin C
DLS	Dynamic light scattering
DMSO	Dimethyl Sulfoxide
DPX	p-xylene-bis-pyridinium bromide
DynA	Dynorphin A
ECE1	Endothelin-converting enzyme 1
ECE2	Endothelin-converting enzyme 2
ECL	Extracellular loop
EM	Electron microscopy
EOAD	Early-onset Alzheimer's Disease
ER	Endoplasmic reticulum
GHSR	Growth hormone secretagogue receptor
GPCR	G-protein coupled receptor
HK1	Hemokinin1

IDE	Insulin-degrading enzyme
KPI	Kunitz protease inhibitor
LOAD	Late-onset Alzheimer's Disease
LRP1	Lipoprotein receptor-related protein 1
LUV	Large unilamellar vesicle
MAPT	Microtubule-associated protein tau
MD	Molecular dynamic
MTT	3-(4,5-dimethylthiazol-2-yl)-2,5-diphenyltetrazolium bromide
NEP	Neprilysin
NFT	Neurofibrillary tangle
NKA	Neurokinin A
NKB	Neurokinin B
NK2R	Type 2 neurokinin receptor
NMR	Nuclear magnetic resonance
NPY	Neuropeptide Y
PACAP	Pituitary adenylate cyclase-activating polypeptide
PC2	Proprotein convertase
PDB	Protein data bank
PDI	Polydispersity index
PDYN	Prodynorphin gene
Phe	Phenylalanine
POPC	1-palmitoyl-2-oleoyl-sn-glycero-3-phosphocholine
POPG	1-Palmitoyl-2-Oleyol-sn-Glycerol-3-[Phosho-rac-(1-glycerol)]
PS1	Presenilin 1 gene
PS2	Presenilin 2 gene
RAS	Renin-angiotensin system
RAGE	Receptor for advanced glycation end products
REU	Rosetta energy units
RFU	Relative fluorescence unit
ROSIE	Rosetta Online Server
sLRP1	Soluble lipoprotein receptor-related protein 1
SDS	Sodium dodecyl sulfate
SEC	Size-exclusion chromatography
SEM	Scanning electron microscopy
SH-S5Y5	Human Neuroblastoma cell line
SP	Substance P
SST	Somatostatin
TAC1	Preprotachykinin A
TAC3	Preprotachykinin B
TEM	Transmission electron microscopy
ThT	Thioflavin T
TKs	Tachykinins
TX100	Triton X-100
VCD	Vibrational circular dichroism
VIP	Vasoactive intestinal peptide

GENERAL INTRODUCTION

1. Alzheimer's Disease

Alzheimer's disease (AD) is a catastrophic neurodegenerative disorder and the most prevalent form of elderly dementia affecting more than 50 million people worldwide[1,2]. In 1907, Alois Alzheimer, described presenile dementia for the first time with senile plaques and neurofibrillary tangles the key pathological hallmarks of AD. AD is accumulative, irreversible, and lethal which slowly leads to a cluster of prefrontal syndrome symptoms starting with memory loss, followed by language disturbances and other cognitive impairments, and finally, lucid dementia[3] accompanying neuropsychiatric symptoms such as depression and psychosis[4]. The widespread appearance of this disease is sporadic AD that is categorized as late-onset AD (LOAD)[5]. Only a small percentage (5%) of the AD cases is autosomal dominant early-onset familial AD (EOAD) and it's an outcome of mutations in Amyloid precursor protein gene (APP,21q21.3), presenilin 1 gene (PS1, 14q24.2), and presenilin2 gene (PS2, 1q42.13) along with the ε4 allele of Apolipoprotein E inheritance[6,7]. Tau protein is also altered in inherited AD[8].

Two classical lesions of AD neuropathogenesis are the intracellular misfolding depositions of hyperphosphorylated tau protein into neurofibrillary tangles (NFTs)[9,10] and the overexpression and accumulation of extracellular amyloid-β (Aβ) peptide into senile plaques mainly located in the hippocampus and neocortex[11]. The NFTs largely consist of hyperphosphorylated twisted filaments of the microtubule-associated protein tau (MAPT). NFTs together with Aβ plaques trigger neuronal loss, mitochondrial disturbance, synaptic alteration, and blood-brain barrier (BBB) dysfunction[12–15].

Understanding these molecular underpinnings is crucial for developing targeted diagnostic and therapeutic strategies. This introduction will delve into the biochemical and biophysical aspects

of AD, with a particular focus on the amyloid cascade hypothesis and its implications for disease progression. Central to this understanding is the abnormal processing of amyloid precursor protein, which leads to the accumulation and aggregation of Aβ peptides[16].

2. Amyloid Cascade Hypothesis

In the early 1980s, researchers recognized analogies between amyloid depositions in AD patients and proteinopathy in Creutzfeldt-Jakob disease. Cerebrovascular amyloid peptides of AD and Down syndrome patient were purified and sequenced which showed that both amyloid share the same primary sequence of β-protein predicting a genetic risk locus at chromosome 21[17]. After $A\beta_{40}$ plaque purification and the characterization of its N-terminal sequence[18], the first reports of Aβ cytotoxicity were published[19], which led to the formation of the amyloid cascade hypothesis (ACH) by Hardy and Higgins in 1992 proposing that ACH is a fundamental theory in AD research with Aβ deposition in the brain parenchyma being a central event driving AD pathology[11]. Genetic mutations of the APP, PS1, and PS2 genes linked to the familial AD, affecting the presence of Aβ within senile plaques, supported the ACH, where accumulation of Aβ starts a chain of reactions that end up in NFTs, synaptic dysfunction, neuronal loss, and ultimately cognitive decline and dementia[11,20,21].

From a biophysical standpoint, AD is a protein misfolding disease in which intrinsically disordered or metastable proteins adopt β-sheet-rich insoluble oligomeric and fibrillar conformations that self-assemble into ordered supramolecular structures. The kinetics of nucleation, growth, and fragmentation of Aβ and tau assemblies, governed by physico-chemical parameters such as concentration, pH, ionic strength, lipid composition, and metal ions, plays a critical role in determining toxicity and spatial spread[22,23].

2.1. APP processing: Amyloidogenic vs. non-amyloidogenic pathways

Aβ, as an ancient neuropeptide, is highly conserved across vertebrate taxa over 400 million years[24]. The human Aβ sequence has crucial biological functions. Under normal neurophysiological conditions, endogenous Aβ exists in monomeric forms at picomolar to nanomolar concentrations playing a key role in activation of intracellular signaling in neurotransmission, regulation of excitation/inhibition balance, also in synaptic vesicle trafficking[25]. In the CREB-mediated pathways, Aβ monomers initiate the brain-derived neurotrophic factor (BDNF) axis which is involved in hippocampal neurogenesis. Furthermore, the Aβ released in the synaptic cleft is engaged in neuronal bioenergetic levels sustainment, important for a proper synaptic activity[26].

Dementia Aβ, is 40/42-residue segment of the brain transmembrane protein APP[27] widely produced by neurons, blood cells, and to a lesser extent by astrocytes. The APP gene, the precursor of Aβ, is located on chromosome 21 in humans with three major isoforms; APP695, APP751, and APP770 which APP751 and APP770 contain a 56 amino acid Kunitz Protease Inhibitor (KPI) domain within their extracellular regions[28]. The protein and mRNA levels of KPI-containing APPs are associated with increased Aβ deposition and up regulated in AD brains. APP is primarily matured in the endoplasmic reticulum and the Golgi apparatus, then it is translocated to the cell surface, where it enters the lysosomal pathway and undergoes the proteolytic degradation[29].

In the non-amyloidogenic pathway, APP is cleaved by α-secretase, a membrane-bound zinc metalloprotease from the ADAM (a disintegrin and metalloproteinase) family, in the center of the sequence between the 16th (Lys) and the 17th (Leu) residues generating the soluble N-terminal 105-125kDa fragment of sAPPα and a 10 kDa cell-membrane-bound C-terminal fragment 83

(CTF83) which later is cleaved to p3 and amyloid precursor protein intracellular domain (AICD) by γ-secretase[30,31].

In the amyloidogenic pathways, two subsequent proteolytic cleavages of APP gene by β-secretase (β-APP-cleaving-enzyme-1, BACE1) and γ-secretase generate Aβ. APP is first cleaved by BACE1 at the ectodomain generating sAPPβ and the 99-residue C-terminal fragment of APP (CTF-β or C99) which remains bound to the membrane. C99 is then processed by γ-secretase within its transmembrane segment to yield Aβ peptides of varying lengths, predominantly $A\beta_{40}$, the majority species, and $A\beta_{42}$, the more amyloidogenic species along with the intracellular domain of APP (AICD)[32–35].

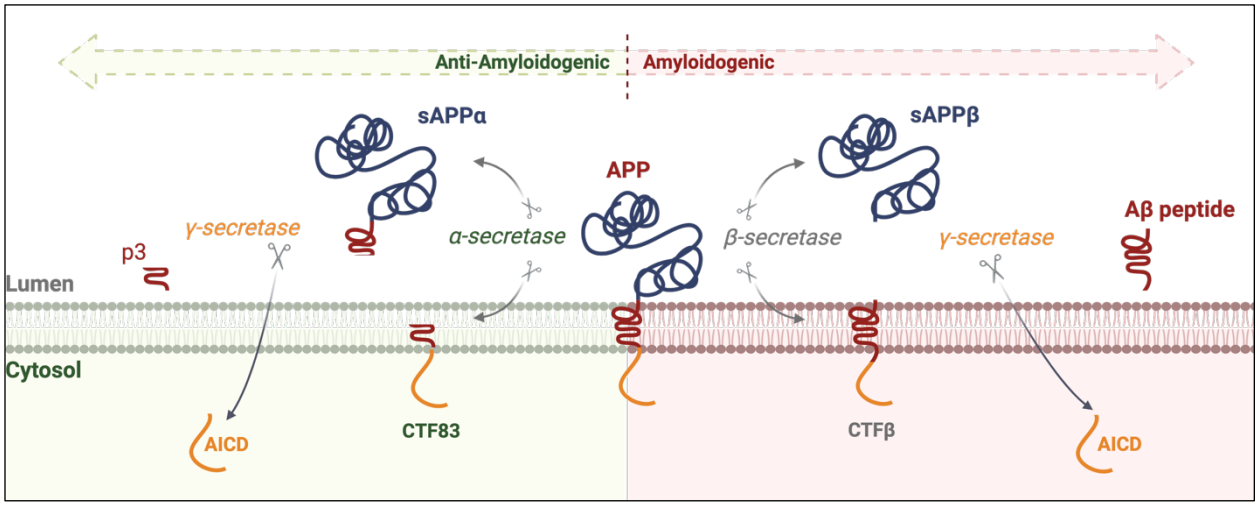


Figure 1. Schematic illustration of APP processing. (Designed using Biorender.com).

2.2. Aβ Function

Overproduction of Aβ leads to a neurodegenerative cascade resulting in formation of NFTs, synaptic dysfunction, and lastly neuronal loss. Aβ monomers self-assemble and organize β-sheet-rich oligomers also known as Aβ assemblies, which are further aggregated to soluble protofibrils. At this stage, insoluble β-sheet fibrils are generated as the result of protofibril accumulation. Afterwards, Aβ peptides flock together and give rise to the AD neuropathological hallmark, Aβ

plaques[11,18,36,37]. These aggregation species of Aβ hold a steady state with the bidirectional conversion of one form to another. Amyloid fibrils are well-ordered cross β-sheet structures that exist in parallel and antiparallel patterns of sheet symmetry. All the amyloid fibrils share a cross-β paternal motif that consists of serial peptide units perpendicularly positioned to the fiber axis, as well as their intermolecular hydrogen bonds between paired carbonyl and amide groups in β-strand[38,39]. Two main isoforms of Aβ are, soluble $Aβ_{40}$ and insoluble $Aβ_{42}$ generating more than 90% and less than 5% of Aβ forms in a normal neurophysiological condition, respectively[40]. In contrast, $Aβ_{42}$ is more amyloidogenic than $Aβ_{40}$ due to a reduction in its C-terminal flexibility via a β-hairpin formation by its 31-34 and 38-41 residues. $Aβ_{42}/Aβ_{40}$ ratio is increased in the brains of patients suffering from AD[41,42] and AB_{42} clearance is reduced in cerebrospinal fluid (CSF)[43]. Aβ are generally tracked in vitro by fluorescent dye probes Thioflavin T and Congo red via a change of their optical properties when bound to Aβ[44]. There are many common non-negligible factors among the proposed hypotheses for the key pathological features exaggerating the progression of AD such as oxidative stress[45], neuroinflammation[9], ions homeostasis dysregulation[46], decrease in glucose metabolism[47].

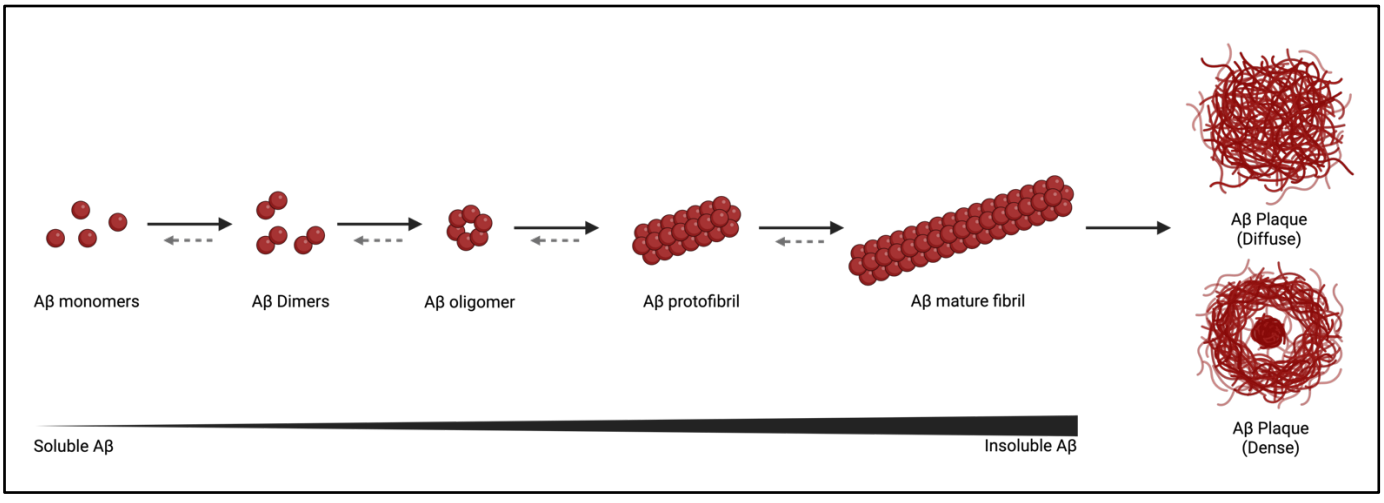


Figure 2. Conversion of Aβ from monomers to senile plaques. (Created using Biorender.com).

2.3. Aβ Clearance, degradation, and homeostasis

The imbalance between the production and clearance of Aβ is considered a major causative factor in the pathogenesis of AD. Aβ removal involves many pathways including enzymatic degradation, receptor-mediated transport across the BBB, and peripheral clearance mechanisms, highlighting their interconnectedness and therapeutic potential[48,49]. The interplay between these clearance pathways is crucial for maintaining Aβ homeostasis, and dysfunction in any one pathway can contribute to the pathological accumulation observed in AD[50]. Given that approximately 60% of brain-derived Aβ is cleared via peripheral mechanisms, the liver is particularly important in removing Aβ from circulation through protein degradation and bile excretion, thereby preventing its cerebral buildup[51]. The liver's capacity for Aβ clearance is significantly mediated by lipoprotein receptor protein-1, which efficiently removes 70–90% of circulating Aβ, thus preventing its pathological accumulation in the brain[52,53].

Enzymatic degradation represents a primary central mechanism for Aβ removal within the brain parenchyma. Key proteases such as neprilysin (NEP) and insulin-degrading enzyme (IDE) cleave monomeric Aβ peptides into smaller, non-toxic fragments, preventing their aggregation into oligomers and plaques. NEP, a membrane-bound metallopeptidase, degrades both monomeric and some oligomeric forms of Aβ, while IDE primarily targets soluble Aβ species. Other enzymes, including endothelin-converting enzymes (ECE1 and ECE2), also contribute to this process. Impairments in these enzymes, due to aging, genetic factors, or disease, reduce Aβ breakdown and exacerbate accumulation, underscoring their therapeutic relevance through strategies aimed at upregulating their expression or activity[54–56].

Receptor-mediated transport across the BBB provides another critical pathway, balancing Aβ influx and efflux. Low-density lipoprotein receptor-related protein 1 (LRP1), expressed on the

abluminal side of brain endothelial cells, facilitates the rapid efflux of Aβ from the brain interstitial fluid into the peripheral circulation. This process is often disrupted in AD, where reduced LRP1 expression contributes to impaired clearance. Conversely, the receptor for advanced glycation end products (RAGE) mediates Aβ influx from blood to brain, and its upregulation in AD promotes further cerebral deposition. The dynamic equilibrium between LRP1-mediated efflux and RAGE-mediated influx helps regulate brain Aβ levels under normal conditions, but shifts toward influx in disease states highlight the potential of modulating these receptors such as enhancing LRP1 or inhibiting RAGE to restore homeostasis[57–60].

Peripheral clearance mechanisms complement central pathways by acting as a "sink" for brain-derived Aβ once it enters the bloodstream. Approximately 40–60% of brain-produced Aβ is eliminated peripherally, with the liver emerging as the dominant organ responsible for systemic catabolism. Hepatocytes uptake circulating Aβ primarily via LRP1, leading to intracellular degradation or excretion into bile. This hepatic process prevents re-entry of Aβ into the brain and maintains low plasma levels of free Aβ. Soluble LRP1 (sLRP1) in plasma further supports this by binding 70–90% of circulating Aβ, sequestering it and inhibiting its return across the BBB. Additional peripheral contributions include kidney filtration of soluble Aβ and enzymatic degradation in other organs, but the liver's role is paramount. Dysfunction in peripheral clearance such as reduced hepatic LRP1 in conditions like non-alcoholic fatty liver disease or aging, correlates with elevated plasma Aβ, increased cerebral deposition, and accelerated AD pathology[51,61].

Endogenous neuropeptides serve as substrates for NEP and similar enzymes, creating a link between neuropeptide metabolism and Aβ homeostasis. Neurokinin A (NKA) indirectly supports Aβ degradation by chelating metal ions (Cu^{2+}, Zn^{2+}) that promote Aβ misfolding and aggregation.

Metals like copper exacerbate Aβ toxicity by inducing oxidative stress and stabilizing oligomers; NKA's chelation reduces this, facilitating access for degrading enzymes such as NEP or IDE. Angiotensin II (AngII) indirectly influences degradation by modulating enzymes like ACE and NEP. Dynorphin A (DynA) indirectly aids degradation by stabilizing Aβ in less aggregated forms, making it more accessible to IDE or NEP.

NKA promotes clearance by its hydrophobic nature allowing it to BBB, where it may enhance Aβ efflux via receptors like LRP1. AngII modulates clearance through vascular and cellular pathways. AT1 receptor blockade improves BBB integrity and glymphatic flow, enhancing Aβ efflux from the brain. In AD models, ACE-overexpressing monocytes increase Aβ phagocytosis, reducing parenchymal and vascular burden by 47-82%. AngII itself reduces Aβ-induced membrane disruption in liposomes, aiding cellular uptake and lysosomal clearance. Big dynorphin (BigDyn) enhances clearance by hindering Aβ aggregate formation, potentially facilitating microglial uptake[62–65].

3. Tau Pathology and Aβ

Tau pathology, a hallmark of AD alongside Aβ plaques, involves the abnormal hyperphosphorylation, misfolding, and aggregation of the microtubule-associated protein tau into NFTs and neuropil threads within neurons. Neurophysiologically, tau stabilises microtubules, facilitating axonal transport and neuronal integrity, but in AD, pathological modifications driven by kinases like GSK-3β and CDK5 lead to three interrelated processes: 1- loss of microtubule stabilizing function, 2- gain of toxic functions through soluble tau oligomers, and 3- propagation of aggregated tau species via prion-like seeding and spreading along neuronal networks. This pathology correlates strongly with cognitive decline, synaptic loss, and neurodegeneration,

progressing in a stereotypical Braak staging pattern from the entorhinal cortex to neocortical regions[66,67].

The relationship between tau pathology and Aβ is bidirectional and central to the amyloid cascade hypothesis, where Aβ accumulation acts as an upstream trigger for tau dysregulation through independent and synergistic contributions. Aβ oligomers promote tau hyperphosphorylation by activating stress kinases and disrupting phosphatase activity, facilitating tau detachment from microtubules and its aggregation. Conversely, pathological tau can potentiate Aβ toxicity by impairing Aβ clearance mechanisms, such as reduced lysosomal function in affected neurons, and by promoting synaptic dysfunction that exacerbates Aβ-induced excitotoxicity[67]. Studies indicate that soluble tau species in CSF correlate with Aβ plaques, with plasma biomarkers like pTau217 reflecting both phosphorylated soluble tau in the context of Aβ pathology and aggregated tau, providing diagnostic utility for early AD detection[68]. Therapeutically, the evolving landscape of AD treatments builds on Aβ successes, with tau-targeted strategies gaining momentum. Protein based approaches include albumin backboned therapies that antagonize tau pathology by stabilizing microtubules and reducing Aβ-tau interactions, as well as interventions targeting downstream effects like neuroinflammation[69].

Apolipoprotein E (APOE), particularly the ε4 isoform, plays a pivotal role in Aβ aggregation by binding to Aβ peptides and modulating their clearance through cell-surface receptors such as LRP1, LDLR, and HSPG in an isoform-dependent manner, with APOEε4 impairing Aβ clearance at the BBB and promoting perivascular deposition, thereby facilitating the formation of amyloid plaques and cerebral amyloid angiopathy (CAA)[70]. This interaction between APOEε4 and Aβ extends to tau pathology, where APOEε4 carriership potentiates Aβ-driven longitudinal tau accumulation, as evidenced by increased tau-PET burden in temporal regions over time,

mediated partly by rises in plasma phosphorylated tau at threonine 217 (p-tau217)[71]. For equivalent Aβ levels, APOEε4 carriers exhibit heightened tau aggregation in regions of high APOE mRNA expression, such as temporal lobes, with sex-specific amplifications in females, underscoring localized vulnerabilities that link APOE genotype to the interplay between Aβ and tau pathologies in AD progression[72].

4. What Drives Aβ Aggregation at The Molecular Level?

A complex interplay of sequence-specific regions and external factors including certain "hotspots" drive the aggregation of Aβ at the molecular level which their mechanisms of action are articulated in this section.

4.1. Hotspots: Aggregation-Prone Regions (APRs)

Two primary APRs in Aβ; APR1 (residues 16–21, KLVFFA) and APR2 (C-terminal, LVFFAE), which are hydrophobic and β-sheet-prone, are identified to drive self-assembly. Selective interactions at these APRs, with early oligomers binding APR1 and later seeds engaging both. Homologous peptides (with up to two mismatches to APR sequences) modify $A\beta_{42}$ aggregation, some accelerate the lag phase, others delay it or alter the fibril yield. In cellulo, HEK293T cells expressing mCherry-$A\beta_{42}$ formed aggregates when co-expressed with APR-homologous proteins, reducible by homolog removal. These findings suggest APRs act as hotspots by facilitating heterotypic interactions that modulate assembly kinetics and structure, potentially explaining human-specific plaque composition. Hotspots in residues 16-21 and 30-42, with mutations like E22G accelerate fibrillization by increasing aggregation propensity. This underscores APRs' role in nucleation from unfolded states[73,74].

4.2. Aggregation-Prone Motifs: Central Hydrophobic Cluster (CHC)

CHC amino acid propensities, with hydrophobic residues (Ile, Phe, Val, Leu) promote aggregation via interactions, while polar ones (Asp, Glu, Asn, Arg) enhance solubility. CHC overlaps with hotspots 16-21 and 30-42, showing these in fibril cores and fibril formation by fragments like 16-22. Aβ monomers favor β-hairpin via CHC-C-terminal interactions, with β-strand probabilities rising from 19% in monomers to 30% in tetramers. Transitions from polyproline II-helix to β-strands take place nucleated by a protease-resistant turn (residues 21-30). CHC motifs drive oligomer growth isotopically up to tetramers, then linear, diverging Aβ40/42 pathways toward toxic species[75,76].

4.3. Amyloid Core Regions

Amyloid cores as stable β-sheet-rich segments, with variability in flanking areas enable polymorphism. Cross-interactions with partners like insulin incorporated Aβ into hetero-fibrils, altering kinetics (shorter lag phases) and morphologies. Aβ residues 15-17 and 34-36 in cores during hetero-assembly, influence AD pathogenicity[77].

Antiparallel β-sheets in oligomers (≥4 strands), transitioning to parallel in fibrils, with S-shaped protofilaments. C-terminal residues (Ile-Ala) mediate viral/bacterial aggregation with fragments like Aβ35-42 retaining activity via oligomerization[78].

The biophysical behavior of these motifs is profoundly modulated by the local environment. Aβ exists in a state of "molecular frustration" where the transition to a β -sheet is often preceded by a transient α-helical intermediate[79]. The stability of these intermediates is influenced by environment physicochemical features such as pH[80], ionic strength[81], and even the neuropeptides' interaction with lipid membranes and surfactants[82]. Research in membrane-

mimetic environments has shown that the "local context", such as the presence of specific surfactants or lipid bilayers, can either sequester the hydrophobic APRs or, conversely, act as a scaffold to accelerate their assembly[83,84]. This membrane-mediated folding is a key determinant in how transitions from a disordered state to a membrane-disrupting oligomer[85]

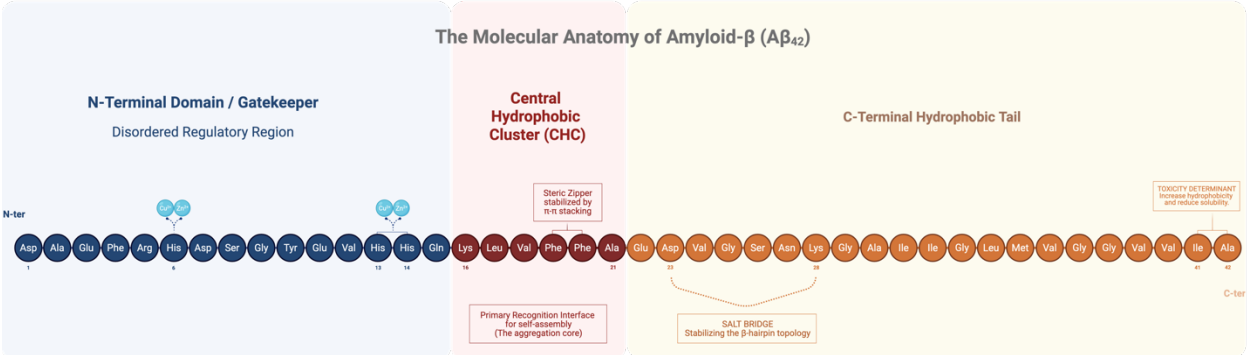


Figure 3. The molecular anatomy of Aβ42. (Designed using Biorender.com).

5. Endogenous Neuropeptides' Cross-Interactions with Aβ

Endogenous neuropeptides are small protein-like molecules synthesized by neurons and secreted to the synaptic space to modulate wide arrays of physiological functions within the CNS and periphery. These bioactive peptides, typically ranging from 3 to 100 amino acid residues in length, act as neurotransmitters, neuromodulators, or neurohormones, influencing synaptic transmission, neuronal excitability, neuroplasticity, inflammation, and homeostasis[65]. In the brain, neuropeptides are stored in large dense-core vesicles and released in response to specific stimuli, often exerting long-lasting effects compared to classical neurotransmitters. Key examples include somatostatin (SST), neuropeptide Y (NPY), substance P (SP), ghrelin, neurotensin, pituitary adenylate cyclase-activating polypeptide (PACAP), orexin, leptin, cerebellin, angiotensin II (AngII), dynorphins, and tachykinins[62]. Their receptors, predominantly GPCRs, are distributed across neurons, glia, and endothelial cells, enabling multifaceted signaling cascades that regulate cellular survival, protests, and metabolic processes[64].

Emerging evidence positions endogenous neuropeptides at the crossroads of AD pathogenesis, particularly in modulating Aβ dynamics. Some neuropeptides exert neuroprotective effects by enhancing Aβ clearance[86], inhibiting aggregation[87], promoting synaptic plasticity[88], and mitigating oxidative stress and inflammation[89]. Conversely, disruptions in neuropeptide networks such as reduced levels or impaired signaling, exacerbate Aβ pathology, contributing to onset or disease progression[62,64,90]. This intricate interplay underscores the potential of neuropeptides as biomarkers and therapeutic targets.

When cross-interacting with Aβ, certain neuropeptides deploy neuroprotective effects and ameliorate AD by suppressing Aβ aggregation. The majority of these so-called "anti-amyloidogenic neuropeptides" come along with the ability to cross the BBB[91] which together with their neuroprotective effects make them and/or their variants important candidates for prospective AD theragnostic approaches.

Table 1. Mechanisms of Neuropeptide-Aβ Cross-Interactions.

Interactor	Primary Mechanism	Biophysical Effect	Outcome	REF
SST14	Oligomer-selective binding (Trp8 anchor)	Caps pore-forming tetramers	**Inhibits Toxicity**	92,93
Cystatin C (CysC)	Monomer sequestration (via residues 101-117)	Competes with CHC (KLVFFA) Remodels fibrils	**Inhibits Aggregation**	94,95
NKB	Metal Chelation (ATCUN motif)	Sequesters Cu/Ni Prevents metal-induced aggregation	**Inhibits Toxicity**	96
NKA	Aromatic/Hydrophobic/Electrostatic interaction	Prevents the initial seeding process (Aß dimers)	**Inhibits Toxicity**	97

BigDyn	Electrostatic/Hydrophobic interaction	Stabilizes non-toxic α-helical conformation	**Inhibits Toxicity**	98
SP	Co-assembly	Forms mixed amyloid-like fibrils Downregulates Kv4 channels	**Modulates Toxicity** (Protective sequestration vs. co-aggregation)	99,100
Ang II	Direct interaction with disordered conformers	Suppresses membrane disruption	**Inhibits Toxicity**	101
VIP	Enhances microglial phagocytosis	IncreasesPKC-dependent phagocytosis of $A\beta_{42}$ Reduces microglial neurotoxic factors	**Attenuates amyloid deposition, Inhibits toxicity**	102
Orexin	Modulation of sleep-wake cycle	Increases wakefulness leading to elevated ISF Aβ levels	**Modulates Toxicity**	103
NPY	Neuroprotective binding and signaling	Reduces Aβ-induced oxidative stress	**Inhibits Toxicity**	104
CCK	Modulation of synaptic vesicle release and neuroprotection	Enhances synaptic vesicle clustering	**Inhibits Toxicity**	105
Oxytocin	Attenuation of microglial activation	Reduces Aβ oligomer-induced inflammation Decreases Aβ deposition and tau phosphorylation	**Restores Cognitive Function**	106
Vasopressin	Direct neuroprotective interaction (via V1a receptor)	Prevents Aβ-induced LTP impairment	**Inhibits Toxicity**	107
Galanin	Direct binding to Aβ Anti-apoptotic signaling	Inhibits Aβ-Induced neuronal death	**Inhibits Toxicity**	108
Adiponectin	Receptor-mediated signaling (AdipoR1/2)	Suppresses Aβ accumulation and tau hyperphosphorylation	**Reduces Cognitive Decline**	109

Apelin-13	Anti-inflammatory and anti-apoptotic interaction	Inhibits Aβ-induced autophagy and oxidative stress	**Improves Memory**	110

5.1. Physiological Roles of Endogenous Neuropeptides in Brain Homeostasis and Aβ Regulation

Endogenous neuropeptides maintain brain homeostasis by regulating neuronal communication, glial responses, and vascular integrity[111]. Big dynorphin, a 32 residues peptide, acts as an endogenous agonist at kappa opioid receptors, contributing to nociception[98]. SST which is consisted of 14- or 28-amino acid, primarily expressed in GABAergic interneurons, inhibits growth hormone release and modulates neurotransmission via SSTR1-5 receptors. In healthy brains, SST upregulates NEP activity through SSTR2 and SSTR4, facilitating Aβ degradation[112]. Similarly, NPY, a 36-amino acid peptide co-localized with SST in interneurons, promotes neuronal survival via Y1-Y5 receptors, activating PI3K/Akt, MAPK/ERK, and p38K pathways that enhance proteostasis and reduce oxidative stress[104]. SP, an 11-amino acid tachykinin, acts via NK1 receptors to regulate pain, inflammation, and vasodilation, while also influencing Aβ clearance[113].

Other neuropeptides like ghrelin consisted of a 28-amino acid hunger hormone, binds growth hormone secretagogue receptor (GHSR) to increase neuronal glucose transport and neurotrophin production. Neurotensin, a 13-amino acid peptide, modulates dopamine signaling and inhibits endoplasmic reticulum (ER) stress[114]. PACAP, a 27- or 38-amino acid peptide related to vasoactive intestinal peptide (VIP), activates PAC1, VPAC1, and VPAC2 receptors to enhance hippocampal LTP and reduce autophagy[115]. Orexin (hypocretin), comprising orexin-A and -B, maintains wakefulness and influences Aβ levels[116]. AngII, an 8-amino acid peptide of the renin-angiotensin system (RAS), reduces Aβ aggregation and membrane disruption in vitro[101].

In Aβ context, these neuropeptides regulate production, clearance, and aggregation. Physiological Aβ acts as an endogenous scavenger of transition metals (Cu, Zn), reducing oxidative stress, and protects against excitotoxicity via sequences like KLVFF (Aβ16-20)[117–119]. Neuropeptides enhance this by promoting Aβ degradation; NEP cleaves Aβ at multiple sites, and its substrates include SST[120], SP[121], and NPY fragments[122]. NEP deficiency elevates Aβ, impairing cognition[123], while SST infusion restores NEP expression[120]. NPY fragments from NEP processing are neuroprotective, reducing Aβ-induced toxicity[122].

5.2. Alterations in Neuropeptide Networks in Alzheimer's Disease

Postmortem studies reveal widespread reductions in neuropeptide levels and receptors in AD brains. SST levels decrease in cortex and hippocampus, correlating with Braak stages, due to selective loss of SST-positive interneurons. This impairs NEP upregulation, fostering Aβ accumulation. Infusion of Aβ disrupts SST signaling, creating a vicious cycle. NPY levels are reduced in AD cortex but increased in some mouse models, with Y1 receptor downregulation exacerbating neurodegeneration. SP levels decline in AD patients, though elevated in certain models, linked to neuroinflammation via NK1 activation[62,124].

Ghrelin signaling is impaired, with reduced GHSR expression contributing to metabolic dysregulation and increased Aβ production[125]. Neurotensin decreases, heightening ER stress and autophagy, which promote Aβ oligomerization[126]. PACAP levels drop, impairing LTP and neurotrophin production[127]. Orexin deficiency in APP/PS1 mice reduces Aβ plaques, suggesting wakefulness-linked Aβ elevation[103]. Leptin and cerebellin interact with Aβ, inhibiting aggregation, but their levels alter in AD, with leptin resistance amplifying pathology[128].

5.3. Interactions Between Neuropeptides and Aβ Aggregation Kinetics

Neuropeptides modulate the aggregation kinetics of Aβ, which will be fully discussed in the next chapter. Followings are some well documented examples.

BigDyn-$A\beta_{40}$ cross-interactions seem to be less hydrophobic with BigDyn suppressing and delaying the Aβ aggregation[98]. $A\beta_{40}$ is stabilized in α-helical secondary structure and its transition to βStrand is prevented by BigDyn via interacting with hydrophobic residues in the $A\beta_{40}$ disordered N-terminal[129]. SST binds $A\beta_{42}$ via tryptophan-dependent interfaces, favoring soluble oligomers over fibrils. NPY inhibits Aβ fibrillization, with fragments preventing neurotoxicity[130].

6. Aβ-Induced Membrane Disruption

Membrane disruption refers to the loss of lipid bilayer integrity, resulting in increased permeability, altered lipid organization, or membrane fragmentation. Aβ perturbs membranes by several modalities such as, pore/channel formation by oligomers, detergent-like disruption by larger aggregates, and indirect disruption via membrane-associated signaling pathways[131,132].

Aβ-induced membrane disruption is a multifactorial process in which Aβ peptides interact with lipid bilayers to perturb membrane structure, alter ion homeostasis, and trigger downstream neurotoxic cascades[133]. Key mechanisms identified in the literature include;

Pore/channel formation: Aβ oligomers insert into the bilayer to form discrete, ion-permeable pores (often β-barrel-like structures) that allow uncontrolled passage of Ca^{2+}, Na^{+}, and other ions. $A\beta_{42}$ preferentially assembles into stable β-barrel pore-forming oligomers ($\beta PFOsA\beta_{42}$) in membrane-mimicking environments, whereas Aβ40 tends to form fibrils. These pores exhibit defined conductance[132,134,135].

Carpet-like surface coverage and detergent-like effects: Prefibrillar Aβ species adsorb onto the membrane surface, exerting asymmetric pressure that thins the bilayer, extracts lipids, or induces non-specific leakage[132].

Two-step process: Initial formation of ion-selective pores is followed by surface-catalyzed fibril growth that drives non-specific fragmentation and vesicle disruption. Aβ as a "channel-forming" peptide introduced the concept that oligomeric Aβ can insert into lipid bilayers to create discrete, ion-conducting pores, leading to unregulated cation influx[136].

The forementioned disruption mechanisms happen in the following order: 1- early, oligomeric Aβ species form channel-like or pore-forming structures that allow unregulated permeabilization of the membrane, and 2- later stages involve fibril growth and detergent-like fragmentation that destabilize membrane integrity and disrupt lipid organization[131,133,137].

Membrane disruption is highly dependent on peptide-to-lipid ratio, peptide length, and lipid composition. High peptide-to-lipid ratios favor fibrillation-driven leakage, while low ratios can stabilize transient channels or induce fusion[138].

6.1. Effects of Specific Lipid Bilayers on Aβ Pore Formation

Lipid composition modulates Aβ binding, oligomerization, insertion, pore stability, and overall disruption. Neuronal membranes are heterogeneous, with distinct domains (liquid-ordered lipid rafts vs. liquid-disordered regions) that partition Aβ differently.

Anionic phospholipids (e.g., phosphatidylglycerol (PG), phosphatidylserine (PS), cardiolipin): These negatively charged headgroups promote electrostatic attraction to the positively charged N-terminal region of Aβ, accelerating surface binding, α-to-β conformational transition, oligomerization, and pore/channel formation. In PC:PG (4:1) liposomes, anionic lipids enhance

leakage during fibrillation, stabilize transient cation-selective channels, and facilitate lipid uptake into Aβ-lipid aggregates. In brain total lipid extracts (rich in PS and other anionic species), $A\beta_{42}$ forms abundant pore-like structures (10–20 nm diameter) with heterogeneous burst-like conductance. Pure zwitterionic PC bilayers show weaker binding and less disruption[132,135,139].

Gangliosides (particularly GM1): GM1 clusters in lipid rafts act as high-affinity receptors that seed Aβ oligomerization and stabilize pore-forming conformations. Ganglioside–Aβ interactions (via the sugar headgroup and Aβ's central hydrophobic region–KLVFFA) lower the energy barrier for β-sheet-rich oligomer assembly and transmembrane insertion. In GM1-containing bilayers, Aβ pore formation is markedly enhanced compared to ganglioside-free membranes; depletion or absence of GM1 strongly suppresses amyloid pore assembly [140]. GM1 cooperates with cholesterol to drive a common pore-forming mechanism shared with other amyloid proteins (α-synuclein)[132,140,141].

Cholesterol exerts a dual, context-dependent effect often described as a "double-edged sword." In raft-mimicking environments, cholesterol promotes Aβ incorporation, stabilizes α-helical transmembrane topologies, and facilitates formation of calcium-permeable amyloid pores. It accelerates surface-catalyzed nucleation and favors pore activation[142]. However, at higher concentrations that rigidify the bilayer (reducing fluidity), cholesterol can inhibit deep insertion, stabilize the membrane against perforation, and reduce toxicity despite increased surface association of oligomers[142,143]. Depletion of cholesterol increases membrane fluidity and perforation but decreases ordered raft domains that seed pores[144]. In pure POPC or low-cholesterol bilayers, pore formation is reduced; in cholesterol-rich neuronal or astrocytic membranes, pore-mediated Ca^{2+} influx is amplified[132,142].

Raft-like bilayers strongly promote Aβ oligomerization, β-barrel pore assembly, and toxicity compared to non-raft (Ld) or purely zwitterionic membranes. Raft clustering concentrates Aβ, GM1, and cholesterol, creating a microenvironment that favors the conformational changes required for pore insertion[145]. Brain total lipid extracts (containing raft components plus anionic lipids) support robust pore formation with heterogeneous conductance, closely mimicking in vivo conditions[135].

6.2. Biophysical Background of Aβ–Membrane Interactions

Membrane interaction is strongly influenced by peptide aggregation's state, lipids composition, and environmental factors such as pH and ionic strength[146]. Biophysical work with model membranes has demonstrated that Aβ binding can 1- redistribute lipids, 2- affect bilayer thickness and curvature, and 3- perturb lateral organization, particularly in cholesterol- and ganglioside-rich microdomains[147]. The hypothesis that Aβ forms ion channels posits that annular oligomers assemble into transmembrane structures with a hydrophilic pore and hydrophobic exterior, analogous to classical pore-forming toxins. By contrast, detergent-like disruption associated with fibril growth would be expected to produce a more generalized increase in conductance and loss of selectivity, consistent with large pores or membrane ruptures[147].

In summary, anionic lipids and gangliosides drive initial binding and oligomerization, while cholesterol and raft domains modulate the transition to inserted, pore-competent β-barrel structures. These lipid-dependent effects explain why Aβ toxicity is amplified in raft-rich neuronal membranes and why alterations in brain lipid composition (e.g., cholesterol dysregulation, ganglioside loss) correlate with AD progression.

7. Biophysical Methodology to Study Heterotypic Cross-Interaction

7.1. Circular dichroism spectroscopy

Circular dichroism (CD) spectroscopy is a powerful biophysical technique widely used in the structural characterization of peptides and proteins. It exploits the differential absorption of left- and right-circularly polarized light by chiral molecules, providing insights into their secondary and tertiary structures. Peptides can adopt various conformations such as α-helices, β-sheets, β-turns, or random coils, and CD helps elucidate these without the need for crystallization or high-resolution imaging techniques like nuclear magnetic resonance (NMR) or X-ray crystallography.

The technique has evolved significantly, with applications spanning protein engineering, pharmaceutical development, and membrane biology. For instance, CD is used to assess conformational stability, detect folding changes upon environmental perturbations, and evaluate interactions with ligands or membranes. Recent advances, including vibrational circular dichroism (VCD) and computational simulations, have enhanced its precision for complex structures like β-turns.

CD spectra are typically recorded in the far-UV region (180-260 nm), where peptide bonds absorb, reflecting secondary structure. Aβ peptides start in a random coil or unstructured state in solution but adopt β-sheet structures during aggregation. This shift is detectable in the far-UV CD spectrum, α-helices show characteristic negative bands at ~208 nm and ~222 nm, with a positive band at ~190-195 nm, β-sheets exhibit a negative band at ~219 nm and a positive at ~195 nm, while random coils have a strong negative band near 200 nm[148–150].

The mean residue ellipticity [θ] ($deg \cdot cm^2 \cdot dmol^{-1}$) is calculated by the following equation,

$[\theta] = \frac{\theta_{obs}}{(10 \times c \times l \times n)}$ (Eq. 1), where θ_{obs} is observed ellipticity in millidegrees, c is peptide concentration (mol/dm³), l is path length (cm), and n is the number of residues.

7.2. Electron microscopy

EM, including transmission electron microscopy (TEM) and cryo-EM, enables direct visualization of Aβ aggregates at high resolution. TEM involves staining samples with heavy metals like uranyl acetate to enhance contrast, revealing fibrillar structures with diameters of 7-10 nm and lengths up to micrometers. Cryo-EM preserves samples in vitreous ice, avoiding artifacts from drying or staining, and has revolutionized structural biology by resolving atomic details of Aβ fibrils[151].

EMs use beams of electrons to achieve resolutions down to the atomic level. This is possible because electrons have much shorter wavelengths than photons in visible light, allowing for imaging at nanometer scales. Developed in the early 20th century, with Ernst Ruska's invention of the first electron microscope in 1931, EM has revolutionized fields such as materials science, biology, and biophysics[152].

Scanning Electron Microscopy (SEM) scans the surface of a sample with an electron beam to produce three-dimensional images, making it ideal for topological studies. In contrast, TEM transmits electrons through an ultra-thin sample to generate two-dimensional projections, revealing internal structures[153].

7.3. Studying Amyloid-β Fibrils

In the biophysical study of Aβ fibrils, TEM methodology is adapted to capture their polymorphic nature, fibrils can vary in length, width (typically 5-10 nm), and twist periodicity. First step is in vitro fibrillization, Aβ peptides are incubated under conditions promoting aggregation. Samples are then prepared via negative staining or cryo-EM to minimize artifacts.

Negative staining TEM reveals fibril morphology, straight or twisted filaments, often with crossover points indicating helical symmetry. For instance, early studies using TEM identified Aβ fibrils as unbranched, 6-10 nm wide structures with a characteristic beta-sheet core, confirmed by X-ray fiber diffraction. Quantitative biophysical analysis involves measuring fibril dimensions from TEM images, length distributions follow exponential decays, suggesting nucleation-dependent polymerization kinetics, a key biophysical model for amyloid growth[154].

Cryo-EM elevates this by preserving native states, allowing visualization of transient intermediates like protofibrils or oligomers, which are toxic species in Alzheimer's pathogenesis. In cryo-EM, samples are plunge-frozen, and images are collected at low electron doses to prevent beam-induced damage. This has enabled 3D reconstructions via cryo-electron tomography, revealing Aβ fibril polymorphs with distinct cross-sections[155].

7.4. Aggregation Kinetics: ThT Assay

Aggregation kinetics of Aβ peptides are crucial for elucidating the mechanisms underlying fibril formation and identifying therapeutic interventions. This kinetic progression is characterized by a nucleation-dependent polymerization model, where initial slow steps give way to rapid amplification. ThT assays are the gold standard for monitoring these kinetics due to their simplicity and sensitivity. ThT is a cationic benzothiazole dye that exhibits enhanced fluorescence intensity upon binding to amyloid fibrils. Its emission at 482 nm (excitation 450 nm) increases dramatically when intercalated into the cross-β structure, making it ideal for real-time monitoring without perturbing the system significantly[156].

In Aβ studies, ThT assays (as shown in fig.4) reveal a sigmoidal curve; a lag phase (nucleation), growth phase (elongation), and plateau (equilibrium), and half-maximal aggregation points. For $A\beta_{42}$, the lag phase is shorter than $A\beta_{40}$ due to higher hydrophobicity.

The aggregation process unfolds in distinct phases, each with unique kinetic characteristics and implications for neurotoxicity. The initial nucleation or lag phase involves the slow formation of a critical nucleus from monomeric Aβ, where peptides transition from random coil or α-helical conformations to β-sheet-rich structures. This phase is rate-limiting, highly sensitive to concentration. At physiological levels (picomolar to nanomolar), nucleation is rare, but seeding accelerates it. During this stage, transient dimers and trimers form, but the nucleus, typically comprising 4-10 monomers serves as a template for further addition. Kinetic models, such as the Finke-Watzky (F-W) two-step mechanism, slow and contionus nucleation, $\mathrm{A} \xrightarrow{\kappa_1} \mathrm{B}$, and fast and autocatalytic, $\mathrm{A} + \mathrm{B} \xrightarrow{\kappa_2} 2\mathrm{B}$ (Eq. 2) where 'A' is monomer, 'B' is aggregate, k_1 is the rate constants for nucleation, and k_2 is the autocatalytic growth constant[157–159].

Following the nucleation phase, the elongation or the log phase ensues, marked by rapid fibril extension through monomer addition to the nucleus ends, often exhibiting sigmoidal kinetics with exponential growth rates. In this phase, secondary processes like fibril fragmentation generate new ends, amplifying self-aggregation via a positive feedback loop, as seen in prion-like models. Fragmentation reduces lag time and increases the plateau level of aggregates, with breakage rates influenced by mechanical agitation or cellular shear forces[160]. Finally, the stationary or plateau phase represents equilibrium, where monomer depletion halts net growth, maintaining a dynamic balance between soluble monomers, oligomers, and insoluble fibrils. In this phase, off-pathway aggregates like annular protofibrils or amorphous deposits may form,

and depolymerization can occur if conditions shift, though in AD brains, plaques persist due to stabilization by metals or proteins[22].

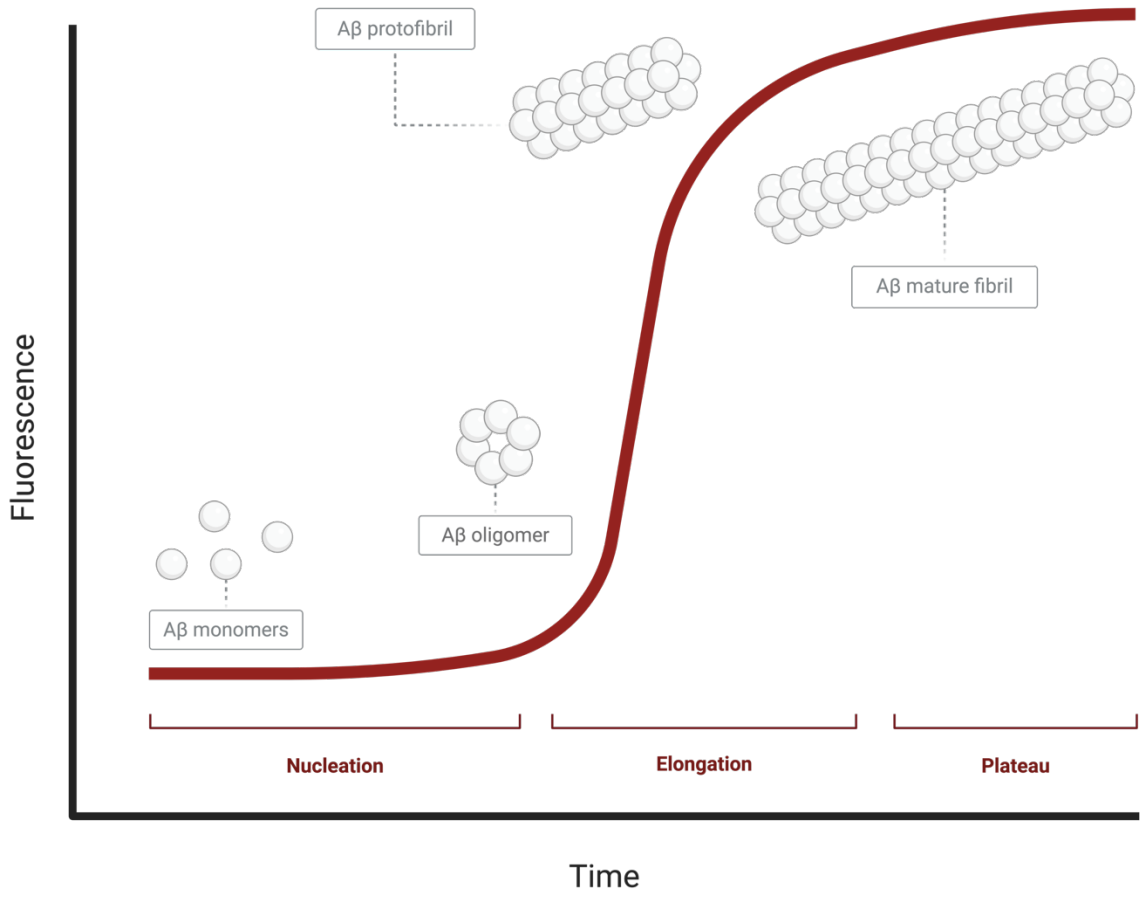


Figure 4. Schematic of Aβ aggregation kinetics by ThT assay. (Created using Biorender.com).

For the ThT fluorescence kinetic traces analysis, sigmoidal curve fitting based on Eq.3 determines the parameters' aggregation halftime, $\tau_{1/2}$ and the maximum growth rate (rmax).

$$F(t) = F0 + \frac{A}{1+\exp[r_{max}\left(\frac{\tau_1}{2}\right)-t]} \qquad \text{Eq. 3}$$

Where F0 is the fluorescence signal intensity baseline, A is the fluorescence intensity amplitude, r_{max} is the maximum growth rate and the aggregation halftime ($\tau_{1/2}$) corresponds to when the monomeric $A\beta_{42}$ peptide population is half depleted[160].

7.5. Cell Viability: MTT Assay

Assessing cell viability in the presence of Aβ is critical to understanding its neurotoxicity. The MTT assay, based on mitochondrial dehydrogenase activity, is widely used for this purpose. MTT (3-(4,5-dimethylthiazol-2-yl)-2,5-diphenyltetrazolium bromide) is reduced to purple formazan by NAD(P)H-dependent enzymes in viable cells. Absorbance at 570 nm quantifies viability. In Aβ studies, MTT reveals dose- and time-dependent toxicity. Aβ oligomers are more toxic than fibrils, reducing MTT by 20-50% at 1-10 µM. SH-SY5Y cells are treated with Aβ for 24-48h, MTT added (0.5 mg/ml, 4h), solubilized in DMSO, read at 570 nm[161,162].

7.6. Liposome Leakage Assay

Liposome leakage assays model Aβ-membrane interactions, where Aβ disrupts bilayers, causing leakage linked to toxicity. Spectrophotometry detects leaked dyes, while characterization uses DLS for size and stability[163].

Liposomes mimic neuronal membranes using phospholipids such as 1-palmitoyl-2-oleoyl-sn-glycero-3-phosphocholine (POPC), 1-Palmitoyl-2-Oleyol-sn-Glycerol-3-[Phosho-rac-(1-glycerol)] (POPG), or colesterol. Aβ induces pores or disrupts integrity, leaking encapsulated fluorophores like calcein or carboxyfluorescein, quenched at high concentrations but fluorescent upon dilution. Spectrophotometry measures fluorescence increase post-Aβ treatment, and the leakage is oligomer-dependent[164].

Liposomes, spherical vesicles composed of phospholipid bilayers, serve as biomimetic cell membranes, to study membrane interactions, permeability, and stability under various conditions. One critical aspect of liposome research is assessing their integrity, particularly how external factors like proteins, peptides, or chemicals can disrupt the bilayer, leading to the release of encapsulated contents. This phenomenon is quantified through liposome leakage assays, which provide insights into membrane permeabilization mechanisms[165].

7.6.1. Understanding the Concept of Liposome Leakage Assays

At its core, a liposome leakage assay measures the release of aqueous contents from the liposome's interior due to membrane disruption. Liposomes can encapsulate hydrophilic molecules, such as fluorescent dyes, which serve as reporters for leakage events. When the membrane remains intact, these dyes are confined within the vesicle, often in a quenched state due to high local concentrations or the presence of a quencher. Upon permeabilization, caused by factors like cell penetrating peptides (CPPs), detergents, or environmental stressors, the contents leak out, leading to detectable changes in fluorescence properties[165,166].

The principle often relies on fluorescence dequenching or quenching dynamics. Complexes like 8-hydroxypyrene-1,3,6-trisulfonic acid (HPTS) and p-xylene-bis-pyridinium bromide (DPX) are used, so HPTS fluorescence is quenched by DPX when co-encapsulated, but leakage separates them, resulting in dequenching and increased emission. This approach distinguishes leakage from other processes like fusion, where contents might mix without external release. The assay's sensitivity allows detection of subtle permeability changes, making it suitable for real-time monitoring over timescales from seconds to hours[167,168].

Liposome composition plays a pivotal role in the assay's outcomes. Incorporating cholesterol, for example, modulates membrane fluidity and thickness, often inhibiting leakage by stabilizing the

bilayer. Variations in lipid types, size, and charge further tailor the model to specific biological scenarios, such as mimicking bacterial or mammalian membranes[169].

7.6.2. The Methodology of Liposome Preparation

The methodology of liposome leakage assays is straightforward yet requires precision to avoid artifacts, such as spontaneous leakage or incomplete encapsulation. Below is a step-by-step overview based on the applicated protocols by fluorescence dequenching approach with HPTS/DPX.

1. **Liposome Preparation**: Liposomes are typically formed using the thin-film hydration method. Lipids are dissolved in an organic solvent (e.g. chloroform), evaporated to form a thin film, and then hydrated with a buffer containing the fluorescent probe and the quencher. The mixture is subjected to vortexing, sonication, or extrusion through bipolycarbonate filters to downsize to uniform large unilamellar vesicles (LUVs) of 100-200 nm diameter. Freeze-thaw cycles enhance encapsulation efficiency.
2. **Purification**: Unencapsulated dyes are removed via size-exclusion chromatography (e.g., using Sephadex G-50 columns). This step is crucial for baseline stability.
3. **Assay Setup**: The purified liposomes are diluted in an isotonic buffer to a final lipid concentration of about 50-100 μM. Fluorescence is measured using a spectrofluorometer with excitation at 413 nm and emission at 510 nm for HPTS/DPX. Initial readings establish the baseline (quenched state).
4. **Induction of Leakage**: The peptide is added at varying concentrations. The mixture is incubated at controlled temperatures (37 ºC), and fluorescence is monitored kinetically. Leakage is quantified as the percentage increase in fluorescence relative to maximum

dequenching, achieved by adding a detergent like Triton X-100 (TX100) to fully disrupt the liposomes[170–172].

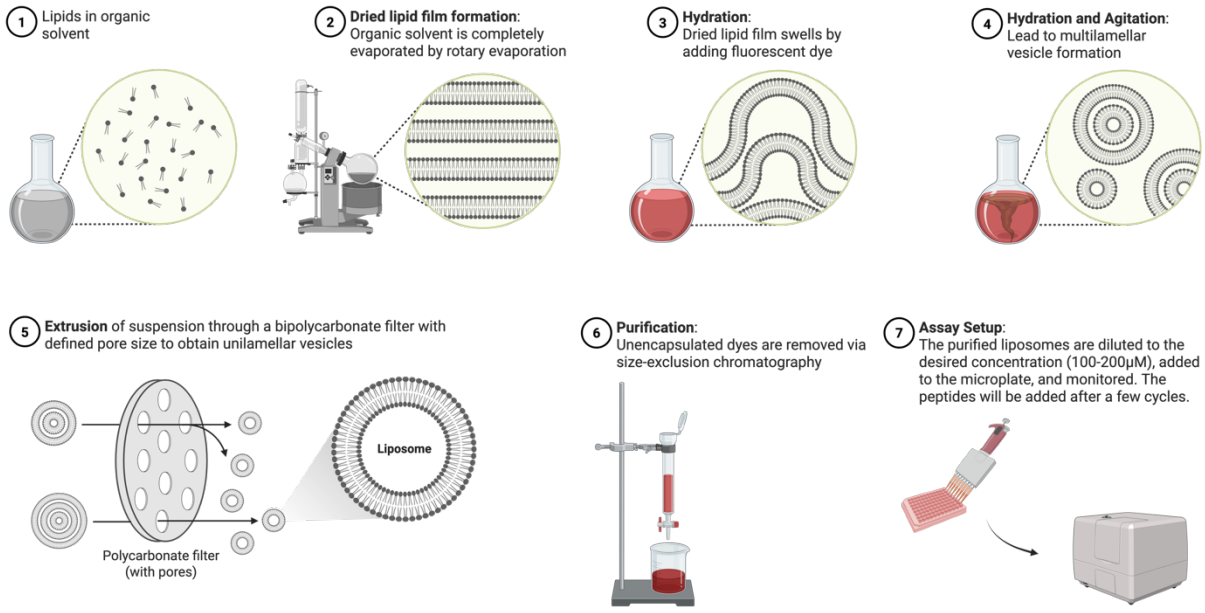


Figure 5. The schematic illustration of liposomes preparation protocol using thin-film hydration followed by extrusion method. (Designed using Biorender.com).

7.6.3. Dynamic Light Scattering

The fundamental principle of DLS revolves around Brownian motion, the random movement of particles suspended in a fluid due to collisions with solvent molecules. Smaller particles exhibit faster Brownian motion, while larger ones move slower. When a coherent light source, typically a laser, illuminates the sample, the particles scatter the light (Rayleigh scattering) in all directions. Due to the particles' motion, the scattered light experiences Doppler shifts, leading to fluctuations in intensity over time. DLS is sensitive to particle size distributions, providing metrics like the Z-average (intensity-weighted mean diameter) and polydispersity index (PDI), which indicates the breadth of the distribution[173].

GENERAL OBJECTIVES

The general objectives of this doctoral thesis are:

I. To elucidate the heterotypic interaction between Neurokinin (NKA) and amyloid-β42 ($A\beta_{42}$), defining the role of phenylalanine-driven aromatic contacts within the FXGLM motif as a molecular gate of the central hydrophobic core (CHC) of $A\beta_{42}$, and assessing the consequent effects on $A\beta_{42}$ conformational landscape, aggregation dynamics, and neuronal toxicity.

II. To characterize the conformation-selective heterotypic interaction between angiotensin II (AngII) and amyloid-β peptides ($A\beta_{40}$ and $A\beta_{42}$), determining its preferential engagement of disordered and early Aβ conformers, and evaluating its modulatory impact on Aβ aggregation kinetics, aggregate thermal stability, and Aβ-induced membrane disruption in the context of renin-angiotensin system dysregulation in Alzheimer's disease.

III. To investigate the heterotypic interaction between Dynorphin A (DynA) and its SCA23-linked clinical variants (L5S, R6W, R9C) with $A\beta_{42}$, characterizing variant-specific effects on $A\beta_{42}$ ordered assembly and hydrophobic co-aggregation, and determining the charge- and aromaticity-dependent molecular determinants that govern their differential membrane-disruptive activity across lipid compositions relevant to neuronal bilayers.

IV. To establish a mechanistic framework in which heterotypic neuropeptide-Aβ interactions constitute a conformation-selective proteostatic checkpoint of the amyloid cascade, and

to identify the molecular principles governing this buffering network as a foundation for the rational design of peptide-based therapeutic and diagnostic strategies in Alzheimer's disease.

CHAPTER I

*This chapter is based on the following published article: Habibnia, M., Catalina-Hernandez, E., Lopez-Martin, M., Masnou-Sanchez, D. & Peralvarez-Marin, A. Decoding the molecular and structural determinants of the neurokinin A and Aβ1-42 peptide cross-interaction in the amyloid cascade pathway. iScience 27, 111187 (2024). https://doi.org/10.1016/j.isci.2024.111187[97]. The content contains minor revisions for consistency with the overall thesis narrative.

Decoding the Molecular and Structural Determinants of the Neurokinin A and $A\beta_{42}$ Peptide Cross-Interaction in the Amyloid Cascade Pathway[97]

SUMMARY

Tachykinins are short neuropeptides, such as substance P and neurokinin B, that have been shown to interact with Alzheimer's β-amyloid (Aβ) peptide. Neurokinin A (NKA) is a secreted tachykinin neuropeptide that binds to neurokinin receptors and with an emerging role in the brain-gut axis. NKA shares the brain niche with Aβ, thus we investigate whether and how NKA and Aβ peptide interact. We have used a combination of computational and experimental biophysics to assess the interaction of both peptides in vitro. Using Phe-to-Trp substitution we have shown that Phe in the FXGLM signature in NKA is important for such interaction and for the modulation of the Aβ peptide amyloid cascade. Besides, cellular experiments have shown that the NKA-Aβ interaction decreases the Aβ peptide toxicity. Altogether, our work raises the intriguing possibility that NKA balance and the NKA-Aβ peptide interplay are relevant in the aggregation process in Alzheimer's disease.

Keywords

Tachykinins; β-amyloid peptide; protein aggregation; brain-gut axis; Alzheimer's disease; peptide-peptide cross-interactions.

INTRODUCTION

Alzheimer's disease (AD) as a neurodegenerative disorder is the major cause of elderly dementia and the most prevalent form of amyloidosis with aging as its most significant risk factor[174]. Monomeric soluble amyloid-beta (Aβ) peptides aggregate into β-sheet rich oligomers and insoluble fibrils into extracellular senile Aβ plaques[175–177] resulting in oxidative stress, neuronal loss, blood-brain barrier breakdown, synaptic dysfunction, metal homeostasis disturbance leading to neuronal death[12,15,118,178].

Neuropeptides as molecules coexisting with Aβ peptides are key potential interactors for Aβ and, more importantly, putative enhancers, chelators and/or buffers of the amyloid potential of this peptide, as it has been shown in several peptide homo and hetero-cross-interactions[62,70,179,180], such as dynorphins[98] or tachykinins (TKs)[181], both of them related to the brain-gut axis[182,183]. The progression of Aβ fibril development occurs during the aggregation process, with monomers of Aβ serving as seeds for nucleation in the initial phase. Overcoming the challenge of preventing or inhibiting the formation of toxic early-stage dimers is complex, given the myriads of physiological factors that can either promote or inhibit this process, depending on the physiological state. In fact, the study of peptide cross-interactions allows a better understanding of the pathophysiology of neurodegenerative disorders[180,184], but also opens a rational-design window to define peptide-based therapy and diagnosis strategies[64].

Mammalian TKs are a family of neuropeptides broadly expressed in neuronal and nonneuronal tissues[185]. TKs target receptors are vastly localized in the brain and these neuropeptides function as neurotransmitters in different biological activities including pain processing, neuroinflammation, hormone regulation, immune function, and memory formation[186,187], and more recently on the spot of the brain-gut axis[63]. The three foremost TK members in mammalian species are substance P (SP), Neurokinin A (NKA), and Neurokinin B (NKB) which consist of 10-12 residues sharing the conserved motif FXGLM in the C-terminal region (X, hydrophobic residue)[188]. The cerebrospinal fluid tachykinergic system's functionality is altered in patients suffering from AD, as it's been indicated that TKs levels, as well as their immunoreactivity, are decreased in the brains of AD patients[189,190]. It has been shown that SP and NKB are able to interact with Aβ and modulate the amyloid cascade[45,96,181]. Aβ and TKs peptides coexist in the brain parenchyma and cross-interact affecting AD progression. Several studies have indicated the neuroprotective effects of TKs in AD both in vivo and in vitro[113,191–194]. NKA is ubiquitously expressed in the central and peripheral nervous system, released from the nerve endings and acting as a neurotransmitter and neuromodulator in various neurophysiological activities[195], with high affinity to type 2 neurokinin receptor (NK-2R)[196]. NKA has been recently related to the brain-gut axis connection in neurodegenerative disorders[197,198].

Comprehensive assessment of the molecular and structural determinants of cross-interactions is imperative, considering their potential positive, negative or neutral impact on the amyloid pathway. In the present study we complement computational simulations to characterize the NKA-$A\beta_{42}$ cross-interaction with in vitro biophysical characterization and cell toxicity experiments

to determine the influence of NKA over the Aβ amyloid pathway, which may open rational-design window to define peptide-based therapy and diagnosis strategies for NKA.

Table 2. Peptide physico-chemical properties.

Peptide	Primary sequence	Mol. Weight[a]	pI[a]	Charge[a]	GRAVY Index[a]
$A\beta_{42}$	DAEFRHDSGYEVHHQKLVFFAEDVGSNKGAIIGLMVGGVVIA	4514.1	5.3	-3	0.20
NKA	HKTDSFVGLM-NH_2	1134.3	6.7	0	0.02
NKAW	HKTDSWVGLM-NH_2	1173.3	6.7	0	-0.35
NKB	DMHDFFVGLM-NH_2	1211.4	4.2	-2	0.68
Substance P	RPKPQQFFGLM-NH_2	1348.63	11.0	+2	-0.70

[a] Analysis performed using Expasy ProtParam tool[199].

Material and Methods

Peptide-peptide docking

Global docking was performed using the Rosetta docking protocol[200]. Input structures for $A\beta_{42}$ – Protein Data Bank (PDB) codes for random coil (6SZF, peptide in solution) and helical (1IYT, peptide in bicelles) structures, and NKA (PDB code 1N6T) - were retrieved from the Protein Data Bank, whereas NKAW structure was obtained by computationally replacing F6 with W6 with UCSF Chimera swapaa command[201] using Dunbrack's rotamer library. Both NKA and NKAW peptides were acetylated at the C-terminus. Rosetta's local refinement was used after completion of global docking to correct possible clashes present at the interaction interface. Finally, Rosetta's energy-based clustering algorithm[202] was used, taking the centroid of the most energetically favorable clusters as input structures for molecular dynamics simulations (MDs).

Molecular dynamics simulations and analysis

NKA/NKAW: $A\beta_{42}$ systems and $A\beta_{42}$ only systems were prepared for MD simulations using the CHARMM36m force field[203] and TIP3P water model. Simulations consisted on 5 000 steepest

descent minimization steps, followed by 200 ps of NVT (Number of particles, Volume, and Temperature of the system are kept constant) equilibration, and 1 ns of NPT (Number of particles, Pressure, and Temperature of the system are kept constant) equilibration with positional restraints, after which the imposed restrictions were released to further equilibrate the system in the NPT ensemble for 2 ns. Production runs were performed for 1 μs, using Berendsen barostat and thermostat for pressure and temperature coupling at 1 bar and 310 K respectively. Particle Mesh Ewald was used for electrostatics. Two different stoichiometries, using helical (1IYT) or random coil (6SZF) as starting $A\beta_{42}$ structures were simulated for the NKA/NKAW: $A\beta_{42}$ systems, being 2:2 (2 $A\beta_{42}$ molecules: 2 NKA/NKAW molecules), and 2:1 (2 $A\beta_{42}$ molecules, 1 NKA/NKAW molecule), accounting for a total of 12 individual simulations, summing up to 12 μs of total simulation time. Convergence of the simulations was checked with MDTraj[204]. Secondary structure conversion analyses during the trajectories were performed using Timeline plugin in VMD[205], according to the secondary structures defined in STRIDE software[206].

Peptides

Synthetic human $A\beta_{42}$ (DAEFRHDSGYEVHHQKLVFFAEDVGSNKGAIIGLMVGG-VVIA) with a purity of >95% was purchased from AlexoTech (Umeå, Sweden), NKA (HKTDSFVGLM-NH_2) and NKAW (HKTDS**W**VGLM-NH_2) were purchased from pepMic Co., Ltd (Jiangsu, China).

Sample preparation

$A\beta_{42}$ samples with high-monomer content were prepared by dissolving $A\beta_{42}$ in 20 mM NaOH, at a concentration of 1 $mg{\cdot}ml^{-1}$ and sonicated at least three times in an ice bath[207]. Peptide samples

were snap-frozen in liquid nitrogen and kept at -80ºC until further use. The $A\beta_{42}$ were diluted to the working concentration in 10 mM phosphate buffer at pH 7.2. Incubated samples for CD (Figure S3), were allowed aggregate for 2 h at 37 ºC. NKA and NKAW peptides were dissolved directly in 10 mM sodium phosphate buffer pH 7.2. The peptide concentration was determined by weight or spectrophotometrically by absorbance at 280 nm.

Circular dichroism measurements

The far-UV CD spectra (190-250 nm) of the peptide samples were recorded on a Jasco J-815 CD spectrometer (Halifax, Canada) spectropolarimeter. The calibration of the instrument was done prior to each measurement. All measurements were performed at 25°C through a 1 mm path length quartz cuvette. Five scans were recorded and averaged for each spectrum. Peptide concentration used in all experiments was 100 µM in sodium phosphate buffer (10 mM, pH 7.2). For incubated samples containing $A\beta_{42}$ peptide, concentrations were reduced to match the concentrations used in ThT experiments, and for that 10 scans were recorded and averaged for each sample.

Thioflavin T aggregation kinetics

$A\beta_{42}$ samples were prepared in ice at final concentration of 12 µM in 10 mM sodium phosphate buffer, pH 7.4., 10 mM sodium phosphate buffer pH 7.4, and 40 µM Thioflavin T (ThT, Sigma Aldrich, Cat. N. T3516). The aggregation kinetics were monitored in a 96-well microplate (non-treated) where each well was loaded with 100 µL solutions of mastermix, 12 µM $A\beta_{42}$ and 6 µM NKA or NKAW, (2:1, $A\beta_{42}$:NKA/NKAW), and 12 µM $A\beta_{42}$ and 12 µM NKA or NKAW (2:2,

$A\beta_{42}$:NKA/NKAW). Peptide samples were loaded to the microplate from lower to higher concentrations. The microplate was covered with a plastic film before being inserted into the microplate reader. The fluorescence intensity was measured in triplicates using a 440 nm excitation filter and a 480 nm emission filter at 37 ºC with 86 rpm double orbital shake (before each cycle) in a FLUOstar Optima microplate reader (BMG LABTECH, Germany). The plots correspond to three independent experiments.

For the ThT fluorescence kinetic traces analysis, sigmoidal curve fitting based on Eq.4 determining the parameters aggregation halftime, $\tau_{1/2}$ and the maximum growth rate (rmax) were performed.

$$F(t) = F0 + \frac{A}{1+\exp[r_{max}\left(\frac{\tau_1}{2}\right)-t]} \qquad \text{Eq. 4}$$

Where F0 is the fluorescence signal intensity baseline, A is the fluorescence intensity amplitude, r_{max} is the maximum growth rate and the aggregation halftime ($\tau_{1/2}$) corresponds to when the monomeric $A\beta_{42}$ peptide population is half depleted.

Transmission electron microscopy negative staining

For negative staining, the sample was prepared by air-dried method. Briefly, an aliquot of purified VLPs was absorbed by flotation onto freshly glow discharged 400 mesh carbon fil copper grids (22-1MC040-100, MicrotoNano). After standing for 1 min at RT, excess sample was drained carefully off the grid using whatman filter paper nº1. Samples were then stained with 8 µL of uranyl acetate (2%) by incubation for 1 min at room temperature. Excess uranyl acetate was drained off as previously described[208].

Grids were observed in a Hitachi TEM operating at an accelerating voltage of 75 kV. Electron micrographs were recorded with a GATAN ES500W CCD using the Digital Micrograph software package (Gatan, Pleasanton, CA).

MTT cell viability assay

Mycoplasma negative Human SH-SY5Y neuroblastoma cells were cultured in DMEM/F12 medium nourished with 1xNEAA and 15 % FBS. Cells were grown in a 5 % CO2 humidified atmosphere at 37 ºC to 80 % confluence for a maximum of 20 passages. Differentiated SH-SY5Y cells were exposed to previously prepared mixtures of 10 µM aggregated $A\beta_{42}$ with 5 µM and 10 µM NKA and NKAW separately, after 20 hours of pre-incubation at 37 ºC. Cells were seeded into 96-well plates at a density of $1 \cdot 10^4$ cells/100 µL/well and incubated at 37 ºC for 24 hours. The toxicity rate was evaluated after cells were challenged with the different treatment mixtures after 24 h of incubation. Afterward, 11 µL of 3-(4,5-dimethylthiazol-2-yl)-2,5-diphenyltetrazolium bromide (MTT) solution was added to each well and incubated for 2 h at 37 ºC. After the reaction stopped, DMSO and absorbance were measured at 570 nm and 655 nm. A 100 % viability was considered for control cells.

EXPERIMENTAL MODEL AND STUDY PARTICIPANT DETAILS

Commercial SH-SY5Y cell line (ATCC CRL-2266) has been used in this study and tested negative for Mycoplasma. For all related experiments SH-SY5Y cells (from liquid N_2 storage) were used as the starting material. The experiments to assess cell viability were performed in triplicates for each experimental condition described in three (N=3) independent experiments.

QUANTIFICATION AND STATISTICAL ANALYSIS

For MTT toxicity comparison one-way analysis of Variance (ANOVA) was performed and corrected by Bonferroni's multiple comparison tests for statistical analysis using R software. Conditions yielding significant differences are indicated (*, $p < 0.01$; **, $p < 0.001$; ***, $p < 0.0001$).

Results

Building the NKA-Aβ dimer. In this study, we investigate the cross-interaction between NKA and Aβ. To establish an unbiased system, we employ peptide-peptide docking (Figure 6A), aiming to acquire an unsupervised configuration for the NKA-Aβ heterodimer as the starting point for our simulation (Figure 6B at 0 ns). The main contacts are between Glu22, Leu34, Met35 and Val39 in $Aβ_{42}$, and His1 and Lys2 in NKA, respectively (Figure 6B). We use the available structural information for $Aβ_{42,}$ such as the random coil structure (PDB 6SZF, Figure 6B) and the helical structure (PDB 1IYT, Figure 7) to define the reference for secondary structure dependent amyloid aggregation in solution. First, we use two randomly positioned Aβ monomers to observe the amyloid interaction between both monomers within of 1 μs simulation (Figure 6B and Figure 7). In parallel we follow the behavior of two stoichiometries for NKA: Aβ (Figure 6B) using all atom molecular dynamics for 1 μs.

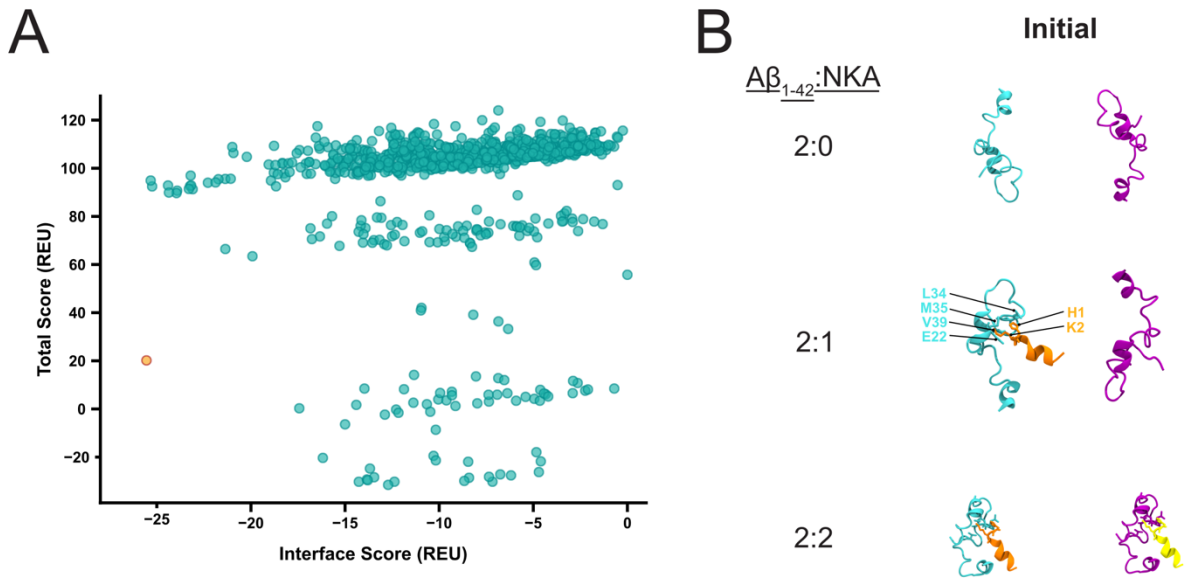


Figure 6. Peptide-peptide docking and time specific snapshots of the simulation. (A) Most stabilized docking pose is chosen (indicated in orange) by cross-correlation coefficiency. REU: Rosetta energy units. (**B)** Initial MD simulation snapshots of $A\beta_{42}$ dimer and $A\beta_{42}$-NKA peptide complex at indicated stoichiometries. $A\beta_{42}$ peptides are depicted in cyan and purple and NKA peptides are depicted in orange and yellow.

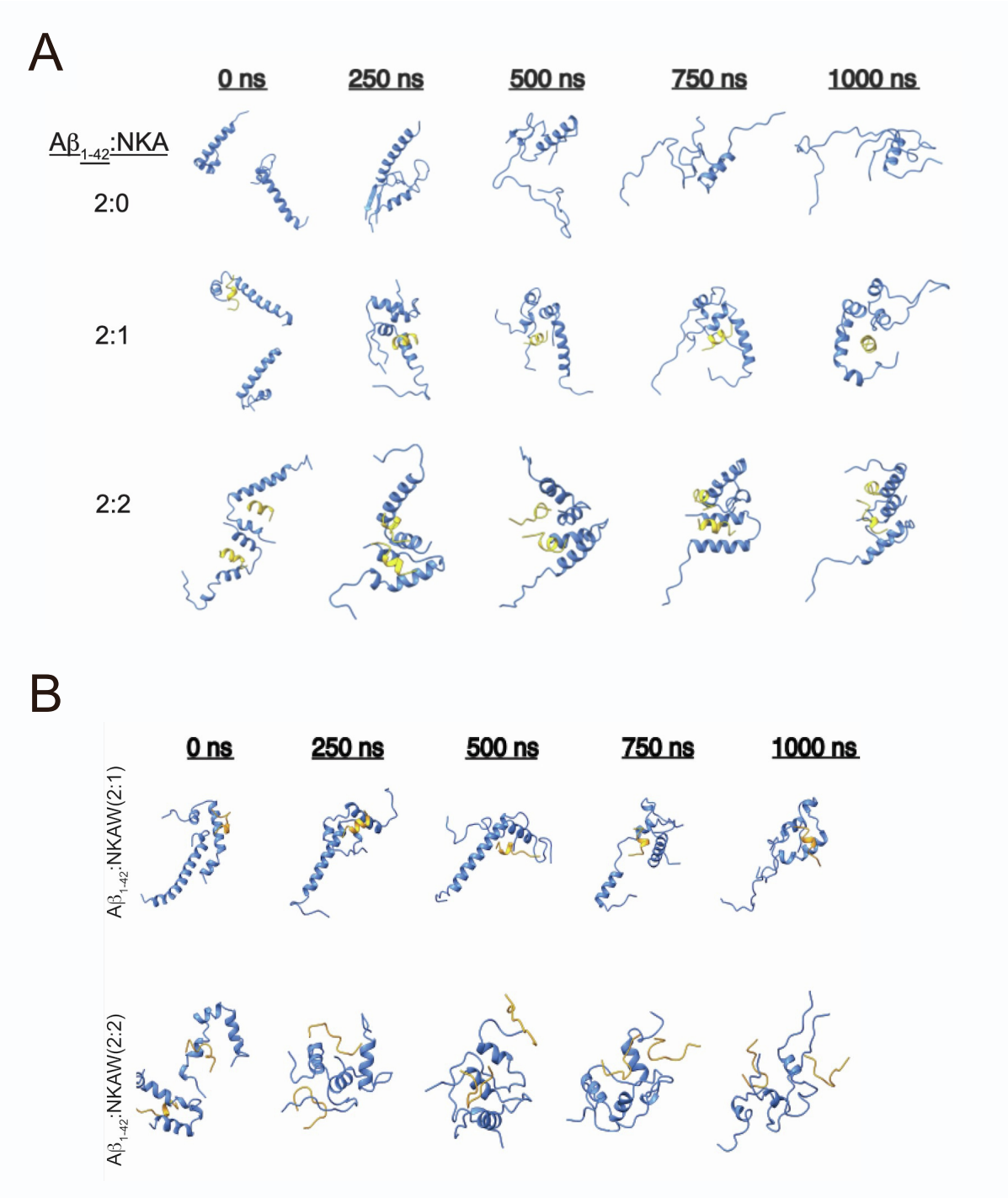


Figure 7. Time specific snapshots of the 1 μs simulations starting with helical $A\beta_{42}$. (A) Time specific MD simulation snapshots of $A\beta_{42}$ dimer and $A\beta_{42}$-NKA peptide complex in different time frames at indicated stoichiometries. (B) Time specific MD simulation snapshots of the $A\beta_{42}$-NKAW peptide complex in different time frames at indicated stoichiometries. $A\beta_{42}$ and NKA/NKAW are indicated in blue and gold, respectively.

NKA stabilizes helical structure in $A\beta_{42}$. In the absence of NKA, random coil $A\beta_{42}$ collapses into a dimer and defines a cluster of mostly random coil structure, a region of helical structure, and scattered β-structure hotspots throughout the peptide (Figure 8A). In presence of NKA, $A\beta_{42}$ helical secondary structure is favored in the central core (residues 23-30) of one $A\beta_{42}$ monomer at 2:1 (Figure 8B) and in both $A\beta_{42}$ monomers at 2:2 (Figure 8C) stoichiometries, respectively. Figure 9 shows the structural propensities in simulations carried out with helical $A\beta_{42}$ peptide as starting model. Within the 1 μs time frame, the $A\beta_{42}$ dimer loses helical structures in favor of random coil and turn structures, together with the onset of b-sheet related spots (bridge and extended) in the C-terminus. The presence of NKA at both stoichiometries, stabilizes the helical $A\beta_{42}$ structure at the central, secondary, and C-terminal hydrophobic cores in $A\beta_{42}$ (Figure 9).

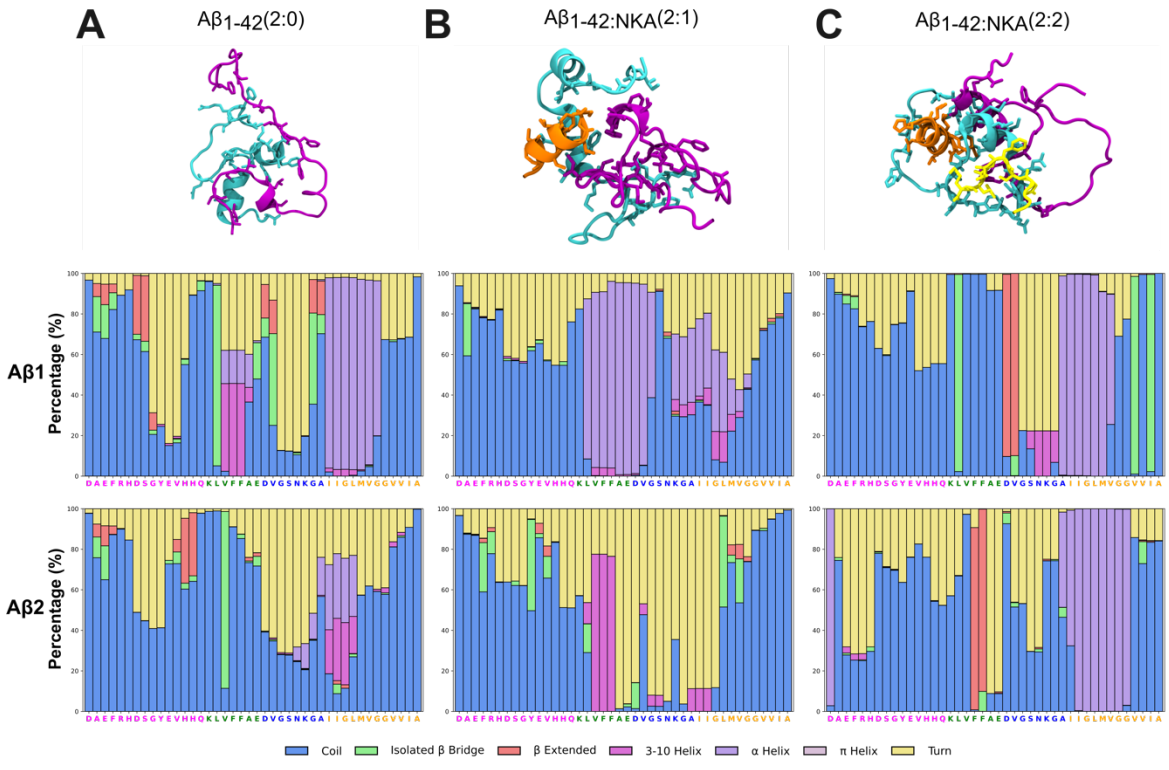


Figure 8. Secondary structure propensities of $A\beta_{42}$ induced by NKA cross-interaction. Aβ1 and Aβ2 together as $A\beta_{42}$ dimer and their secondary structure conversion with a total simulation contact time of the last 500 ns of the simulation for: (A) $A\beta_{42}$ dimer

(2:0), (B) $A\beta_{42}$-NKA (2:1), and (C) $A\beta_{42}$-NKA (2:2). On top, molecular illustration of the most representative cluster of the last 500 ns of the simulation. $A\beta_{42}$ peptides are depicted in cyan and purple and NKA peptides are depicted in orange and yellow. $A\beta_{42}$ domains are indicated following the color code: N-terminal unstructured domain (residues 1 to 15) in magenta; primary hydrophobic core (residues 16 to 22) in green; central core (residues 23 to 30) in blue; and C-terminal hydrophobic core (residues 342) in yellow.

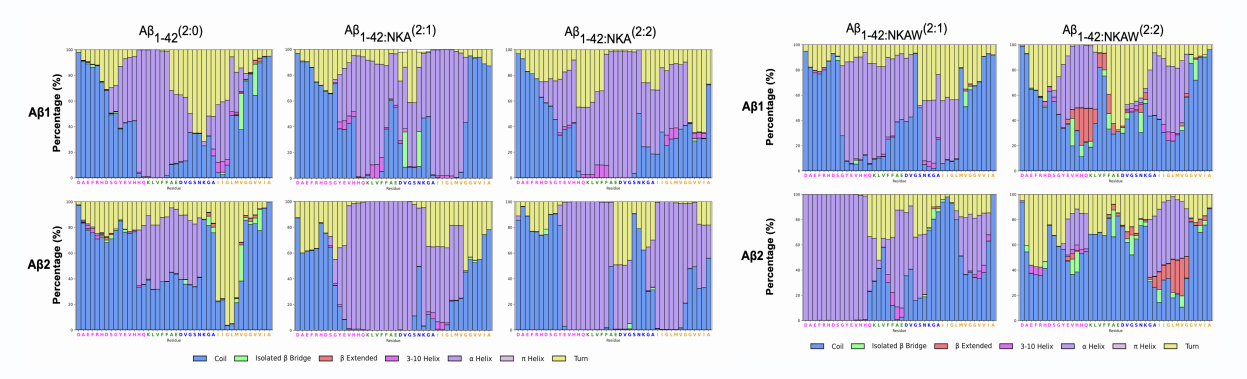


Figure 9. Secondary structure propensities of $A\beta_{42}$ in a 1 μs simulation starting with helical $A\beta_{42}$. Aβ1 and Aβ2 together as $A\beta_{42}$ dimer and their secondary structure conversion with a total simulation contact time of the last 500 ns of the simulation for: $A\beta_{42}$ dimer (2:0), $A\beta_{42}$-NKA (2:1), $A\beta_{42}$-NKA (2:2), $A\beta_{42}$-NKAW (2:1), and $A\beta_{42}$-NKAW (2:2). $A\beta_{42}$ domains are indicated following the color code: N-terminal unstructured domain (residues 1 to 15) in magenta; primary hydrophobic core (residues 16 to 22) in green; central core (residues 23 to 30) in blue; and C-terminal hydrophobic core (residues 342) in yellow.

Regardless of using a random coil (Figure 10A) or helical (Figure 11) for $A\beta_{42}$ structure, there are several hydrophobic driven contacts between monomer, that result into the amyloid dimer. Once NKA comes into play, the tachykinin neuropeptide prevents certain $A\beta_{42}$ dimer contacts at both stoichiometries (2:1 and 2:2, Figures 6B and C, respectively and Figure 11). Specific NKA interactions occur between the NKA FVGLM signature and the first hydrophobic core (K_{16}LVFFAE$_{22}$) in $A\beta_{42}$, through π-π interactions driven via the single aromatic NKA Phe residue (Figures 10D and 10E), but also preventing the inter and/or intra $A\beta_{42}$ salt bridge formation

between Asp23 and Lys28, important for the $A\beta_{42}$ self-assembly[209]. The role of Phe has been previously emphasized as a key residue in amyloid interactions, as also shown for NKB[181], with two Phe residues in the FFGLM signature.

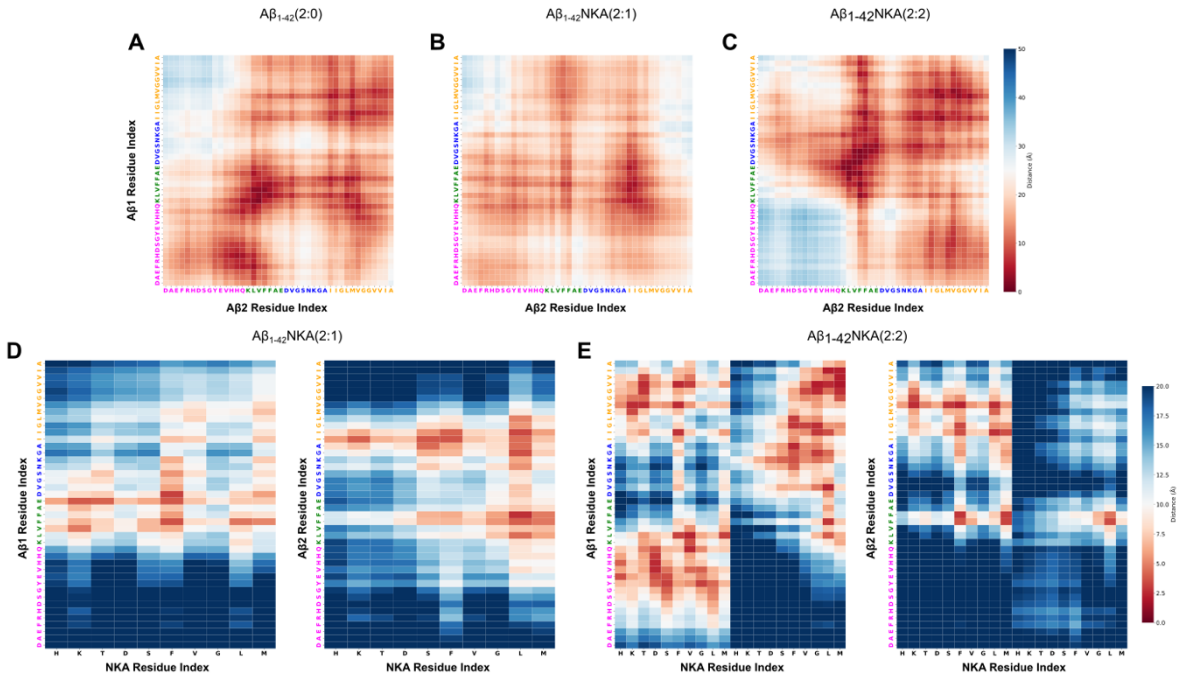


Figure 10. Residue-residue contacts map of the 1µs simulation. Intermolecular residue-residue contacts for $A\beta_{42}$ dimer interaction in the absence **(A),** at ($A\beta_{42}$:NKA, 2:1) **(B)**, and at ($A\beta_{42}$:NKA, 2:2) **(C)** stoichiometries. **(D)** NKA- Aβ contacts map for 1 NKA peptide in the presence of two $A\beta_{42}$ peptides ($A\beta_{42}$:NKA, 2:1). **(E)** NKA- Aβ contacts map for two NKA peptides in the presence of two $A\beta_{42}$ peptides ($A\beta_{42}$:NKA, 2:2). $A\beta_{42}$ domains are indicated following the color code: N-terminal unstructured domain (residues 1 to 15) in magenta; primary hydrophobic core (residues 16 to 22) in green; central core (residues 23 to 30) in blue; and C-terminal hydrophobic core (residues 342) in yellow.

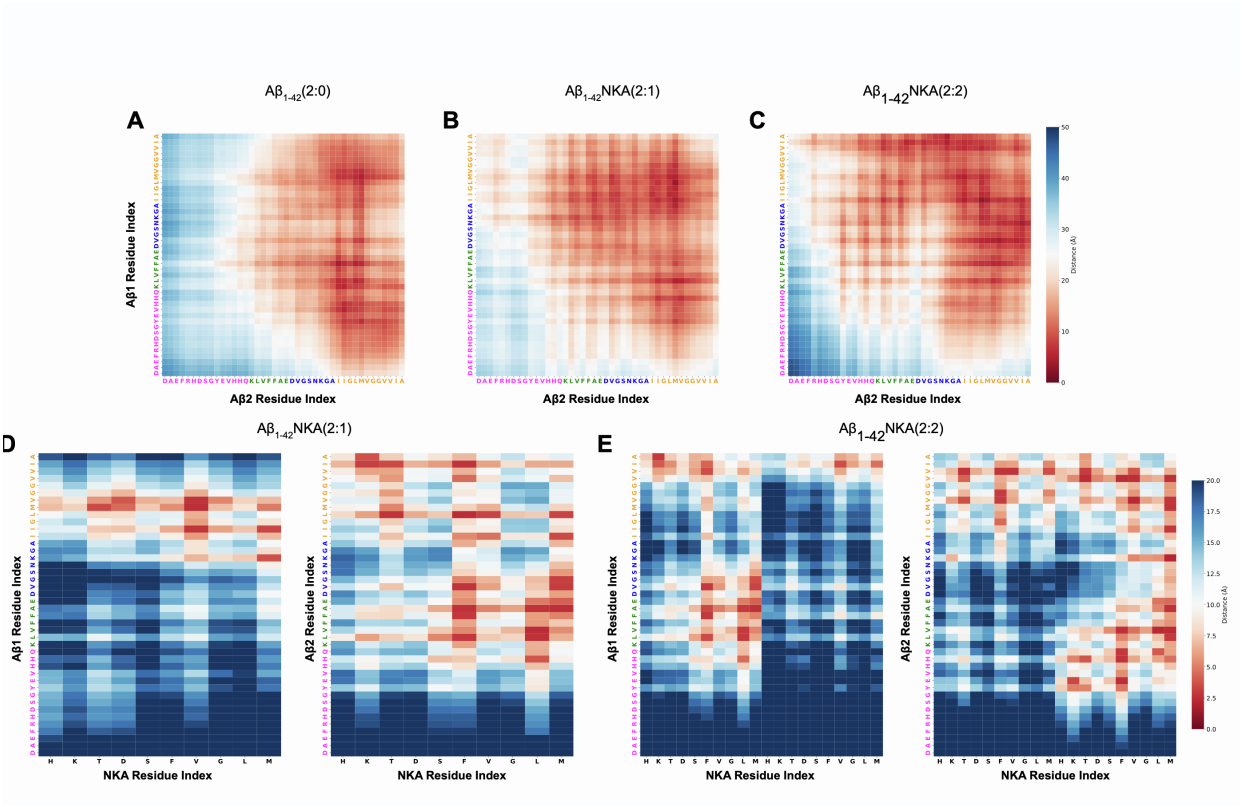


Figure 11. Residue-residue contacts map of the 1μs simulation starting with helical $A\beta_{42}$ peptide. Intermolecular residue-residue contacts for $A\beta_{42}$ dimer interaction in the absence **(A),** at ($A\beta_{42}$:NKA, 2:1) **(B)**, and at ($A\beta_{42}$:NKA, 2:2) **(C)** stoichiometries. **(D)** NKA- Aβ contacts map for 1 NKA peptide in the presence of two $A\beta_{42}$ peptides ($A\beta_{42}$:NKA, 2:1). **(E)** NKA- Aβ contacts map for two NKA peptides in the presence of two $A\beta_{42}$ peptides ($A\beta_{42}$:NKA, 2:2). $A\beta_{42}$ domains are indicated following the color code: N-terminal unstructured domain (residues 1 to 15) in magenta; primary hydrophobic core (residues 16 to 22) in green; central core (residues 23 to 30) in blue; and C-terminal hydrophobic core (residues 342) in yellow.

Phe residue is key in the NKA- $A\beta_{42}$ interaction. Accordingly, we took advantage of the computational approach to dissect the role of the single Phe residue in NKA, by the Phe-Trp conservative substitution, subsequently named NKAW (Figure 12A and Figure 7). Regarding $A\beta_{42}$ dimer secondary structure propensities, NKAW stabilizes the helical structures throughout $A\beta_{42}$ at the 2:1 and at the 2:2 stoichiometries (Figure 12B) when we use random coil $A\beta_{42}$ as starting point. In simulations using the helical $A\beta_{42}$ higher β-structure propensities are observed in the Aβ

monomers (Figure 7). The Phe-Trp substitution, allows the interaction of NKAW Trp with the $K_{16}LVFFAE_{22}$ hydrophobic core of $A\beta_{42}$ at 2:1 stoichiometry, but to a lesser extent in the 2:2 stoichiometry (Figure 13 and Figure 14 for $A\beta_{42}$ random coil and helical initial structures, respectively).

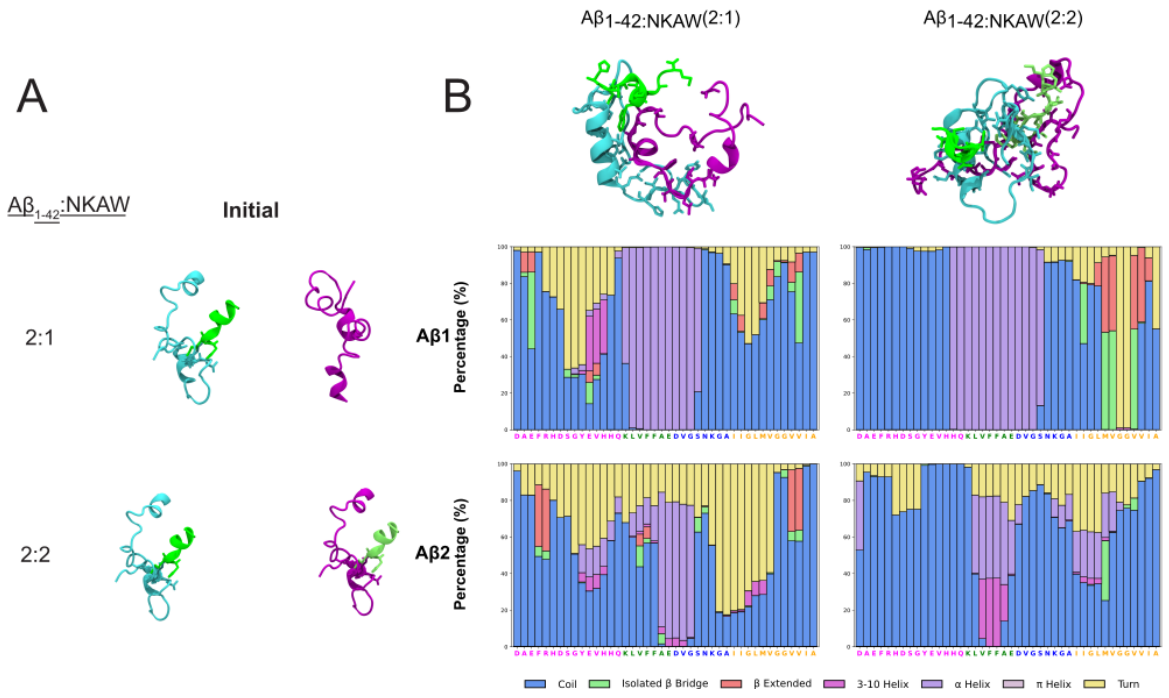


Figure 12. Secondary structure propensities of $A\beta_{42}$ induced by NKAW cross-interaction. A. Initial pose of MD simulations of $A\beta_{42}$ dimer and $A\beta_{42}$-NKAW peptide complex at indicated stoichiometries. $A\beta_{42}$ are displayed in cyan and purple and NKAW peptides are depicted in green and light green, respectively. **B.** Aβ1 and Aβ2 as $A\beta_{42}$ dimer and their secondary structure conversion with a total simulation contact time of 1 μs simulation for: $A\beta_{42}$-NKAW (2:1), and $A\beta_{42}$-NKAW (2:1). On top, snapshot of the average cluster of the last 500 ns of the MD simulation. $A\beta_{42}$ domains are indicated following the color code: N-terminal unstructured domain (residues 1 to 15) in magenta; primary hydrophobic core (residues 16 to 22) in green; central core (residues 23 to 30) in blue; and C-terminal hydrophobic core (residues 342) in yellow.

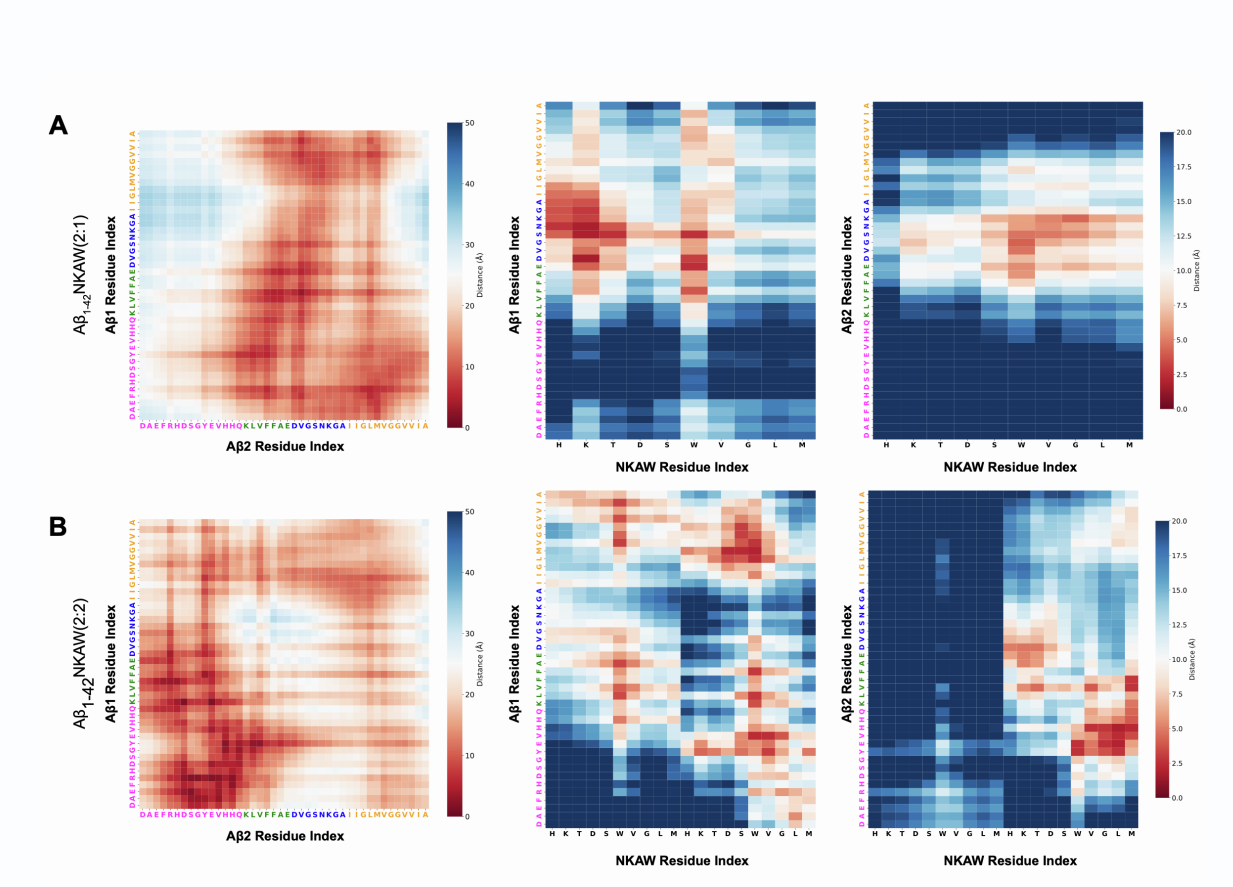


Figure 13. Residue-residue contacts map of the 1μs simulation starting with random coil $A\beta_{42}$ peptide. (A) Contacts map of $A\beta_{42}$ peptide cross-interaction with NKAW ($A\beta_{42}$:NKAW, 2:1); NKAW- Aβ contacts map for 1 NKAW peptide in the presence of two $A\beta_{42}$ peptides ($A\beta_{42}$:NKW, 2:1). **(B)** Contacts map of $A\beta_{42}$ peptide cross-interaction with NKAW ($A\beta_{42}$:NKAW, 2:2) NKA- Aβ contacts map for 2 NKAW peptides in the presence of two $A\beta_{42}$ peptides ($A\beta_{42}$:NKA, 2:2). $A\beta_{42}$ domains are indicated following the color code: N-terminal unstructured domain (residues 1 to 15) in magenta; primary hydrophobic core (residues 16 to 22) in green; central core (residues 23 to 30) in blue; and C-terminal hydrophobic core (residues 342) in yellow.

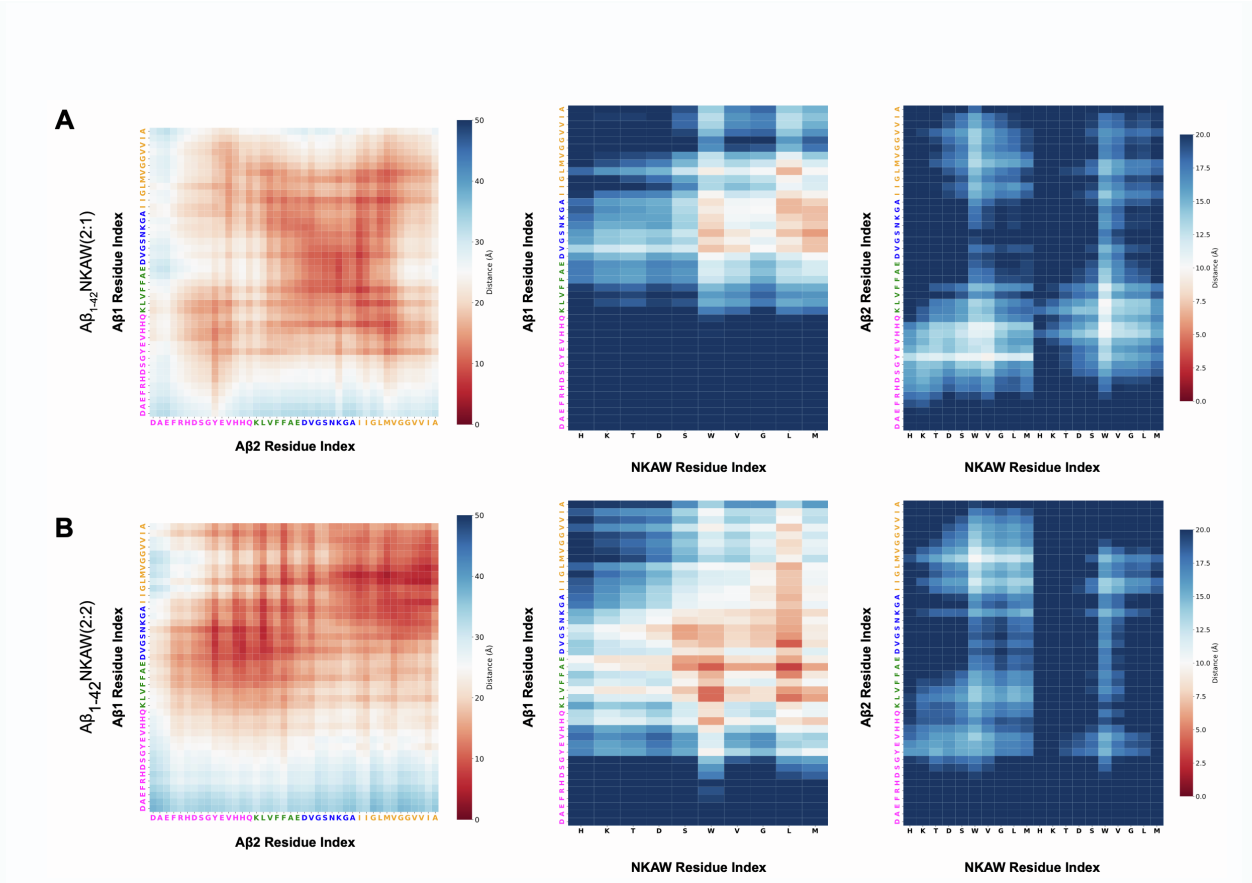


Figure 14. Residue-residue contacts map of the 1μs simulation starting with helical $A\beta_{42}$ peptide. (A) Contacts map of $A\beta_{42}$ peptide cross-interaction with NKAW ($A\beta_{42}$:NKAW, 2:1); NKAW- Aβ contacts map for 1 NKAW peptide in the presence of two $A\beta_{42}$ peptides ($A\beta_{1-42}$:NKW, 2:1). **(B)** Contacts map of $A\beta_{42}$ peptide cross-interaction with NKAW ($A\beta_{42}$:NKAW, 2:2) NKA- Aβ contacts map for 2 NKAW peptides in the presence of two $A\beta_{42}$ peptides ($A\beta_{42}$:NKA, 2:2). $A\beta_{42}$ domains are indicated following the color code: N-terminal unstructured domain (residues 1 to 15) in magenta; primary hydrophobic core (residues 16 to 22) in green; central core (residues 23 to 30) in blue; and C-terminal hydrophobic core (residues 342) in yellow.

As a summary, in Figure 8 we show the aromatic interactions driven by Phe/Trp in NKA and NKAW with Phe19 and Phe20 in $A\beta_{42}$, using random coil (Figure 15A) or helical (Figure 15B) structures. Regardless the initial conformation of $A\beta_{42}$, in the absence of NKA/NKAW, Phe19 and Phe20 of $A\beta_{42}$ monomers are able to interact through π-π stacking. When NKA/NKA comes into play,

Phe6/Trp6 reorients away one of the Phe in the 19-20 di-Phe motif, preventing a tight π-π stacking interaction between $A\beta_{42}$ monomers.

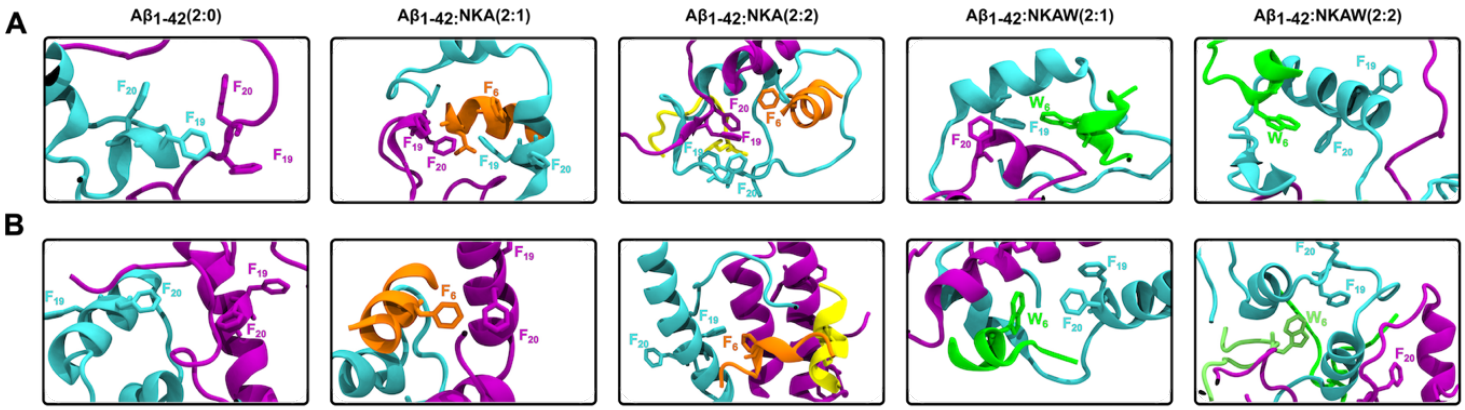


Figure 15. (A) (B) Interaction aromatic residues between $A\beta_{42}$ and NKA/NKAW. The $A\beta_{42}$:NKA/NKAW ratios are: 2:0, 2:1, and 2:2, as indicated. The interactions correspond to the simulations using the NKA/NKAW starting with $A\beta_{42}$ **(A)** random coil and **(B)** helical configurations, respectively.

Effect of NKA/NKAW interaction on the $A\beta_{42}$ amyloid pathway. First, to determine that the Phe-Trp substitution did not affect the structure of the peptide, we analyzed the circular dichroism (CD) behavior of both NKA and NKAW using thermal ramps, resulting in no significant structural differences (Figure 14). To obtain further details of the NKA/NKAW-$A\beta_{42}$ interactions, Thioflavin T (ThT) fluorescence labelling was used to monitor aggregation kinetics for $A\beta_{42}$ alone and in the presence of NKA and NKAW at $A\beta_{42}$:NKA/NKAW stoichiometries 2:1 and 2:2 (Figure 15A and B for NKA and NKAW, respectively). Regarding kinetics, the $A\beta_{42}$ samples incubated with NKA shows the highest decrease and slowing down in the amyloid formation process (Figure 16A), as shown by the $t_{½}$ parameter 12.5±0.4 h (r_{max} 1.2±0.4 h^{-1}) hours for the samples incubated with NKA at 2:1 stoichiometry, as compared to $t_{½}$ 10.5±0.4 h (r_{max} 0.2±0.0 h^{-1}) for $A\beta_{42}$ alone under the same

conditions. At 2:2 stoichiometry NKA decreases the amount of amyloid aggregation but speeding up the kinetics to $t_{½}$ 3.7±0.3 h (Figure 16A). NKAW (Figure 16B) at 2:1 stoichiometry decreased the $A\beta_{42}$ amyloid formation but speed up the aggregation kinetics to $t_{½}$ 6.4±0.7 h (r_{max} 0.3±0.1 h^{-1}), with a similar effect at 2:2 stoichiometry with kinetics of $t_{½}$ 5.2±0.4 h (r_{max} 1.2±0.4 h^{-1}). The samples resulting from the ThT kinetics, were observed by Transmission Electron Microscopy (TEM), and all the samples containing $A\beta_{42}$ show a large amount of fibrillar aggregates. Qualitatively, samples containing NKA and NKAW, showed smaller fibrillar aggregates. (Figure 17).

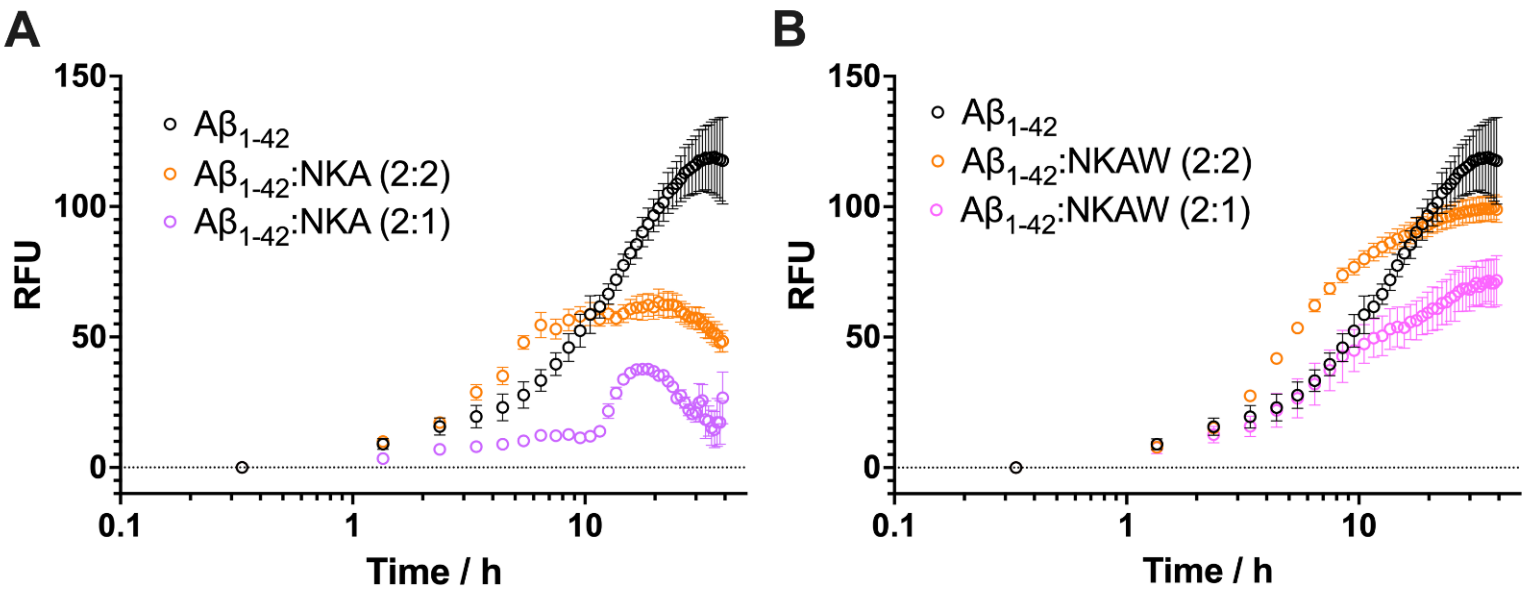


Figure 16. $A\beta_{42}$ ThT aggregation kinetics. $A\beta_{42}$ peptide fibrillation kinetics in the presence of NKA **(A)** and NKAW **(B)** peptides at different peptide ratios. 12 µM monomeric $A\beta_{42}$ peptides were incubated in 10 mM sodium phosphate buffer pH 7.4 and 40 µM ThT at +37 ºC under quiescent conditions in the absence and presence of 6 µM (2:1) or 12 µM (2:2) NKA or NKAW. The average for each condition calculated from three replicates is shown.

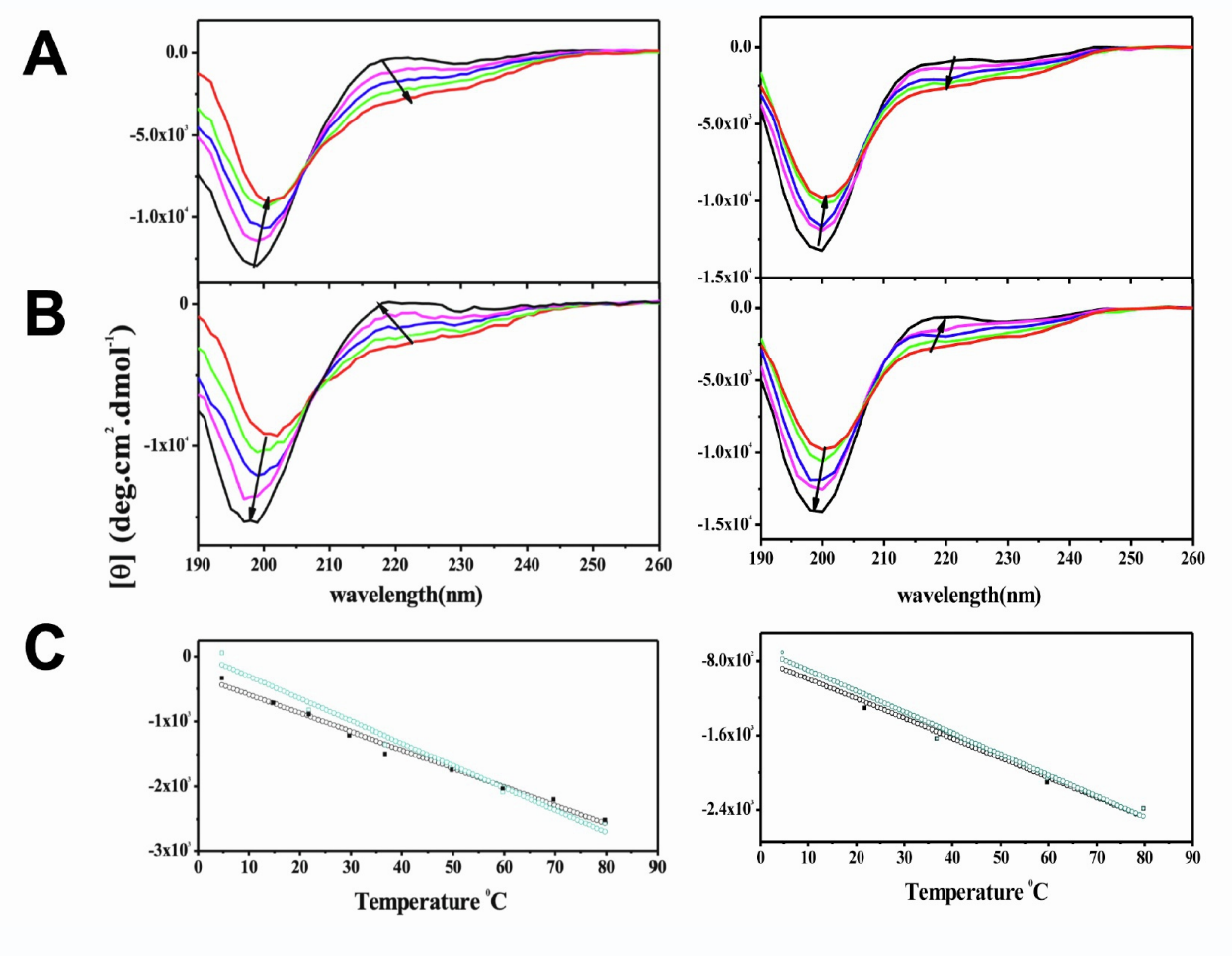


Figure 17. CD spectra of NKA (left), NKAW (right) analog recorded at increasing **(A)** and decreasing **(B)** temperatures: 5 (black), 22 (magenta), 37(blue), 60 (green) and 80 ºC (red). **(C)** Mean residue ellipticity plot at 224 nm as a function of temperature. The black open circles and cyan open circles indicate heating and cooling cycles, respectively. Note that the ellipticity is linear over a broad temperature range. In all the cases, the spectra were recorded in sodium phosphate buffer (10 mM, pH 7.0) and concentration of peptides was 100 µM.

β-sheet secondary structure of $A\beta_{42}$ was observed by CD in samples incubated for 1 hour showing, with a maximum at 203 nm and a minimum at 215 nm (Figure 18). In the presence of NKA and NKAW, the maximum/minimum for β-sheet structure was reduced in all cases (Figure 18), indicating an effect due to the presence of both peptide on secondary structure of $A\beta_{42}$.

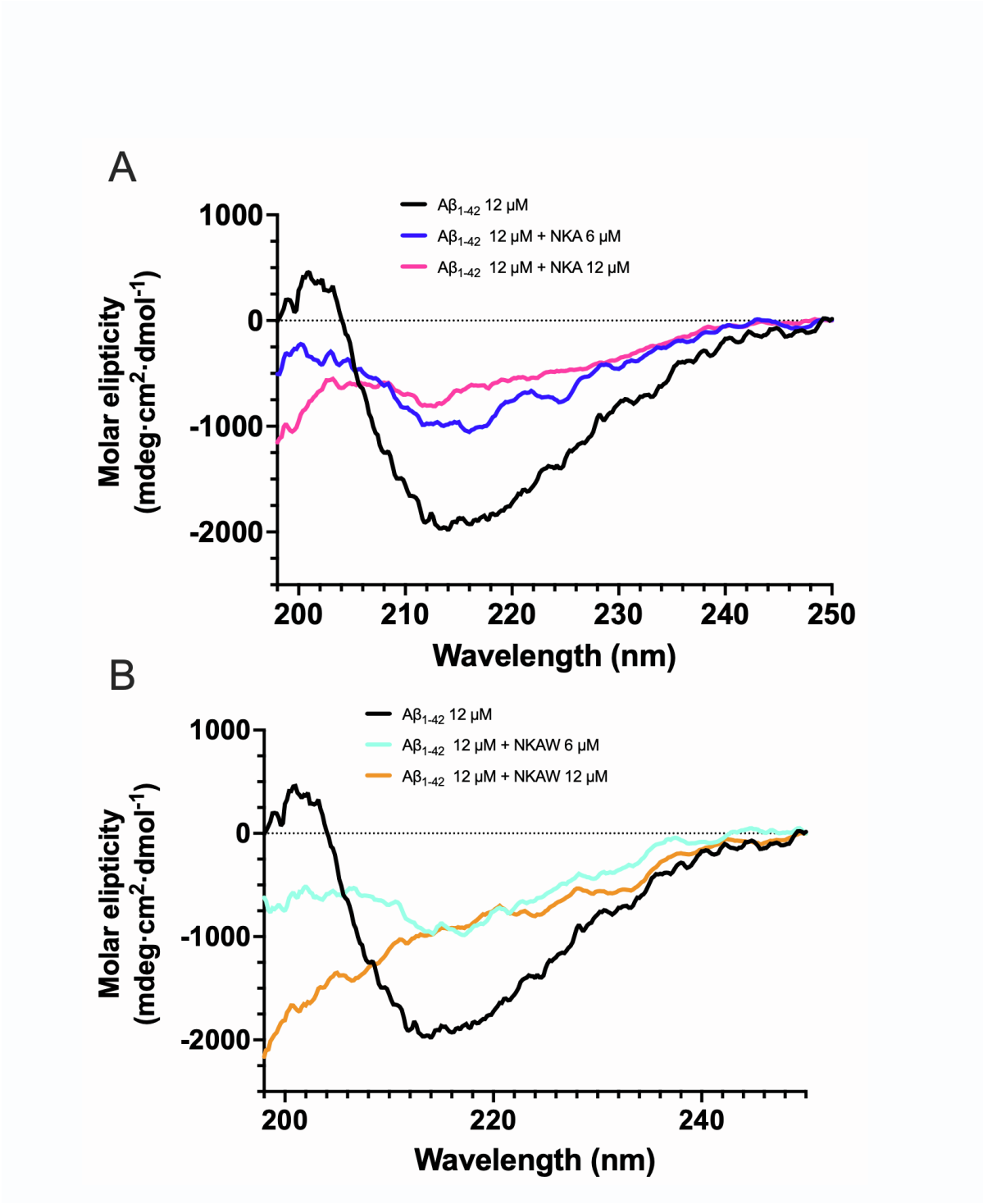


Figure 18. Secondary structure analysis of incubated mixtures. CD spectra of **(A)** $A\beta_{42}$, $A\beta_{42}$-NKA and **(B)** $A\beta_{42}$, $A\beta_{42}$-NKAW peptide mixtures at indicated stoichiometries. In all the cases, the spectra were recorded in sodium phosphate buffer (10 mM, pH 7.3).

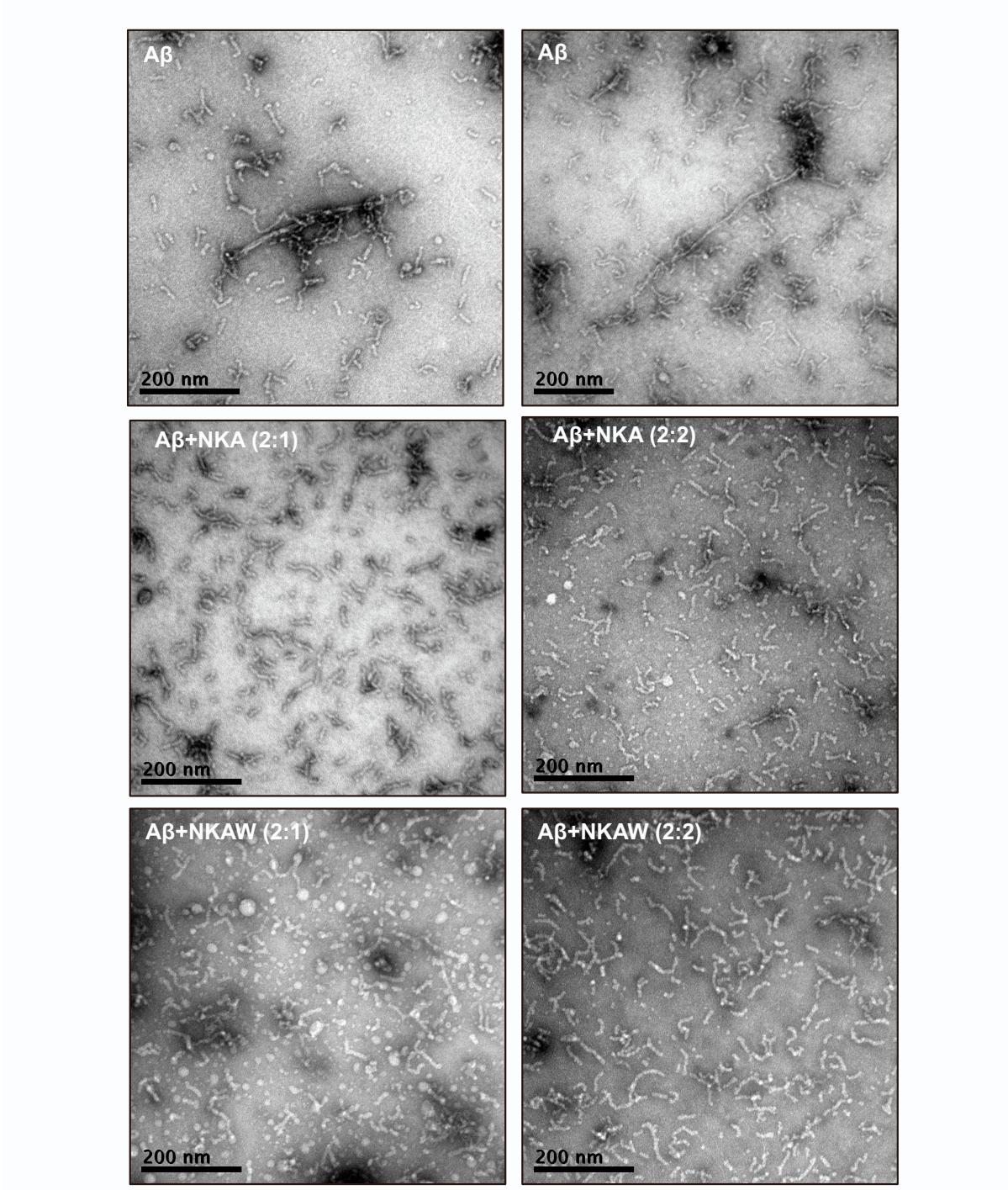


Figure 19. TEM micrographs. Negative stained samples from the final step of ThT aggregation kinetics (Figure 5 of the main text). For reference, the scale bar represent 200 nm.

Effect of the NKA- $A\beta_{42}$ interaction on cell toxicity. Peptide mixtures incubated for at least 24 h were exposed to neuroblastoma-derived cells to assess the toxicity of the aggregates using the

3-(4,5-dimethylthiazol-2-yl)-2,5-diphenyltetrazolium bromide (MTT) assay (Figure 20). Regardless of the peptide-cell interaction mechanism, 10 µM of $A\beta_{42}$ exhibit a significant toxicity of 25%, whereas neither NKA or NKAW showed significant toxicity at 5 or 10 µM. When cells were treated with the NKA- or NKAW- $A\beta_{42}$ mixture, cell viability was significantly increased back to normal levels, independently of the stoichiometry used.

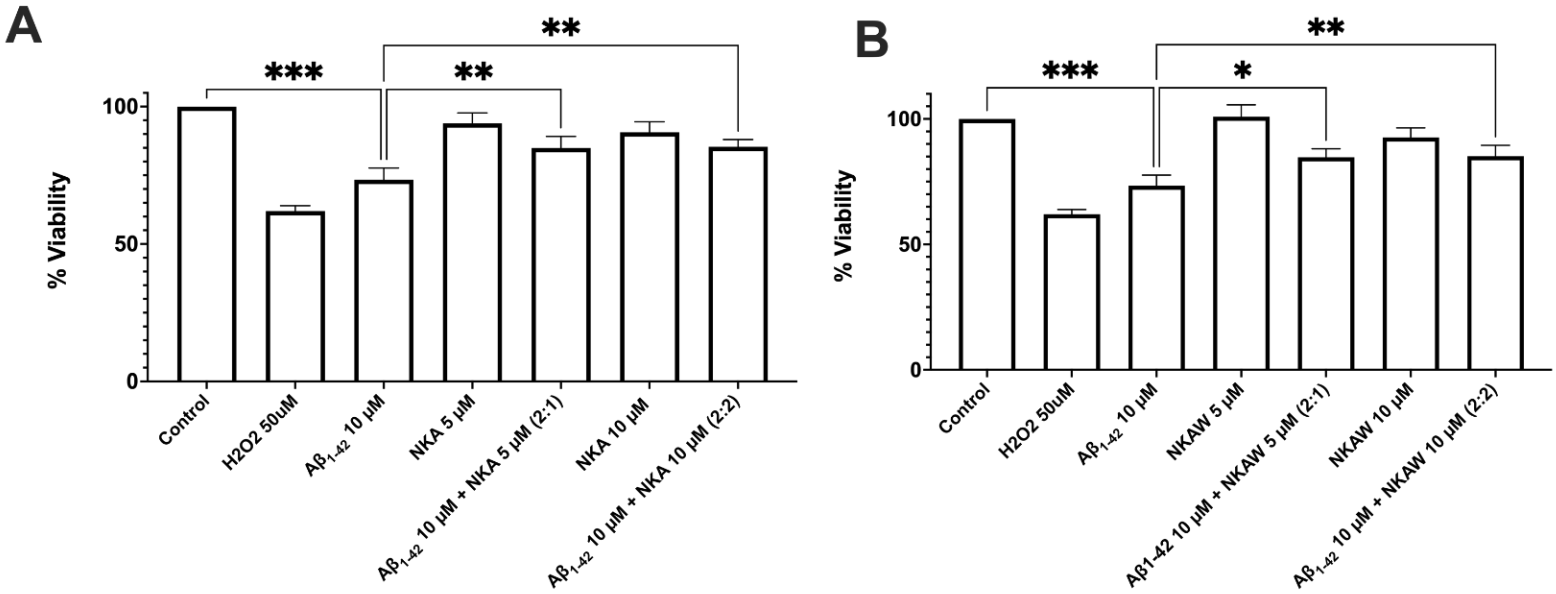


Figure 20. Amyloid-induced cell toxicity in SH-SY5Y cells. The effect on cell viability of $A\beta_{42}$ and NKA **(A)** and NKAW **(B)** was compared to untreated cells and is represented as the average of at least three independent experiments ± S.E.M. The effect on cell viability of samples from $A\beta_{42}$ incubated with NKA and NKAW at two distinct concentrations ($A\beta_{40}$:NKA/NKAW 10 µM:5 µM and 10 µM:10 µM) was compared to $A\beta_{42}$. Conditions yielding significant differences are indicated (*, $p < 0.01$; **, $p < 0.001$; ***, $p < 0.0001$).

DISCUSSION

Amyloid production takes place throughout an individual's lifespan primarily originating from neurons, and with aging as primary risk factor for AD. Peptide cross-interactions, such as Aβ-TKs[96,210–212], Aβ-dynorphins[98], and others[62,64,98,180,213,214], act as physiological buffers or enhancers

for amyloid aggregation. The existence of an age-related pathophysiological condition, characterized by predominant amyloid aggregation within the brain, suggests a potential disruption in peptide cross-interaction homeostasis. This disturbance may lead to the surpassing of the amyloid threshold, consequently exacerbating the onset of the disease beyond reversible limits. Thus, it is key to identify endogenous peptides as Aβ counterplayers to design strategies for the prevention and inhibition of AD development at all levels. Recent findings demonstrate that dynorphin neuropeptides play a crucial role in inhibiting dimer formation, thereby preventing the initiation of the amyloid cascade and serving as neuroprotectors[98], and other neuropeptides, such as NKB, have been found to avoid the Aβ dimer formation[181]. It is reasonable to consider that exists a physiological inhibition of amyloid aggregation in systemic tissues and the brain, until the concentration of amyloid exceeds a specific threshold leading to onset of pathology. NKA is especially relevant to understand the brain-gut axis mechanism[63], specifically in the brain. NKA-Aβ cross-interaction, which has not been so extensively studied compared to other TKs, is likely to occur at physiological level[11-13,18,27,44,45]. Previous studies show effect of NKA on Aβ toxic effect at cellular level[42], despite later biochemical and biophysical characterization failed to show any interaction between a Trp-analog for NKA (extra Trp added at the C-terminus) and $A\beta_{40}$[27].

Here, to study the NKA-Aβ cross-interaction, we have used peptides acetylated at the C-terminus (both computationally and experimentally), and we use a Trp variant to assess the role of Phe in NKA prior assessment that the secondary structure of the peptide is not affected by the conservative substitution. Then, we complement two approaches, first the computational approach through MD simulations to assess putative molecular determinants in the Aβ dimer

formation, and how the NKA peptide influences this interaction. Previous studies point to the role of the Phe-Phe motif in NKB in stabilizing the NKB- Aβ cross-interaction through π-π stacking interactions[14,17]. For NKA, which has a single Phe residue, we observe a similar effect, indicating that interpeptide Phe-Phe π-π stacking is important for the Aβ self-assembly, but also for Aβ cross-interactions. To assess the role of the single Phe in NKA in the NKA- Aβ cross interaction, we substitute the Phe for a Trp, trying to minimally disturb the cross-interaction, and we observe the NKAW follows the same trend. Our computational results argue peptides containing aromatic residues as stabilizers against amyloid self-assembly[215].

Second, we use biophysics and cell biology to assess the macroscale effects of the NKA- Aβ cross-interaction. Secondary structure studies using CD indicate between both peptides, and ThT kinetics show that NKA presence influence the Aβ aggregation kinetics. The NKA influence is also shown at the cellular level in MTT cell viability assays. The conservative Phe-to-Trp mutation does not affect significantly the in vitro and in cellulam results. Altogether, our results add up to other studies regarding Aβ-neuropeptides cross-interactions[10,12-14,17,18,26,27,32,41-43], and show that the premise of the least studied NKA-Aβ cross-interaction is not unlikely, and that it should be further considered to understand the pathophysiological implications in AD and neurodegenerative disorders.

Here we show the molecular mechanisms of the NKA-$A\beta_{42}$ cross-interaction. Our study on NKA leads to the following conclusions: i) NKA influences the formation of the cross-β structure by shielding aromatic and hydrophobic interactions between Aβ monomers in a concentration dependent manner. ii) NKA efficiently affects the initial seeding of the formation of early-stage nonfibrillar Aβ dimers at both Aβ:NKA ratios of 1:1 and 2:1, and the role of the single Phe in NKA

is predominant. NKA establishes stable aromatic, hydrophobic, and electrostatic interactions with an Aβ monomer, and the Trp substitution is not as efficient. iii) The computational observations agree with in vitro ThT aggregation kinetics, and in cellular viability experiments. As a global conclusion, strategic integration of experimental and computational methodologies is required to overcome existing challenges associated with amyloid polymorphism and the relatively brief lifetimes of specific amyloid structures.

CHAPTER II

*This chapter is based on the following published article: Habibnia, M. et al. Biophysical analysis of angiotensin <scp>II</scp> and amyloid-β cross-interaction in aggregation and membrane disruption. FEBS Lett. **600**, 109–118 (2026). https://doi.org/10.1002/1873-3468.70185[101]. The content contains minor revisions for consistency with the overall thesis narrative.

Biophysical Analysis of Angiotensin II and Amyloid-β Cross-Interaction in Aggregation and Membrane Disruption[101]

Summary

Amyloid-β (Aβ) peptide aggregation, is a hallmark of Alzheimer's disease (AD) pathology. Endogenous peptides occupying the same physiological environment may influence Aβ aggregation through direct interactions. This study investigated the cross-interaction between Aβ and angiotensin II (AngII), a neuropeptide of the renin–angiotensin system, using biophysical in vitro aggregation assays, membrane disruption tests, and in silico docking to model the interaction. Thioflavin T fluorescence, circular dichroism spectroscopy, and Congo Red thermal shift assays showed that AngII modestly reduced Aβ aggregation and membrane disruption in a dose-dependent manner. Liposome leakage assays indicates that AngII decreases the membrane disruption potential of aggregated Aβ peptides. ThT and circular dichroism, aided with modeled heteroaggregates show that AngII may bind preferentially to disordered Aβ conformers, with reduced affinity for α-helical and β-sheet structures. Altogether the data presented here suggests that AngII may modulate early amyloidogenic events in a concentration-dependent manner which may be important to amyloid homeostasis.

Keywords

Alzheimer’s disease; amyloid cascade pathway; renin-angiotensin system; amyloid β peptide; angiotensin II; peptide-peptide cross-interactions

Introduction

The amyloid beta (Aβ) cascade hypothesis and the cholinergic hypothesis are two well-documented explanations for the pathogenesis of Alzheimer's disease (AD)[216–218]. The Aβ cascade hypothesis describes the development of senile plaques, resulting from the accumulation of Aβ peptides (39 to 42 residues) in the central nervous system (CNS)[216]. This aggregation and deposition occur due to an imbalance between the production of Aβ peptides from amyloid precursor protein (APP) and their clearance. $A\beta_{40}$ and $A\beta_{42}$ are the main products of APP processing, with $A\beta_{42}$ being more fibrillogenic and a major component of amyloid plaques, despite $A\beta_{40}$ being more abundant in both healthy and AD patients[219]. The dynamic process of Aβ aggregation is influenced by neuropeptides, which regulate neuronal and vascular functions[220,221]. Peptides like dynorphins and tachykinins interact with Aβ, preventing toxic early-stage Aβ dimers and further fibril development, which beyond the potential therapeutic implications of peptide design, open an important avenue on neuropeptide proteasis as a mechanism to understand and control amyloidogenesis through heterotypic interactions[97,98,181]. The renin-angiotensin system (RAS) traditionally regulates blood pressure and fluid balance but also influences brain functions such as learning, memory, and neuronal plasticity, relating to the cholinergic hypothesis[222]. Angiotensin II (AngII), a key peptide in the RAS, interacts with G-protein coupled receptors (GPCRs) AT1, AT2, and AT4, to modulate cognitive processes[223]. Recent

research suggests that AngII interaction with Aβ may exacerbate neurodegenerative processes by promoting oxidative stress, inflammation, and neuronal apoptosis[224,225].

Angiotensin II (AngII) and amyloid-beta (Aβ) are co-expressed in brain regions vulnerable to Alzheimer's disease (AD) pathology, such as the hippocampus and cortex, where their interaction may exacerbate neurodegenerative processes[226]. AngII has also been implicated in modulating Aβ metabolism through its influence on degrading enzymes like neprilysin and angiotensin-converting enzyme (ACE), which are critical for Aβ clearance[227,228]. AngII stands out due to its dual role in vascular and cognitive regulation, its structural compatibility for direct interaction with Aβ, and its therapeutic relevance given the clinical use of RAS inhibitors in AD-related contexts[228–230].

Proteostasis of neuropeptides coexisting with Aβ peptides appears crucial, as key potential interactors and modulators of the amyloidogenic pathway. A multitude of physiological factors can either promote or inhibit the amyloid cascade process, depending on the physiological balance. The study of peptide cross-interactions not only enhances our understanding of the pathophysiology of neurodegenerative disorders but also opens avenues for the rational design of peptide-based therapeutic and diagnostic/biomarker strategies.

In the present study, we combine in vitro biophysical characterization with computational docking to investigate the cross-interaction between AngII and Aβ. This approach aims to elucidate the potential influence of AngII on the Aβ amyloid pathway, contributing to a better understanding of how endogenous peptides may modulate Aβ aggregation dynamics.

Materials and Methods

Peptides and sample preparation

Recombinant human $A\beta_{40}$ was purchased from Alexotech (Umeå, Sweden), synthetic $A\beta_{42}$ was purchased from JPT (Germany), and synthetic human angiotensin II peptide was purchased from pepMic (Jiangsu, China). Aβ peptides were dissolved in 10 mM NaOH at pH 11, aliquoted and kept frozen until further use. High-monomer content stock samples were prepared as previously described[98] by dissolving Aβ peptides in 10 mM NaOH, pH 11, at a concentration of 225 µM and sonicated in an ice-bath for at least three minutes. Ang II stock solution was dissolved in 10 mM NaPi buffer, pH 7.4, at a concentration of 2500 µM. Peptide concentrations were determined initially by weight and confirmed spectrophotometrically by absorbance at 215 nm in a NanoDrop device. For experiments, $A\beta_{40}$ and $A\beta_{42}$ samples were kept on ice and diluted to the specified concentration (10-25 µM) in 10 mM sodium phosphate buffer (final pH in the 7.2-7.4 range). All samples were kept on ice until the beginning of the experiment. Aged samples for liposome leakage experiments were prepared by incubating peptide samples for 30 hours at 37 ºC [231].

Thioflavin T aggregation kinetics

40 µM Thioflavin T (ThT, Sigma Aldrich, Cat. N. T3516). $A\beta_{40}$ and $A\beta_{42}$ samples were mixed with AngII at the specified Aβ:AngII ratios of 1:0.1, 1:1, and 1:10, yielding AngII final concentrations of 1 µM, 10 µM, and 100 µM, respectively. Fluorescence intensity was measured in triplicates using a 440 nm excitation filter and 520 nm emission filter at 37 ºC with 86 rpm double orbital shake during 5 minutes before each cycle (shaking) for $A\beta_{40}$ and 30 s before each cycle (no shaking) for $A\beta_{42}$ in a FLUOstar Optima microplate reader (BMG LABTECH, Germany). The no shaking/shaking variable was introduced to keep the sigmoidal spectra within the same time window of 40 h per

experiment. The plots correspond to at least three independent experiments of four replicates per condition. The ThT fluorescence kinetic traces were analyzed using sigmoidal curve fitting according to Eq.5, allowing the parameters aggregation halftime,t and the maximum growth rate, r_{max}, to be determined.

$$F(t) = \frac{Fmax}{1+\exp[r_{max}\times(\tau - t)]} \qquad \text{Eq. 5}$$

Congo red thermal ramps

$A\beta_{40}$ and $A\beta_{42}$ samples at final concentration of 10 µM were mixed with AngII at a final concentration of 50 µM to yield an Aβ:AngII ratio of 1:5 using Congo red (CR, Labkem, Spain) at 2 µM as amyloid indicator in 10 mM sodium phosphate buffer pH 7.2–7.4. Thermal stability of the samples was recorded by measuring the 250-700 nm absorbance, average time of 0.166 s, 1 nm data interval, and an scan rate of 361.446 nm/min, using a Cary Bio3 spectrophotometer from 25°C + 5°C up to 75°C, allowing all the samples equilibrate separately at each temperature for 5 minutes before spectra acquisition, with an estimated heat rate of 40 $K{\cdot}h^{-1}$. After the final scan at 75°C, samples were allowed to cool down to 25°C and were equilibrated for 5 minutes before measuring the absorbance spectrum again to assess reversibility of the transitions. To obtain melting temperature (T_m) values, the ratio between 540 nm and 400 nm absorbance was calculated for the data of 2 independent experiments, and the scattering plot was analyzed using a two-state sigmoidal curve fitting.

Liposome leakage experiments

1-palmitoyl-2-oleoyl-sn-glycero-3-phosphocholine (POPC, Affymetrix, California, USA), 1-Palmitoyl-2-Oleyol-sn-Glycerol-3-[Phosho-rac-(1-glycerol)] (POPG, Avanti, Alabama, USA), and cholesterol (Chol, Sigma-Aldrich, Missouri, USA) were dissolved in $CHCl_3$/MeOH (2:1 v/v) solvent to obtain the following mixtures and molar ratios; POPC , POPC:POPG, 7:3, and POPC:POPG:Chol, 6:3:1. Liposomes were prepared as described previously [232]. In brief, the previous lipídic organic solutions were rotovapored to obtain a thin film. Multilamellar liposomes at a total lipid concentration of 10 mM were obtained after hydrating the lipid film with phosphate buffer 10 mM pH 7.2 containing 2 mM 8-hydroxypyrene-1,3,6-trisulfonic acid (HPTS). Finally, the vesicles were downsized by progressive extrusion through 800, 400, 200 and 100 nm pore polycarbonate membranes. Liposome size Distribution was characterized by dynamic light scattering (DLS, Nanotrac Wave, Microtrac, USA) yielding average radius size of 120 nm for POPC and 90 nm for POPC:PG and POPC:PG:Chol, respectively. Removal of non-encapsulated HPTS was done by size-exclusion chromatography (SEC) in Sephadex G-25 PD-10 columns (Amersham Biosciences). P-xylene-bis-pyridinium bromide (DPX, Fisher Scientific) at a final concentration of 5 µM was added to SEC-purified liposomes giving a final concentration of 100 µM. HPTS encapsulated liposomes with DPX were subsequently loaded in black 96-well plate clear flat bottom. The HPTS fluorescence as a function of time and subsequent quenching by DPX upon liposome release of the dye was measured using 420 nm and 520 nm excitation and emission wavelengths respectively in a FLUOstar Optima microplate reader (BMG LABTECH, Germany). The effect of the peptides was evaluated by adding them to the wells at a final concentration of 5 µM and after 4,000 s the full fluorescence quenching was assessed by liposome solubilization

by adding Triton X-100 (Sigma-Aldrich) at a final concentration of 5 µM. The plots correspond to the average of three independent experiments.

Peptide-peptide docking

Peptide-peptide docking was performed using FlexPepDock server, a peptide docking tool in the Rosetta Online Server (ROSIE)[233–235]. Docking was performed against six different Aβ structures and conformations, with PDB codes: $A\beta_{40}$ random coil 2LFM [236], $A\beta_{40}$ α-helix 1BA4[237], $A\beta_{40}$ β-sheet 8FF2[238], $A\beta_{42}$ random coil 6SZF[239], $A\beta_{42}$ α-helix 1Z0Q[240], and $A\beta_{42}$ β-sheet 5OQV[241]. CtHSA structure with PDB code 5FUO [242] was used. Angiotensin II was modeled using AlphaFold3 [243]. The receptor backbone was minimized previously to the docking, generating 1,000 structures with both the high resolution and low-resolution protocols.

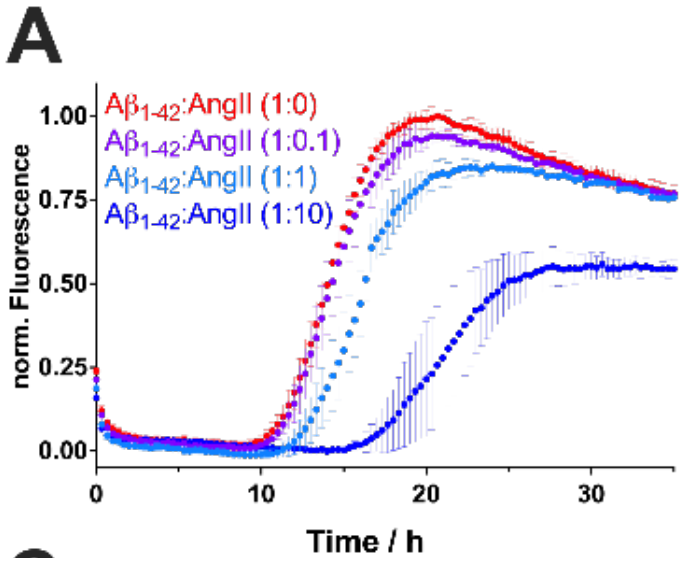
Results

Amyloid-β (Aβ) aggregation into oligomers and fibrils is a hallmark of Alzheimer's disease (AD), with monomeric Aβ acting as a nucleation seed in early aggregation phases. We hypothesized that endogenous peptides sharing the same physiological environment as Aβ may influence its aggregation pathway. To explore this, we characterized the cross-interaction between Aβ and angiotensin II (AngII), a RAS peptide, using biophysical methods to assess aggregation in vitro and in silico methods to model putatively the heterotypic interaction.

AngII modulates Aβ aggregation in vitro

To experimentally validate these predictions, we monitored Aβ fibrillization using Thioflavin T (ThT) fluorescence. To speed up the $A\beta_{40}$ kinetics and to be able to observe the whole aggregation

levels than for $A\beta_{42}$ in the same time window, the $A\beta_{40}$ sample was under higher shaking conditions than $A\beta_{42}$, resulting in noisier kinetics (Figure 21A). For $A\beta_{40}$, AngII reduced final ThT fluorescence amplitude in a concentration-dependent manner, though kinetic parameters (lag time t and growth rate r_{max}) remained largely unchanged (Figure 22, Table 4). In contrast, $A\beta_{42}$ aggregation was more sensitive to AngII (Figure 21A, Table 4), with both amplitude and kinetics affected. At 1:1 and 1:10 Aβ:AngII ratios, ThT signal decreased to 0.84 and 0.55, respectively, with corresponding reductions in τ and r_{max}. The t is decreased to ca. 16 and 21 h, and the r_{max} kinetic slope is lowered to ca. 0.9 h^{-1} and 0.6 h^{-1}, when the Aβ:AngII ratios are 1:1 and 1:10, respectively, indicating a dose-dependent inhibition of fibril formation (Table 4). For following experiments, we have chosen concentrations between the 1:1 and 1:10 ratios as the ones where changes are more evident.



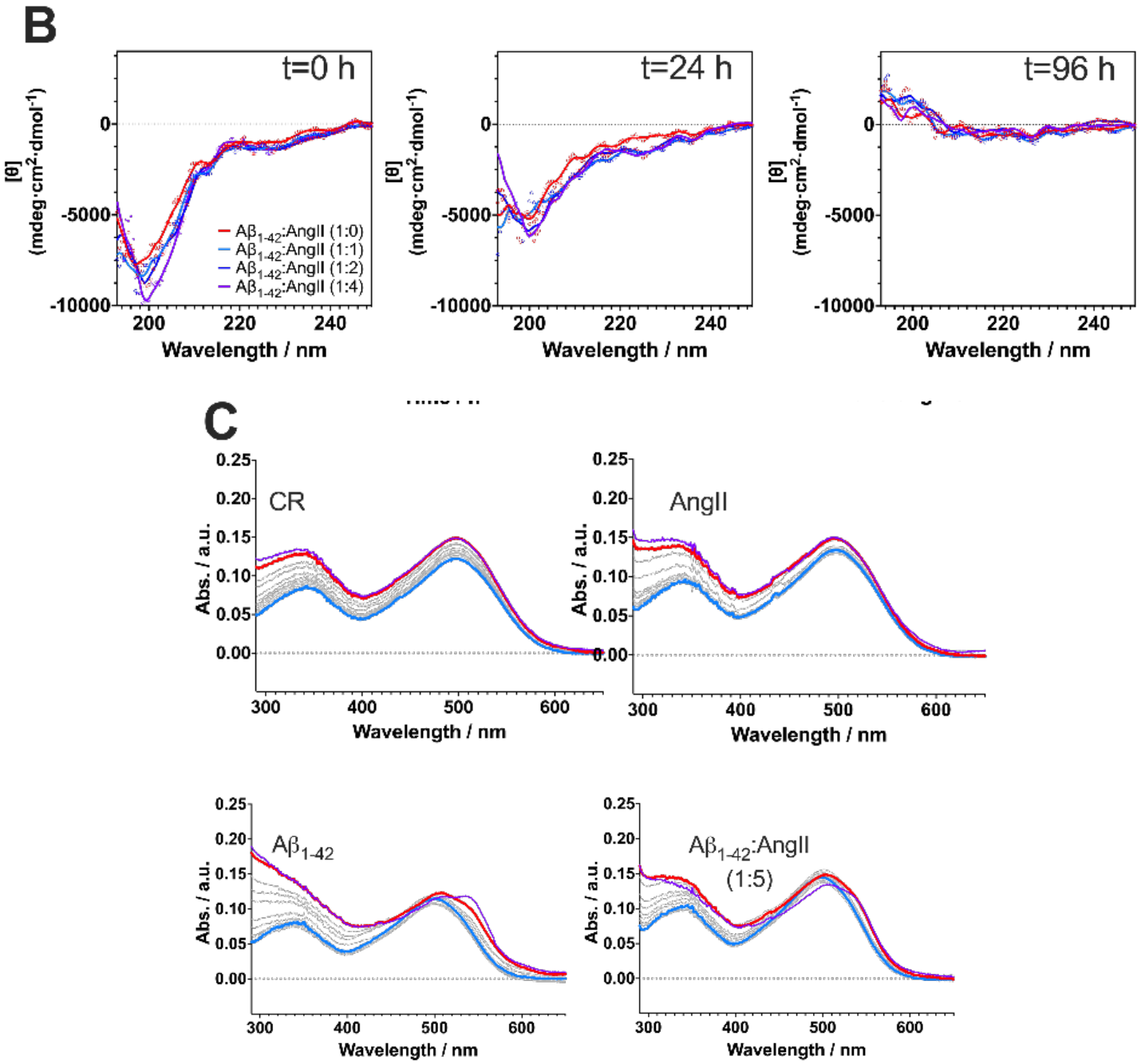


Figure 21. Fibril and amyloid formation. **A.** Attenuated Ab_{42} peptide fibrillization kinetics in the presence of AngII peptides. 10 µM of Ab peptides were incubated in 10 mM sodium phosphate buffer pH 7.4 and 40 µM ThT at +37 ºC, respectively in the absence and presence of AngII peptide at the indicated ratios (n = 4 independent measurements; error bars represent S.E.M.). **B.** Representative CD spectra of Ab_{42} peptide following a fibrillization kinetics in 10 mM sodium phosphate buffer pH 7.4 incubated at +37 ºC for 96 h (time points 0, 24 and 96 h). **C.** Congo red (CR) binding to Ab amyloid species in thermal dependent ramps. 2 independent experiments were performed (n=2). Blue spectrum corresponds to 25ºC; grey spectra represent thermal transitions

from 30°C to 70°C in 5°C increments; red spectrum corresponds to 75ºC; purple line corresponds to the 25ºC spectrum after cooling down from 75ºC.

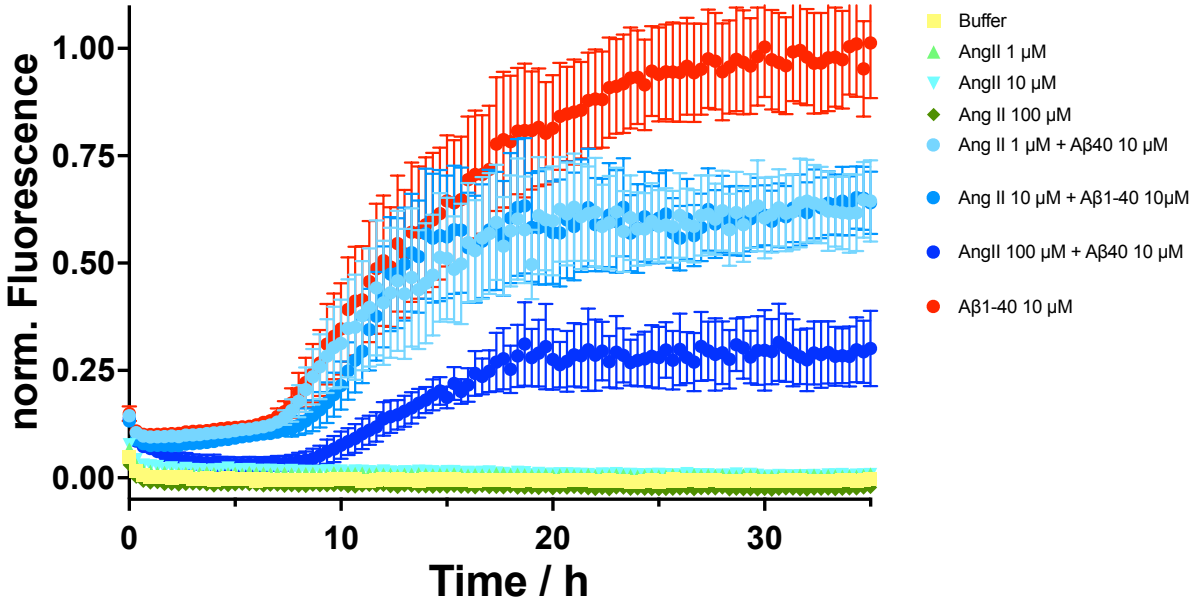


Figure 22. Fibril and amyloid formation. Attenuated Ab_{40} peptide fibrillization kinetics in the presence of AngII peptides. 10 µM of Ab peptides were incubated in 10 mM sodium phosphate buffer pH 7.4 and 40 µM ThT at +37 ºC, respectively in the absence and presence of AngII peptide at the indicated ratios. AngII only and buffer only controls are included for reference (n = 4 independent triplicate measurements; error bars represent S.E.M.).

Table 3. Sequence and properties of the peptides used in this study**.**

Peptide	Primary sequence	MW	Charge	GRAVY Index
Ab_{40}	DAEFRHDSGYEVHHQKLVFFAEDVGSNKGAIIGLMVGGVV	4,329.8	-3	0.06
Ab_{42}	DAEFRHDSGYEVHHQKLVFFAEDVGSNKGAIIGLMVGGVVIA	4,514.1	-3	0.20
AngiotensinII	DRVYIHP**F**[a]	1,046.2	0	0.32

Table 4. Phenomenological parameters determined from sigmoidal curve fitting of the kinetic traces of amyloid aggregate formation shown in Figure 21A and Figure 22.

	ThT fluorescence amplitude[a]	**t (h)**	**r_{max} (h^{-1})**
Ab_{40}:AngII (1:0)	1.00 ± 0.04	12.49 ± 0.75	0.25 ± 0.04
Ab_{40}:AngII (1:0.1)	0.62 ± 0.03	9.98 ± 0.86	0.29 ± 0.07
Ab_{40}:AngII (1:1)	0.62 ± 0.02	10.66 ± 0.64	0.41 ± 0.13
Ab_{40}:AngII (1:10)	0.30 ± 0.02	12.72 ± 0.98	0.32 ± 0.11
Ab_{42}:AngII (1:0)	0.99 ± 0.01	13.55 ± 0.17	0.99 ± 0.13
Ab_{42}:AngII (1:0.1)	0.94 ± 0.01	13.78 ± 0.18	0.95 ± 0.12
Ab_{42}:AngII (1:1)	0.84 ± 0.01	15.54 ± 0.16	0.86 ± 0.10
Ab_{42}:AngII (1:10)	0.55 ± 0.02	20.85 ± 0.37	0.57 ± 0.10

[a] Values represented in fractions of Ab peptide alone (1.00)

Secondary structure of the $A\beta_{42}$ as a function of time was followed using CD spectroscopy. At initial stages, $A\beta_{42}$ shows a predominant random coil (unordered structure, Figure 21B time 0 h) which due to the aggregation process leads to a mixture of structures and a time-dependent loss of CD signal which leads to the onset of positive signal in the 190-200 nm region (close to 0 ellipticity at time 24 h, and over 0 ellipticity at 96 h). AngII reduces in a very subtle fashion the loss of random coil structure and the onset of positive ellipticity values in the 190-200 nm region, which is concentration dependent, since at $A\beta_{42}$:AngII of 1:4, the random coil spectrum is clearly visible with a negative peak at between 190 and 200 nm at time 24 h (Figure 21B). In the time range when the aggregation has reached the plateau (Figure 21A), the CD structure for $A\beta_{42}$ alone or in the presence of AngII becomes almost indistinguishable (Figure 21B time 96 h). AngII

peptides at the chosen concentrations have almost no ellipticity signal (Figure 23), so most of the CD contribution in Figure 21B is due to changes in $A\beta_{42}$ peptide.

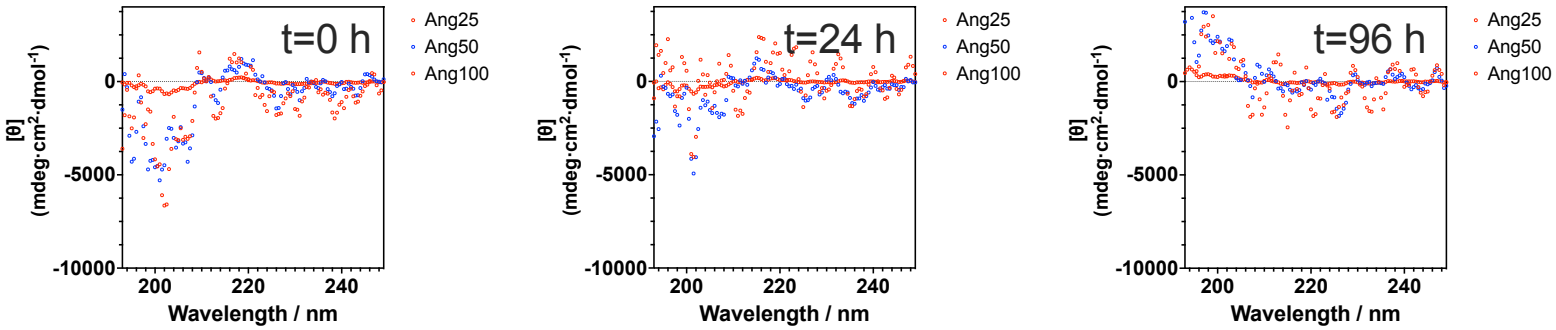


Figure 23. CD secondary structure spectra of AngII peptide at the indicated concentrations. CD spectra of AngII peptide at the indicated concentrations (25 µM; 50 µM; 100 µM) in 10 mM sodium phosphate buffer pH 7.4 incubated at +37 ºC for 96 h (time points 0, 24 and 96 h).

Thermal stability of Aβ aggregates in the presence of AngII

Congo Red (CR) absorbance was used to assess thermal-induced amyloid formation. $A\beta_{42}$ (Figure 21C) but not $A\beta_{40}$ (Figure 24) showed temperature-dependent amyloid formation, which has been previously described, evidenced by a red-shifted shoulder at 540 nm (Figure 21C). The scattering plot of the ratio of two distinctive CR wavelengths as shown by Klunk et al. [244] (i.e. 400 and 540 nm, Figure 21C) shows that although no amyloid shifts are observed for most of the samples in Figure 21C and Figure 24, the T_m of the process is affected whether AngII is present or not (Figure 24C and Table 5). CR-free shows T_m of ca. 70 ºC and when AngII is present shifts down the Tm to ca. 65ºC. When either $A\beta_{40}$ or $A\beta_{42}$ are in the system, T_m as an indicator of amyloid formation is reduced to ca. 60 and 53ºC, respectively. When AngII is added, this T_m is increased

(amyloid onset delay) to ca. 66ºC for $A\beta_{40}$ and 56ºC for $A\beta_{42}$ (Table 5). For $A\beta_{42}$ the effect of the presence of AngII on $A\beta_{42}$ thermal-dependent amyloid formation is also shown by the smaller red-shift shoulder in CR absorbance (Figure 21B). In the presence of AngII, this red shift was attenuated, and the T_m for the CR-amyloid bound species increased from ~53°C to ~56°C for $A\beta_{42}$, and from ~60°C to ~66°C for $A\beta_{40}$ (Figure 24, Table 5). For $A\beta_{40}$ cooling the temperature down does not show any dramatic changes, reinforcing the idea that no amyloid formation occurs, which is still more evident for $A\beta_{42}$ with a strong red-shift shoulder in CR absorbance after cooling the system back down to 25ºC (Figure 21C). These results support a stabilizing effect of AngII on Aβ, particularly in early aggregation states.

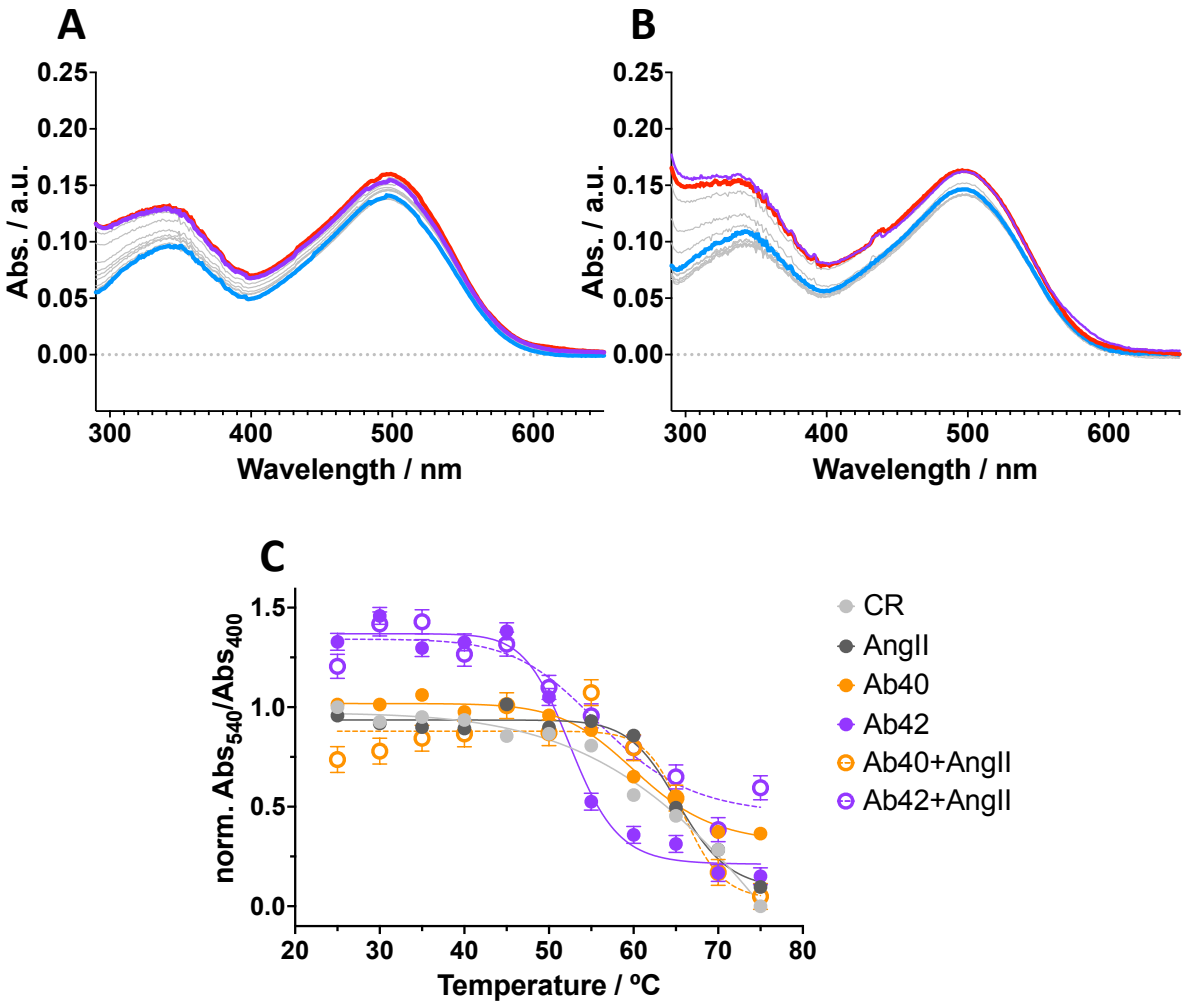


Figure 24. Congo red (CR) binding to $A\beta_{40}$ in thermal dependent ramps. **A.** Congo red (CR) binding to $A\beta_{40}$ in thermal dependent ramps. **B.** Congo red (CR) binding to $A\beta_{40}$ in the presence of AngII (Aβ :AngII 1:5) thermal dependent ramps. Blue spectrum corresponds to 25ºC; grey spectra represent thermal transitions from 30°C to 70°C in 5°C increments; red spectrum corresponds to 75ºC; purple line corresponds to the 25ºC spectrum after cooling down from 75ºC.**C.** $A\beta_{40}$ (orange line, filled circle) curve drops moderately with temperature, reflecting the thermal stability of the CR-$A\beta_{40}$ complex**.** $A\beta_{42}$ (purple line, filled circle) exhibits a steeper decline, implying $A\beta_{42}$ forms a less thermally stable complex with CR than $A\beta_{40}$. The shifted curve of $A\beta_{40/42}$ + AngII (orange line, open circle and purple line, open circle, respectively) compared to $A\beta_{40/42}$ alone, suggests AngII influences the binding dynamics or aggregate formation, potentially altering thermal dependence. CR-only normalized absorbance ratio at 540 nm (CR-amyloid binding) and 400 nm (CR-free) used to obtain the T_m values in Table 5 for the Aβ amyloid CR binding in the presence and absence of AngII peptide, the plot is the average of two independent experiments (n = 2; error bars represent S.E.M.).

Table 5. Transition temperatures (in Celsius) for Congo Red binding determined from sigmoidal curve fitting of the absorbance ratio at 540/400 nm in thermal ramps in Figure 21B and Figure 23.

CR	CR+AngII	CR+Ab_{40}	CR+Ab_{40}:AngII (1:5)	CR+Ab_{42}	CR+Ab_{42}:AngII (1:5)
69.93±0.02	65.24±0.03	60.50±0.02	65.96±0.06	52.65±0.04	56.37±0.06

AngII reduces Aβ-induced membrane disruption

Given the role of membrane interactions in Aβ toxicity[245–247], we assessed peptide-induced leakage in model liposomes. We have used model membranes such as POPC, POPC:PG (7:3), and POPC:PG:Chol (6:3:1) to aged peptide samples (Figure 24 and Figure 25), to measure the peptide-induced leakage of the fluorescent dye HPTS entrapped into liposomes by monitoring the HPTS fluorescence quenching by DPX quencher outside the liposomes. To avoid artifacts of excessive peptide concentration, all experiments were performed at a peptide:lipid ratio of 1:20. Encapsulated HPTS, shows a slight fluorescence drift in the absence of peptide (more evident for POPC and POPC:PG, than for POPC:PG:Chol liposomes, Figure 24), which reaches a 15-20% leakage when $Aβ_{40}$ or $Aβ_{42}$ peptides incubated for 30 h are present. Leakage is diminished when Aβ:AngII mixtures incubated for 30 h (1:2 ratio, Figure 25 and Figure 26) are added to the liposomes, especially in that with cholesterol. In brief, aged $Aβ_{40}$ and $Aβ_{42}$ induced 15–20% leakage, which was reduced 2-10% in $Aβ_{40}$ (Figure 24) and back to basal levels in $Aβ_{42}$ (Figure 25) in the presence of AngII (1:2 ratio), particularly in cholesterol-containing membranes (Figure 25C and Figure 26). This suggests that AngII may mitigate Aβ-induced membrane perturbation, possibly by altering peptide conformation or aggregation state[248–250].

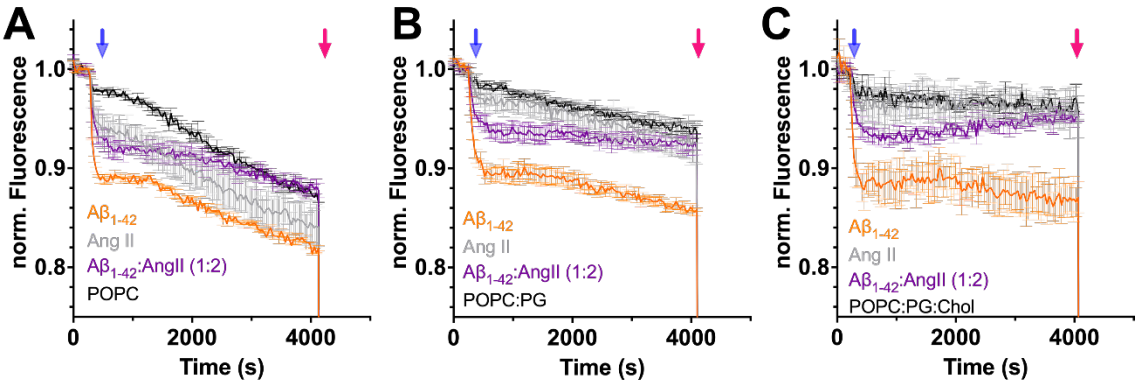


Figure 25. Liposome leakage experiments. HPTS fluorescence DPX-induced quenching in the presence of aged AngII, Ab_{42}, and Ab_{42}:AngII (1:2) mixture. Samples were incubated for 30 h at 37ºC before addition to 100 µM liposomes; **A.** POPC(100); **B.** POPC:PG (70:30); **C.** POPC:PG:Chol (60:30:10). Blue and pink arrows indicate the addition of peptide (or buffer in the liposome only condition in black) and Triton-X, respectively; plots correspond to the average of three independent measurements (n = 3); error bars represent S.E.M.

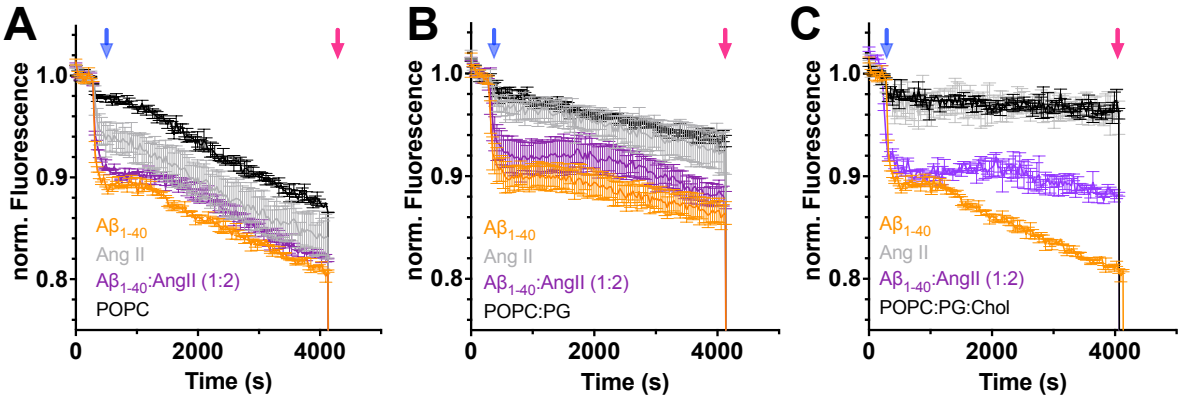


Figure 26. HPTS fluorescence DPX-induced quenching in the presence of aged peptide mixtures. HPTS fluorescence DPX-induced quenching in the presence of aged AngII, $Aβ_{40}$, and $Aβ_{40}$:AngII (1:2) mixture. Samples were incubated for 30 h at 37ºC before addition to 100 µM liposomes (A: POPC(100); B: POPC:PG (70:30); C: POPC:PG:Chol (60:30:10). Blue and pink arrows indicate the addition of peptide (or buffer in the liposome only condition in black) and Triton-X, respectively.

In silico modeling of Aβ–AngII interactions

Structural snapshots for $A\beta_{40}$ and $A\beta_{42}$, namely monomeric and low molecular weight fibril state are available [236–241], providing opportunities for in silico structural characterization. We evaluated the binding energy landscape of Aβ self-association across three conformational states: random coil, α-helix, and low molecular weight β-sheet fibrils (9 and 10 β-strands for $A\beta_{40}$ and $A\beta_{42}$, respectively). As expected, self-interaction energies become more favorable with increasing β-sheet content (Figure 27A and Figure 28), consistent with the thermodynamic drive toward fibril formation. The energy range goes from ca. -25 Rosetta energy units (REU) to ca. -2,100 REU, as a simplistic model of the interaction patterns occurring in an amyloid oligomerization/fibrillization pathway (Figure 27A and Figure 28). As a rule of thumb, the higher the β-sheet content of the counterplayers, the more negative the binding energy. To assess peptide-peptide cross interactions, we show the binding energy of Aβ, AngII, and the human serum albumin C-terminus fragment (CtHSA), as a previously described anti-amyloid peptide[251], with low energy of binding for comparison. Regardless of the Aβ secondary structure used as probe, the overall poses for Aβ-AngII cross interaction show higher mean energy compared to CtHSA- Aβ cross interaction, but in the similar range to Aβ-Aβ self-aggregation when the Aβ peptide is unordered. This Aβ-AngII cross interaction energy becomes less favorable as the Aβ secondary structure transits to a-helix and β-sheet. The most favorable docking pose for each Aβ secondary structure are represented in Figure 27B for $A\beta_{42}$ (Figure 28 for $A\beta_{40}$).

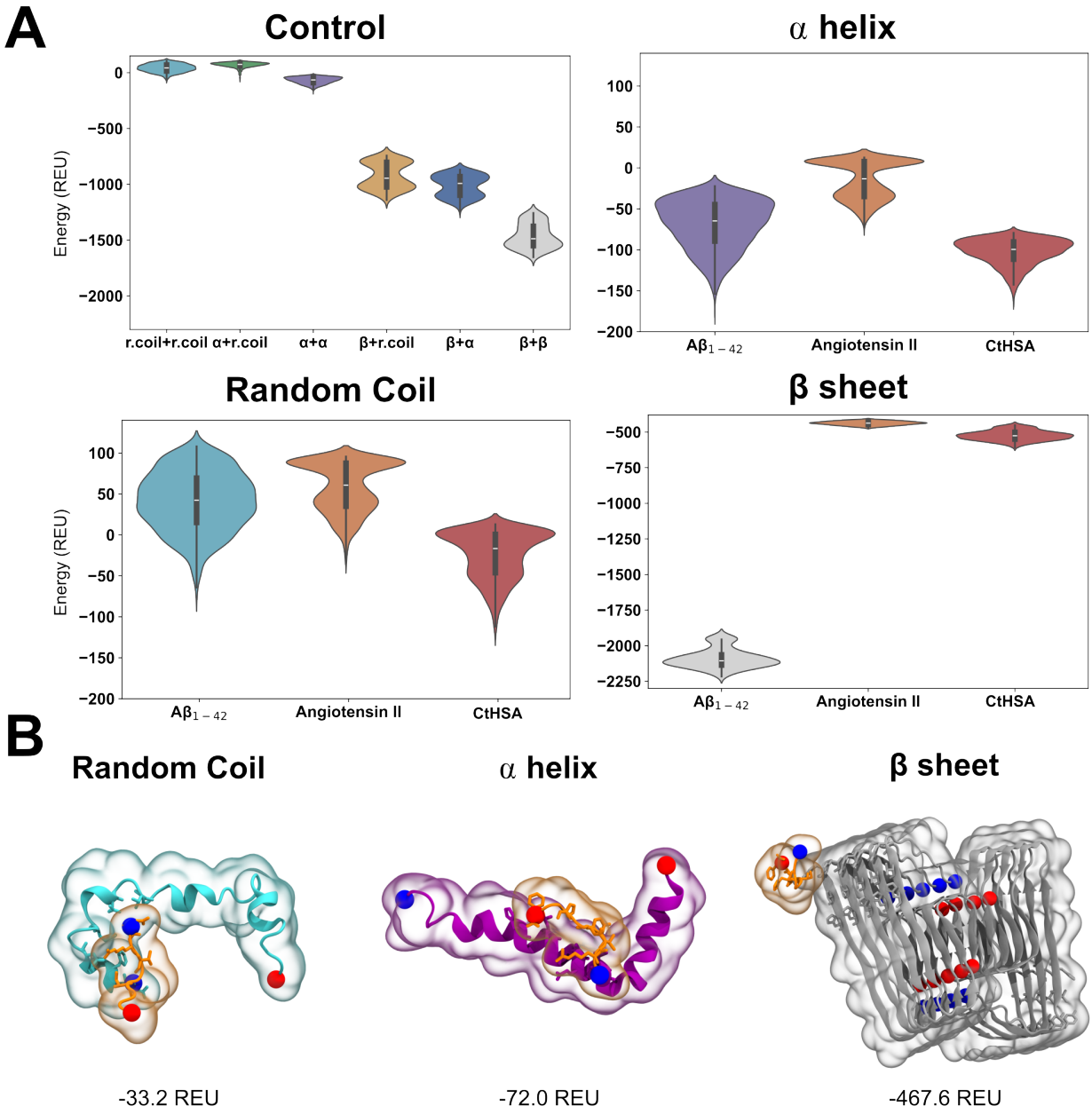


Figure 27. Rosetta docking analysis of $A\beta_{42}$ peptide interactions with angiotensin II and CtHSA under varying secondary structural conformations. **A.** Violin plots representing the binding energies (in REU: Rosetta Energy Units) $A\beta_{42}$ (right) interacting with Angiotensin II and C-terminal Human Serum Albumin (CtHSA) peptides. The energy values refer to 2000 molecular dockings, including 1000 performed with high-resolution and 1000 with low-resolution protocols. Horizontal dispersion within each violin reflects the exploration distance, i.e., the extent to which the docking program sampled alternative poses my moving the molecules during the search. Different secondary structures have been employed and $A\beta_{42}$: random coil (PDB id. 6SZF, respectively), α-helix (PDB id. 1Z0Q, respectively), and β-sheet (PDB id. 5OQV, respectively). Control plots show the energy distributions for each structure docked to itself and the others. **B.** Representative model $A\beta_{42}$ interacting with angiotensin II (in

orange) in the three different secondary structures (random coil in cyan, α-helix in purple, β-sheet in silver). The blue and red spheres indicate the N- and C-termini, respectively. Corresponding energy values are shown.

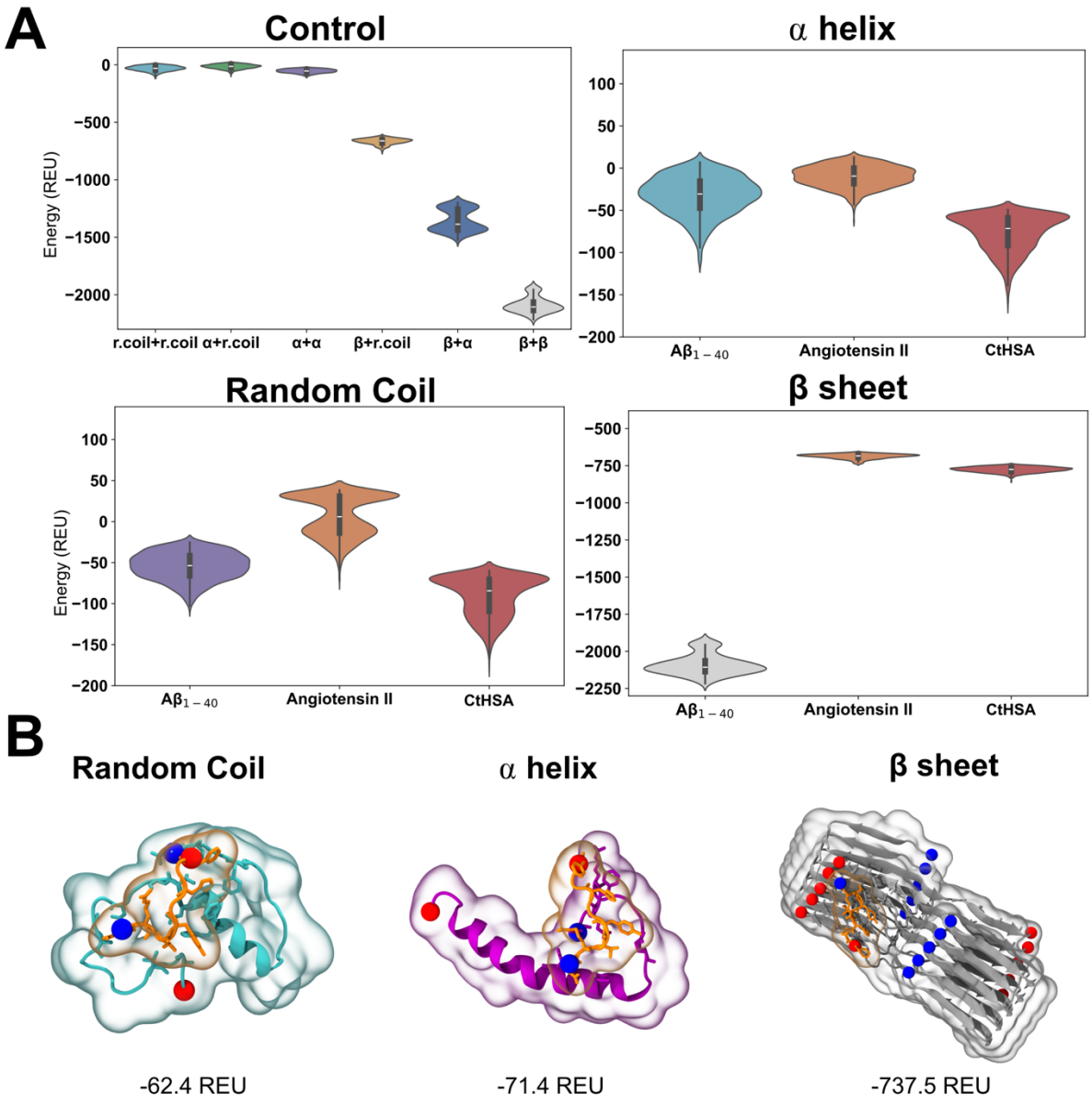


Figure 28. Rosetta docking analysis of $A\beta_{40}$ peptide interactions with angiotensin II and CtHSA under varying secondary structural conformations. **A.** Violin plots representing the binding energies (in REU: Rosetta Energy Units) for $A\beta_{40}$ interacting with Angiotensin II and C-terminal Human Serum Albumin (CtHSA) peptides. The energy values refer to 2000 molecular dockings, including 1000 performed with high-resolution and 1000 with low-resolution protocols. Horizontal dispersion within each violin reflects the exploration distance, i.e., the extent to which the docking program sampled alternative poses my moving the

molecules during the search. Different secondary structures have been employed for $A\beta_{40}$: random coil (PDB id. 1BA4), α-helix (PDB id. 2LFM), and β-sheet (PDB id. 8FF2). Control plots show the energy distributions for each structure docked to itself and the others. **B.** Representative model of $A\beta_{40}$ interacting with angiotensin II (in orange) in the three different secondary structures (random coil in cyan, α-helix in purple, β-sheet in silver). The blue and red spheres indicate the N- and C-termini, respectively. Corresponding energy values are shown.

To assess cross-interactions, we compared Aβ–AngII binding energies to those of Aβ–CtHSA. AngII exhibited higher binding energy than CtHSA when Aβ was in a disordered or α-helical state, but this interaction weakened as Aβ adopted β-sheet conformations (Figure 21A). This suggests that AngII preferentially interacts with early, unordered Aβ species, potentially modulating the initial stages of aggregation. Compared to other peptides previously studied (e.g., dynorphins and neurokinins)[97,98], AngII showed a narrower interaction window, with limited affinity for structured Aβ conformers.

AngII mostly interacts with the N-terminal region of Aβ peptides, where the binding is stabilized through a combination of hydrogen bonds and π-π stacking interactions. These non-covalent forces contribute to a relative stable complex in the unstructured or α-helical state of Aβ (Figure 21B). However, when AngII interacts with preformed Aβ fibrils, the area of interaction changes (close to the C-terminal in $A\beta_{40}$ or hydrophobic part in $A\beta_{42}$) and the number of residues involved is reduced, indicating a less favorable binding interface. In short, AngII can form relatively stable interactions with Aβ monomers, but Aβ oligomerization limits AngII ability to establish stabilizing contacts.

Implications for amyloid proteostasis

Although speculative, our findings are consistent with previous observations in Parkinson's disease (PD) models, where angiotensin II (AngII) reduced α-synuclein toxicity and aggregation[252]. However, unlike α-synuclein, where AngII effects were enhanced by AT1/AT2 receptor blockade, the Aβ–AngII interaction appears to be more direct and conformation-dependent. In our in silico and in vitro models, AngII preferentially interacted with early, unordered Aβ species, modestly reducing aggregation and membrane disruption. Particularly for the role of AngII-RAS system in AD, it has been claimed that hypertension and stress may lead to lower Aβ metabolism[227] and higher Aβ production[228], respectively. On the therapeutic side, the use of AngII blockers has been argued to be superior than the use of ACE inhibitors[229]. In a wider sense, the biological plausibility of neuropeptide–Aβ interactions is supported by the co-expression of neuropeptides such as AngII, dynorphins, neurokinins, substance P, etc. in brain regions central to AD[64,253–255], including the hippocampus and cortex, and particularly for AngII, brain microvessels[229], reinforcing the relevance of neuropeptide homeostasis in early amyloidogenic processes. These results support the broader concept that endogenous peptide–peptide cross-interactions may modulate amyloidogenic pathways and influence the early stages of aggregation.

From a mechanistic perspective, this interplay may reflect a convergence of enzymatic and signaling pathways relevant to both AD and PD. ACE is involved in the conversion of $A\beta_{42}$ to the less aggregation-prone $A\beta_{40}$, while also generating AngII from angiotensin I[255]. Neprilysin, another key protease, degrades both Aβ and dynorphins, highlighting shared proteostatic mechanisms across neurodegenerative diseases[256]. Moreover, dysregulation of the renin–angiotensin system (RAS)—particularly overactivation of the AT1 receptor—has been linked to

increased oxidative stress, neuroinflammation, and tau phosphorylation, all of which exacerbate Aβ pathology[257,258]. Elevated AngII and AngIII levels, along with reduced ACE2 and Mas receptor signaling, further shift the balance toward pro-amyloidogenic and pro-inflammatory states in AD brains[259,260]. Together, these findings underscore the potential relevance of both direct peptide interactions and broader RAS dysregulation in shaping amyloid homeostasis and neurodegenerative trajectories.

Discussion

Our findings indicate that AngII, an endogenous peptide of the renin–angiotensin system, interacts with amyloid-β (Aβ) in a conformation-dependent manner, with preferential binding to early, unordered Aβ species. This interaction modestly attenuates Aβ aggregation kinetics and reduces membrane-disruptive potential in vitro, particularly at higher AngII concentrations. These effects are consistent with a broader role for endogenous peptide–peptide cross-interactions in modulating amyloidogenic pathways. While moderate in magnitude, the observed effects support the notion that such interactions may contribute to protein homeostasis (proteostasis) by influencing the early stages of Aβ aggregation. Further investigation is warranted to elucidate the mechanistic basis and physiological relevance of these interactions in vivo.

CHAPTER III

*This chapter is based on the following published article Habibnia, M., Catalina-Hernandez, E., Barnadas-Rodríguez, R. & Peralvarez-Marin, A. Electrostatic control of membrane disruption and amorphous coaggregation by dynorphin A variants. Biochem. Biophys. Res. Commun. **827**, 154059 (2026). https://doi.org/10.1016/j.bbrc.2026.154059[261]. The content contains minor revisions for consistency with the overall thesis narrative.

Electrostatic control of membrane disruption and amorphous coaggregation by dynorphin A variants[261]

Introduction

Dynorphins are among the most positively charged peptides in the human body[262] and constitute a major family of endogenous opioid peptides. They are derived from the prodynorphin (PDYN) precursor[263], which undergoes proteolytic processing at basic residues to generate Big Dynorphin (BigDyn, 32 residues) and, subsequently, Dynorphin A (DynA, residues 1–17) and Dynorphin B (DynB, residues 20–32) following cleavage at the K–R hinge region[264,265]. Dynorphins act primarily as agonists of κ-opioid receptors (KOR) and, to a lesser extent, μ-opioid receptors (MOR), contributing to analgesia, stress responses, and addiction-related behaviors[266].

In addition to their canonical receptor-mediated activity, DynA displays a second, non-classical mode of action involving direct interactions with lipid membranes. Multiple studies have shown that DynA can disrupt membrane integrity independently of opioid receptor activation[267–271]. These membrane-active properties have been implicated in neurological disorders, including Spinocerebellar Ataxia Type 23 (SCA23)[272,273]. Mutations in the PDYN gene associated with SCA23 specifically alter the DynA sequence[269,274,275], giving rise to four clinically relevant variants: wild-type DynA (WT), a leucine-to-serine substitution at position 5 (L5S), an arginine-to-tryptophan substitution at position 6 (R6W), and an arginine-to-cysteine substitution at position 9 (R9C).

Previous work has demonstrated that DynA behaves as a cell-penetrating peptide (CPP), capable of translocating across plasma membranes in a lipid composition–dependent manner[268,270]. In anionic membranes, DynA and BigDyn induce calcium leakage and membrane permeabilization, whereas in neutral membranes DynA can form ion channel–like pores or undergo direct translocation[269,271,276]. Clinical variants display differential behavior: R6W and R9C show

increased membrane insertion, pore stability, resistance to proteolytic degradation, and neurotoxicity compared to WT[274,275,277]. In contrast, the L5S variant exhibits enhanced degradation and reduced membrane-disruptive activity experimentally, despite computational predictions suggesting strong CPP-like behavior[275,277,278].

This discrepancy between computational and experimental observations highlights the challenges of correlating peptide–membrane interactions across timescales, concentrations, and model systems. To address this gap, we combine Computational Electrophysiology (CompEL), which enables the study of larger peptide–lipid ratios and membrane perturbation under transmembrane potential, with in vitro liposome leakage and aggregation assays. Using this integrated approach, we investigate how membrane composition and sequence variation modulate DynA WT and variant behavior, aiming to establish generalizable principles of peptide–membrane interaction and aggregation.

Table 6. Sequence and physico-chemical properties of the peptides used in this research.

Peptide	Primary sequence	MW	Charge	GRAVY Index
$A\beta_{1-42}$	DAEFRHDSGYEVHHQKLVFFAEDVGSNKGAIIGLMVGGVVIA	4,514.1	-3	0.20
DynA WT	YGGFLRRIRPKLKWDNQ	2147.51	+4	-1.2
DynA L5S	YGGF**S**RRIRPKLKWDNQ	2121.43	+4	-1.5
DynA R6W	YGGFL**W**RIRPKLKWDNQ	2177.54	+3	-1.05
DynA R9C	YGGFL**C**RIRPKLKWDNQ	2094.46	+3	-0.85

Material and methods

Computational electrophysiology

Computational electrophysiology has been used for the computational study of DynA WT and its clinical variants membrane disruption. In CompEL, a double membrane configuration is needed due to periodic boundary conditions (PBC) applied. The initial system was generated in CHARMM-GUI[279–281], which was duplicated, rotated one of the systems, and both membranes were concatenated in the same file to achieve a double membrane configuration. The transmembrane potential through ion imbalance (ΔQ) was generated with gmx insert-molecules, inserting eight positive charges (K+) in the inner water compartment, and eight negative charges (Cl-) in the outer water compartment, reaching a ΔQ 16 membrane potential, as was concluded in a previous

study[278]. Then, the remaining ions were added in the corresponding water compartment to reach a 150 mM KCl concentration. Systems were solvated with TIP3P water molecules.

The same peptide structure was used as in our previous article, which were predicted using AlphaFold algorithm[278], relaxed during 100 ns in a molecular dynamics simulation, and clustered to obtain the most stable structure. For each system, eight –identic– peptides were introduced in the inner water compartment, reaching a 1:32 protein:lipd ratio (8 peptides :256 lipid residues).

Double membrane and peptide containing systems were minimized for 5 000 steps, equilibrated for approximately 2 ns, divided in six steps of 125, 125, 125, 500, 500, and 500 ps, while progressively lowering the restraints in lipid and protein residues (1 000, 400, 400, 200, 40, 0 $kJ \cdot mol^{-1} \cdot nm^{-2}$, respectively). Subsequently, CompEL molecular dynamics simulations were run for 500 ns and 3 replicas per system, accounting for a total simulation time of circa 20 μs. The corresponding ion concentration was kept constant using the computational electrophysiology method in GROMACS, which was implemented by Kutzner and collaborators[282] (production input files can be found at the GitHub repository). Simulations were run using GROMACS 2020 package [283–290], and CHARMM36m force field, in an RTX3080Ti GPU workstation, at approximately 80 ns/day.

Three different membrane compositions (table 7) were prepared with different combinations of 1-palmitoyl-2-oleoylphosphatidylcholine (POPC), 1-palmitoyl-2-oleoylphosphatidylserine (POPS), and cholesterol (CHOL), with a total number of 128 lipids per leaflet, 256 per bilayer and a total of 512 lipids per system. This way, three systems were prepared: POPC, POPC:POPG (ratio 7:3), and POPC:POPG:CHOL (6:3:1).

Table 7. Membrane compositions.

Membrane	**Ratio**	**Lipid number per leaflet**	**Lipid number per bilayer**
POPC	1	128	256
POPC:POPG	7:3	90:38	180:76

POPC:POPG:CHOL	6:3:1	77:38:13	154:76:26

Simulations were analyzed using Jupyter Notebook integrated development environment (IDE)[291] in combination with GROMACS analysis tools. Matplotlib[292] was used for graphic plotting, and VMD[293] was utilized for visual inspection and molecular graphics.

Peptides and sample preparation

The peptide concentration was determined by weight or spectrophotometrically by absorbance at 280 nm. DynA variants were dissolved in 10 mM NaPi buffer, pH 7.4, at a stock concentration of 250 µM. Liposome leakage experiements were performed at 5 µM and 10 µM peptide concentration for P:L 1:20 and 1:10, respectively.

Liposome leakage

1-Palmitoyl-2-oleoyl-sn-glycero-3-phosphocholine (POPC), 1-Palmitoyl-2-oleyol-sn-glycerol-3-[phospho-rac-(1-glycerol)] (POPG), and cholesterol (Chol) were dissolved in a 2:1 v/v mixture of $CHCl_3$ and MeOH to obtain the following mixtures and molar ratios: POPC, POPC:POPG (7:3), and POPC:POPG:Chol (6:3:1). Liposomes were prepared as described previously [101,294]. Concisely, a thin film was obtained by rotary evaporation of the previous lipidic organic solutions. Multilamellar liposomes with a total lipid concentration of 10 mM were obtained after hydrating the lipid film with phosphate buffer 10 mM pH 7.2 containing 2 mM 8-hydroxypyrene-1,3,6-trisulfonic acid (HPTS). Lastly, the liposomes were serially extruded multiple times through 400, 200, and 100 nm pore polycarbonate membranes. Liposome size distribution was characterized by dynamic light scattering (DLS, Nanotrac Wave, Microtrac, USA), yielding average radius sizes of 120 nm for POPC, 90 nm for POPC:PG, and 90 nm for POPC:PG:Chol, respectively. Removal of none-encapsulated HPTS was done by size-exclusion chromatography (SEC) in Sephadex G-25 PD-10 columns (Amersham Biosciences) and the final lipid concentration of the purified samples was adjusted to XXX xM. P-xylene-bis-pyridinium bromide (DPX, Fisher Scientific) at a final concentration of 5 mM was added to SEC-purified liposomes, resulting in a final concentration of 100 µM. HPTS-encapsulated liposomes with DPX were then loaded into a black 96-well plate with

a clear flat bottom. The HPTS fluorescence was measured over time and subsequently quenched by DPX upon liposome release of the dye using a FLUOstar Optima microplate reader (BMG LABTECH, Germany). The excitation and emission wavelengths were 420 nm and 520 nm, respectively. The effect of the peptides was evaluated by adding them to the wells at a final concentration of 5 µM and 10 µM. After 4,000 seconds, the full fluorescence quenching was assessed by solubilizing the liposomes with Triton X-100 (Sigma-Aldrich) at a final concentration of 5 mM. The leakage was monitored over 150 cycles as a decrease in relative fluorescent unit (RFU) with peptides added at the tenth cycle.

Aggregation and hydrophobic surface exposure kinetics

To characterize the kinetics of amyloid formation and hydrophobic surface exposure, fluorescence assays were conducted using Thioflavin T (ThT; Sigma Aldrich, Cat. N. T3516)[97] and Bis-ANS, respectively. $A\beta_{1\text{-}42}$ was prepared at a constant final concentration of 10 µM and co-incubated with DynA variants at molar ratios of 1:1 and 1:2, yielding final DynA concentrations of 10 µM and 20 µM, respectively. Ordered assembly was monitored using 40 µM ThT with excitation at 440 nm and emission at 520 nm. Hydrophobic surface exposure was tracked using 10 µM 4,4'-Dianilino-1,1'-binaphthyl-5,5'-disulfonic acid dipotassium salt (Bis-ANS; Tocris Bioscience Cat. No. 4434) with excitation at 380 nm and emission at 520 nm.

All measurements were performed at 37°C without shaking using a FLUOstar Optima microplate reader (BMG LABTECH, Germany). Data were normalized through a two-step protocol to facilitate the comparative analysis of kinetic parameters and amplitudes across different conditions. First, all raw fluorescence intensities were background-corrected and zero-leveled relative to a probe-only blank (F_{blank}), representing the intensity of ThT or Bis-ANS in buffer alone:

$$\mathrm{Fnorm2} = \frac{\mathrm{Fnorm1} - \mathrm{F0A\beta}}{\mathrm{FmaxA\beta} - \mathrm{F0A\beta}}$$

Samples containing DynA variants in the absence of were expressed as signal fold-change according to this initial normalization. To enable the analytical comparison of the aggregation amplitude (A) as a fold-change relative to the control, a second normalization step was applied to all samples containing $A\beta_{1\text{-}42}$:

$$\mathrm{Fnorm2} = \frac{\mathrm{Fnorm1} - \mathrm{F0A\beta}}{\mathrm{FmaxA\beta} - \mathrm{F0A\beta}}$$

In this step, and represent the initial and maximum fluorescence intensities of the control, respectively, scaling the signal from 0 to 1. The resulting kinetic traces were analyzed using nonlinear regression with a four-parameter sigmoidal Boltzmann equation:

$$\mathrm{F(t)} = \frac{\mathrm{A}}{1 + \exp[\mathrm{r_{max}} \times (\tau - \mathrm{t})]}$$

This model allowed for the determination of the plateau amplitude (A), the apparent maximum growth rate (r_{max}), and the aggregation half-time (τ). All reported values represent the mean and standard error (SEM) from at least three independent experiments.

Results

DynA clinical variants (P:L 1:32) have been simulated in POPC; POPC:PG (7:3), and POPC:PG:CHOL (6:3:1) symmetric bilayer compositions, in the presence of a transmembrane potential. After 500 ns (Figure 29A), peptides mostly partition in the bilayer, but there are discrete events (Figure 29B) of peptide insertion and peptide translocation. Thereafter, peptide-lipid interactions (Figure 29C) and conformational behavior and secondary structure conversions (Figure 29D) for all clinical variants in each specific lipid bilayer, were respectively assessed and characterized.

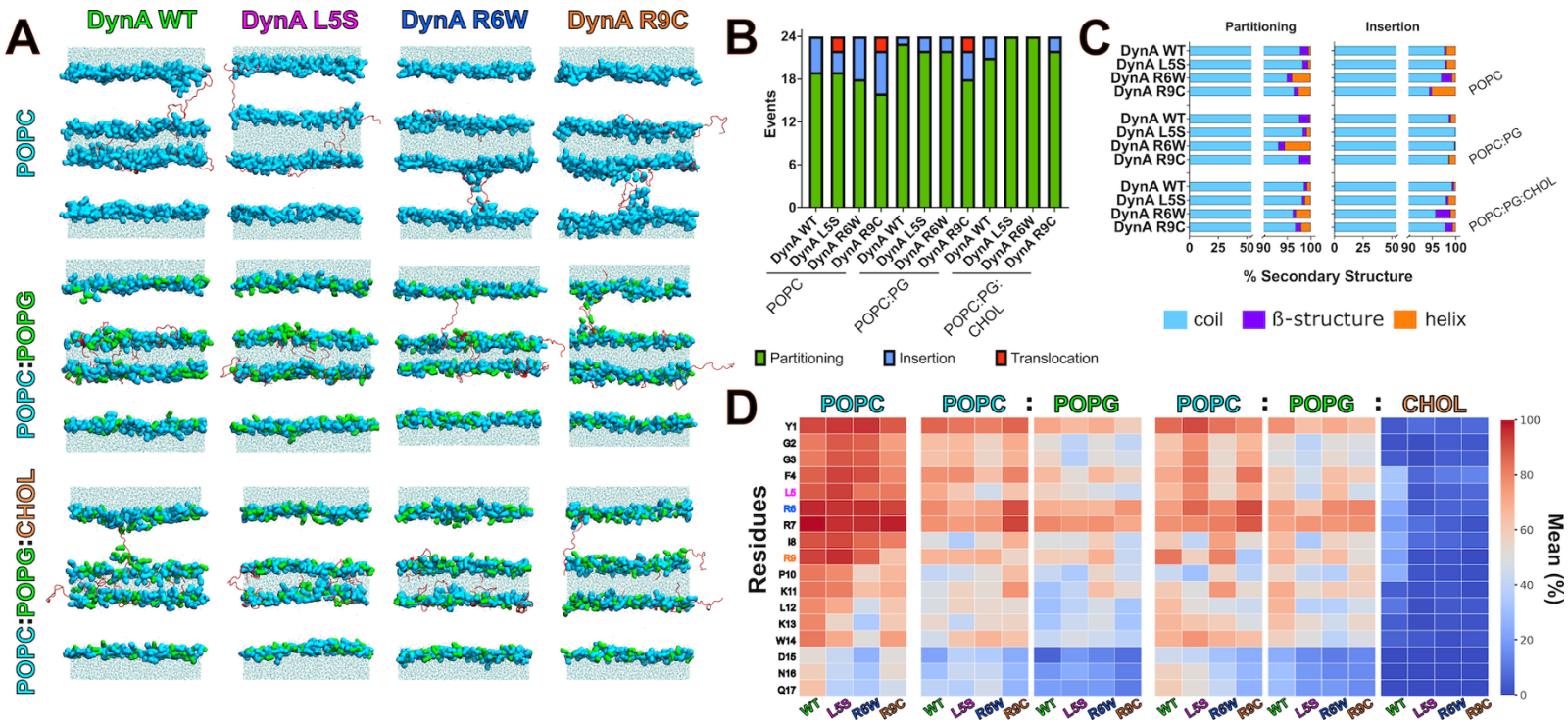


Figure 29. Membrane interaction behavior of DynA variants across lipid compositions. (A) Representative snapshots from molecular dynamics simulations. Peptides are shown in cartoon representation, and lipids are rendered as surfaces/lines colored by species. **(B)** Quantification of interaction events observed over simulation trajectories. **(C)** Heat map showing residue-level contact frequency (mean %) between DynA variants and lipid bilayers. Rows correspond to residues, and columns represent peptide variants in different lipid models. **(D)** Conformational behavior and secondary structure evolution of DynA variants during simulations. Time-resolved heat maps display changes in secondary structure elements across trajectories for each variant in different lipid environment.

Across all three membrane compositions (Figure 29A and B), interfacial partitioning dominates for all DynA variants. Insertion occurs with less frequency, but higher in POPC, lower in POPC:PG,

and hindered in POPC:PG:CHOL. R9C seems to show variant-specific enrichment for insertion in POPC:PG Translocation is rare, but happens for L5S in POPC and for R9C in POPC and POPC:PG, respectively. Regarding the peptide-lipid contacts, Figure 29C reveals a clear N-terminal contact signature. In POPC, DynA interacts strongly with the upper leaflet regardless of the variant, and the N-terminal contact signature spans residues 1-14, mediated by both hydrophobic and positively charged residues. In POPC:PG this N-terminal contact signature is restricted to the residues 1-7, and the positively charged residues become more relevant than hydrophobic ones, especially for R6W and R9C where the loss of the Arg is compensated by the neighboring positively charged residues (Figure 29C). In POPC:POPG:CHOL, contact frequencies are globally reduced (shift toward blue), indicating cholesterol dampens membrane association. Variants (L5S, R6W, R9C) show modestly altered contact profiles at the mutated positions relative to WT, but the N-terminal anchor is preserved across variants. Secondary structure plots show largely uniform coil/unstructured species across all conditions, confirming DynA remains predominantly unstructured throughout simulations. Sporadic streaks of transient helical or turn structures appear mainly in the N-terminal region and are most visible in POPC:POPG (e.g., L5S shows a notable hairpins structure during membrane insertion events) and POPC:POPG:CHOL conditions. These transient structured episodes correlate with membrane-inserted states and are absent or minimal in pure POPC, suggesting that anionic lipids (POPG) promote brief secondary structure formation upon deeper membrane engagement. Pore dimensions extracted from MD simulations (Table 8) reveal a strong membrane composition-dependent effect on DynA-induced bilayer disruption. In POPC, all variants produced comparably large pores (18-23 Å) well above the control (15 Å), consistent with the permissive nature of a pure PC bilayer. Introduction of POPG dramatically reduced baseline pore size (control: 0.2 Å), yet R6W and R9C selectively rescued pore formation (5.4 and 7.3 Å, respectively), while WT and L5S remained near control levels, mirroring the insertion events and transient secondary structure observed for these variants in POPC:POPG simulations (Figure 29D). In the cholesterol-containing membrane, the response diverged further, where WT and R9C sustained moderate pore sizes (in the 5 Å range), whereas R6W and L5S were strongly suppressed (<2 Å), indicating that cholesterol selectively neutralizes the pore-forming capacity of specific variants. Together, these data demonstrate that

DynA-mediated pore formation is governed by membrane association, but it is also peptide sequence dependent , that is differentially modulated by anionic lipids and cholesterol.

Table 8. Average pore radius (Å) in CompEL simulations.

Membrane	Control	DynA WT	DynA L5S	DynA R6W	DynA R9C
POPC	15.3 ± 3.2 [a]	20.5 ± 4.4	18.7 ± 4.2	20.6 ± 4.5	22.3 ± 5.1
POPC:POPG	0.2 ± 0.1[b]	1.7 ± 0.4	1.8 ± 0.4	5.4 ± 1.2	7.3 ± 1.8
POPC:POPG:CHOL	0.3 ± 0.1[b]	5.4 ± 1.6	1.9 ± 0.5	1.3 ± 0.3	5.1 ± 1.5

[a]Stable pore observed in 2 out of 3 replicas. No pore formation in the third replica.
[b] Transient pore formation (5-10 ns time range) observed in all replicas.

To validate the in silico membrane perturbation activity of DynA and its clinical variants variants, we performed fluorescence quenching-based leakage assays using LUVs. Normalized fluorescence was monitored over time, where a decrease in signal represents the leakage and subsequent quenching of the encapsulated HPTS by DPX upon peptide addition at approximately 5 minutes. In neutral POPC bilayers, all peptides behaved similarly at both 1:20 (Fig. 30A) and 1:10 (Fig. 30B) peptide-to-lipid (P:L) ratios, with a ca. <20% leakage. In these conditions, normalized fluorescence remained above 0.8 until the addition of Triton X-100 at 75 minutes, which induced total vesicle permeabilization. The introduction of POPG significantly sensitized the membranes to peptide-induced disruption (Fig 30C and 30D). At a 1:20 ratio (Fig. 30C), moderate leakage was initiated by all peptides (>20%). This effect was markedly amplified at a 1:10 ratio (Fig. 30D), where the R6W and R9C show more rapid and extensive leakage (>50%), with fluorescence dropping up to ~0.4 within 60 minutes (Table 9).

The inclusion of cholesterol in the membrane (POPC:PG:Chol) modulated the disruptive capacity of the peptides, highlighting differences between the WT, L5S (leakage <20%, Fig. 30E) and the R6W and R9C variants at 1:20 ratio (leakage >20%, Fig. 30E). At the 1:10 the differences between the WT and L5S subgroup are exacerbated in respect to the R6W and R9C subgroup (leakage >20%, Fig. 30E), where both the variants affecting positive residues show larger leakage effects up to ~0.45 (Fig. 30F), but with the extent of leakage slightly attenuated compared to the cholesterol-free system (Fig. 30D). A common activity hierarchy across all active conditions was consistently observed as DynA R6W > DynA R9C > DynA L5S ≈ DynA WT. L5S and WT displayed

soft leakage profiles in most panels, regardless of the lipid composition and the P:L ratio of choice (Table 9).

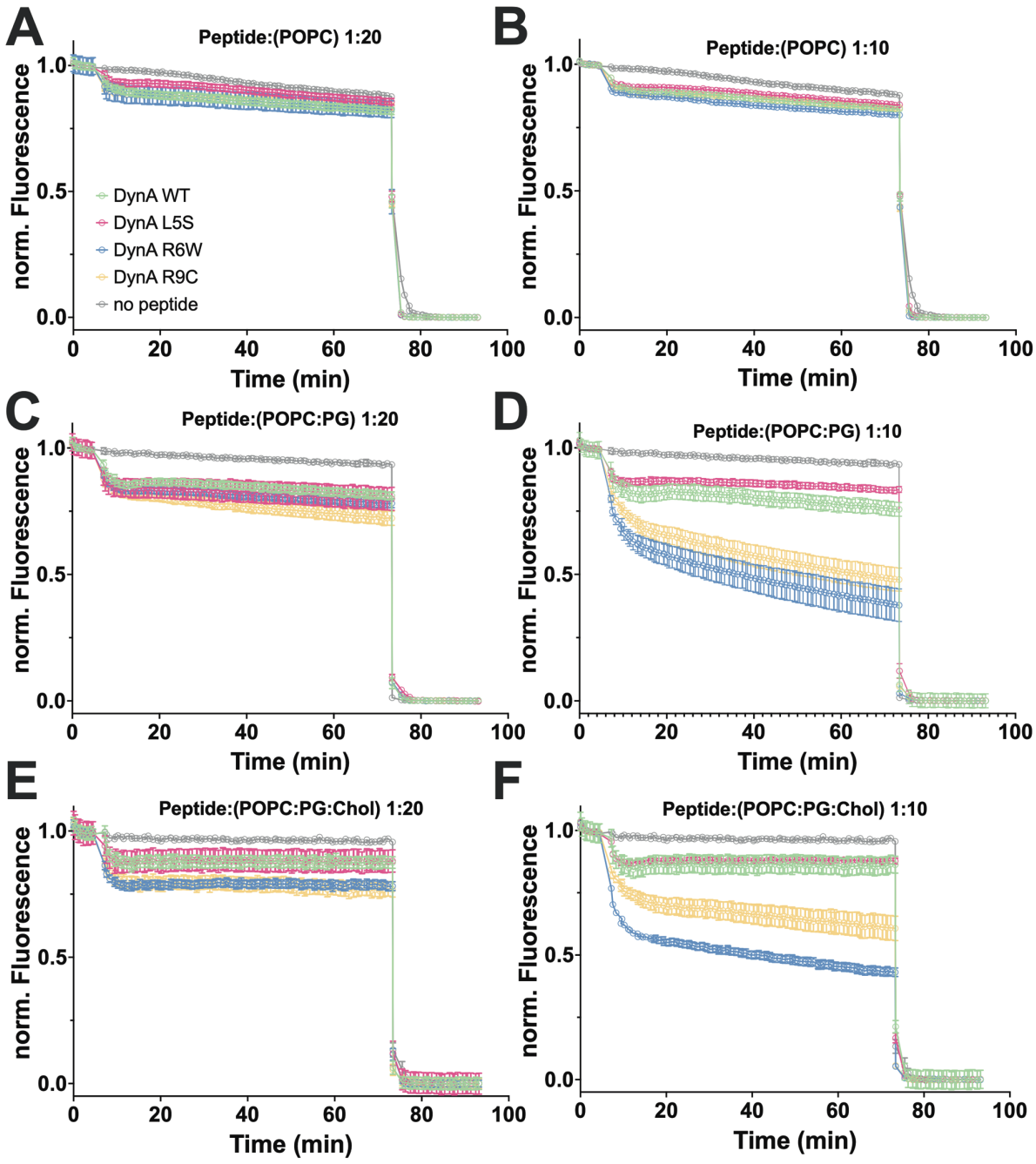


Figure 30. Liposome leakage assay monitoring membrane permeabilization by DynA variants. Normalized fluorescence intensity is shown over time for the liposome models incubated with DynA peptides at peptide:lipid molar ratios of 1:20 and 1:10. The vertical green drop at ~80 min in every panel represents the addition of detergent (Triton X-100) to fully disrupt all liposomes and establish the baseline fluorescence for normalization.

Table 9. Membrane Leakage (fraction of 1) at 60 minutes.

Composition	P:L	WT	L5S	R6W	R9C	no peptide
POPC	1:20	0.87 ± 0.02	0.89 ± 0.02	0.87 ± 0.06	0.88 ± 0.02	0.90 ± 0.13
POPC	1:10	0.86 ± 0.01	0.87 ± 0.01	0.84 ± 0.01	0.86 ± 0.02	0.90 ± 0.13
POPC:PG	1:20	0.87 ± 0.02	0.90 ± 0.05	0.84 ± 0.02	0.83 ± 0.01	0.95 ± 0.08
POPC:PG	1:10	0.80 ± 0.01	0.91 ± 0.01	0.43 ± 0.04	0.66 ± 0.02	0.95 ± 0.08
POPC:PG:Chol	1:20	0.90 ± 0.05	0.89 ± 0.09	0.80 ± 0.03	0.79 ± 0.06	0.96 ± 0.00
POPC:PG:Chol	1:10	0.86 ± 0.07	0.89 ± 0.02	0.47 ± 0.03	0.65 ± 0.09	0.96 ± 0.00

The membrane perturbartion exerted by DynA and the clinical variants, show that purely zwitterionic membranes (POPC) resist disruption, but the introdcution of electrostatic attraction (POPG) seems to be required as a primary anchor before hydrophobic deeper insertion can occur. The CompEL simulation and membrane leakage assays establish that DynA variants disrupt lipid bilayers assuming non-aggregated peptide conditions. Having defined this membrane-active regime, we next examined whether these variants exhibit aggregation-related behaviors in solution, either intrinsically or through interactions with aggregation-prone peptides, by analyzing ordered assembly and hydrophobic surface exposure using fluorescence-based aggregation assays.

Ordered assembly and hydrophobic surface exposure were monitored using Thioflavin T (ThT) and Bis-ANS fluorescence, respectively (Figure 31). Kinetic parameters were obtained by sigmoidal fitting, yielding the amplitude (A), apparent rate constant (r_{max}), and half-time (τ) for each condition (Table 10). DynA variants alone showed negligible ThT signal (Figure 31A), indicating the absence of spontaneous ordered aggregation. $A\beta_{1-42}$ alone displayed a sigmoidal aggregation profile (Figure 31B) with $A = 0.9 \pm 0.0$ and $\tau = 284.3 \pm 5.7$ min.

Addition of DynA WT at a 1:2 molar ratio reduced the final ThT plateau ($A = 0.7 \pm 0.0$) and shortened the half-time ($\tau = 166.6 \pm 4.0$ min), indicating modulation of fibril accumulation. The DynA L5S variant strongly altered $A\beta_{1-42}$ aggregation behavior (Figure 31C). At a 1:2 ratio, L5S increased the ThT amplitude to $A = 4.0 \pm 0.4$ and accelerated kinetics ($\tau = 10.0 \pm 14.8$ min). The R6W and R9C variants retained sigmoidal kinetics comparable to $A\beta_{1-42}$ alone (Figure 31D,E). R6W

(1:2) yielded A = 1.0 ± 0.0, while R9C (1:2) showed a moderate increase in amplitude (A = 1.3 ± 0.0) with τ = 232.7 ± 10.6 min.

Table 10. Kinetic parameters of ordered assembly and hydrophobic surface exposure in the presence of Dynorphin A variants.

	ThT			BisAns		
	A (fold)	r_{max} (min^{-1})	τ (min)	A (fold)	r_{max} (min^{-1})	τ (min)
$A\beta_{1-42}$	0.9±0.0	0.012±0.001	284.3±5.7	1.2±0.1	0.004±0.000	343.5±37.8
$A\beta_{1-42}$+DynA (1:1)	0.7±0.0	0.020±0.002	193.6±7.5	5.2±0.2	0.017±0.002	253.3±7.4
$A\beta_{1-42}$+DynA (1:2)	0.7±0.0	0.015±0.001	166.6±4.0	--	--	--
$A\beta_{1-42}$+DynA L5S (1:1)	1.8±0.0	0.006±0.000	389.6±10.6	18.0±0.7	0.026±0.003	145.7±5.0
$A\beta_{1-42}$+DynA L5S (1:2)	4.0±0.4	0.010±0.000	10.0±14.8	28.2±1.9	0.028±0.003	90.3±6.9
$A\beta_{1-42}$+DynA R6W (1:1)	0.7±0.0	0.024±0.002	218.0±4.4	8.5±0.4	0.006±0.000	304.9±16.4
$A\beta_{1-42}$+DynA R6W (1:2)	1.0±0.0	0.012±0.000	277.3±2.1	11.2±0.2	0.008±0.000	479.7±6.1
$A\beta_{1-42}$+DynA R9C (1:1)	1.6±0.0	0.005±0.000	428.0±9.3	2.0±0.0	0.007±0.000	519.2±9.6
$A\beta_{1-42}$+DynA R9C (1:2)	1.3±0.0	0.004±0.000	232.7±10.6	11.9±0.1	0.005±0.000	444.9±5.0

Bis-ANS assays revealed distinct hydrophobic co-aggregation behavior (Figure 31F–J). DynA WT alone showed a slightly decreasing signal. L5S and R6W alone exhibited rapid fluorescence decay. R9C alone displayed a sigmoidal increase, consistent with hydrophobic self-assembly. In the presence of $A\beta_{1-42}$, DynA WT produced low hydrophobic exposure (Figure 31G), with A = 5.2 ± 0.2 at a 1:1 ratio and insufficient signal for fitting at 1:2. Clinical variants induced pronounced hydrophobic species. L5S (1:2) reached a Bis-ANS amplitude of 28.2 ± 1.9, compared to 1.2 ± 0.1 for $A\beta_{1-42}$ alone, corresponding to a ~24-fold increase (Figure 31H). The half-time was τ = 90.3 ± 6.9 min, later than the ThT transition. R6W and R9C at 1:2 reached amplitudes of

11.2 ± 0.2 and 11.9 ± 0.1, with delayed half-times of 479.7 ± 6.1 min and 444.9 ± 5.0 min, respectively (Figure 31 I,J).

Across all conditions, ThT amplitudes remained within a narrow range (A ≈ 0.7–4.0), while Bis-ANS amplitudes varied widely for the mutant variants (A ≈ 11.2–28.2). This indicates dissociation between ordered fibril formation and hydrophobic surface exposure, consistent with the accumulation of non-fibrillar, hydrophobic co-aggregates.

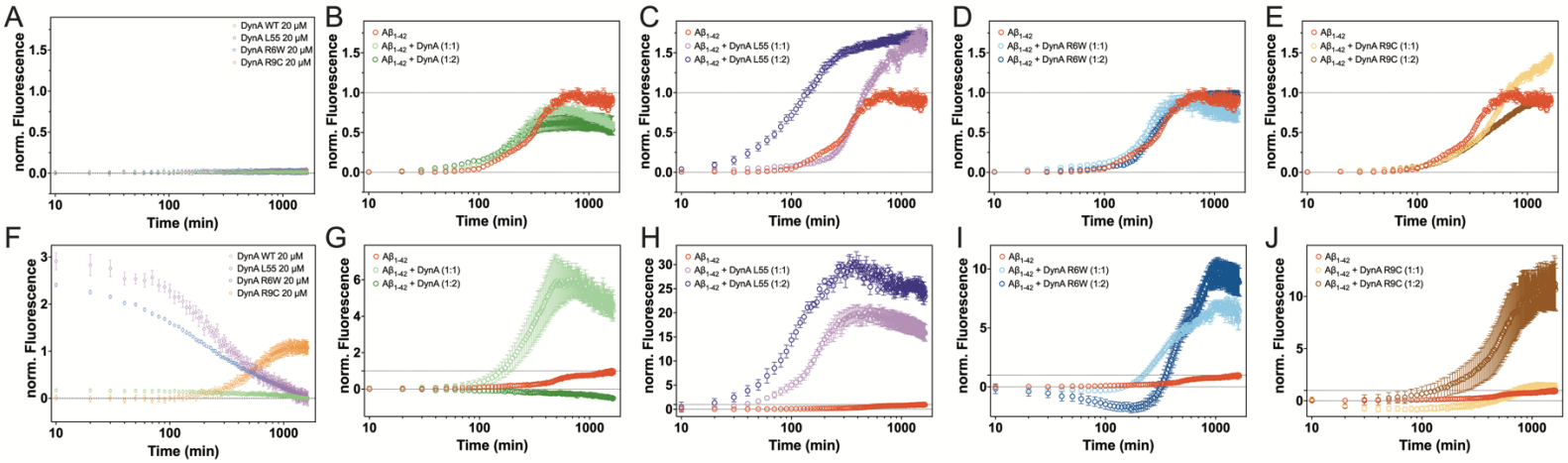


Figure 31. Kinetic modulation of aggregation and hydrophobic surface exposure by DynA variants. The aggregation of $A\beta_{1-42}$ (10 µM) was monitored in the presence of various DynA variants at molar ratios of 1:1 (10 µM) and 1:2 (20 µM) over 1,500 minutes. (A–E) Ordered assembly kinetics monitored by Thioflavin T (ThT) fluorescence. (A) Basal ThT fluorescence of DynA variants alone (20 µM). (B–E) Co-incubation of $A\beta_{1-42}$ (red circles) with DynA WT (B), L5S (C), R6W (D), and R9C (E). (F–J) Hydrophobic surface exposure monitored by Bis-ANS fluorescence. (F) Basal Bis-ANS fluorescence of DynA variants alone (20 µM). WT exhibits a slightly decreasing slope, L5S and R6W show exponential decay, and R9C displays independent sigmoidal growth. (G–J) Co-incubation of with DynA WT (G), L5S (H), R6W (I), and R9C (J). For kinetic parameters refer to Table 10**.** The dotted line in panels B-E and G-J shows the $A\beta_{1-42}$ normalized maximum fluorescence value as a reference (value of 1.0) for comparison. All reported values represent the mean and standard error (SEM) from at least three independent experiments.

Discussion

This study examines how sequence variations in Dynorphin A (DynA), including the wild-type peptide and the SCA23-associated variants L5S, R6W, and R9C, influence peptide structure, membrane interaction, and aggregation behavior under controlled biophysical conditions[272,274]. By combining CompEL simulations with membrane leakage and fluorescence-based aggregation

assays, we analyze general principles governing how short, highly cationic peptides interact with lipid bilayers and aggregation-prone partners such as amyloid-β (Aβ)[98,275]. While these variants are clinically observed in SCA23, the present work focuses on fundamental peptide–membrane and peptide–peptide interactions rather than the disease mechanisms.

DynA displays pronounced conformational plasticity, adopting an N-terminal α-helical structure upon membrane association, consistent with previous structural studies[275,276]. The L5S, R6W, and R9C substitutions reduce this membrane-induced helicity, demonstrating that single-residue changes can substantially disrupt local secondary structure in membrane-mimetic environments[101,275]. These findings underscore the sensitivity of amphipathic helices to sequence perturbations and highlight how residue chemistry modulates membrane-facing conformations.

At submicellar concentrations, DynA and its variants form aggregated species that retain predominantly α-helical character, in contrast to the β-sheet–rich assemblies typical of many amyloid-forming peptides[295]. Membrane leakage assays revealed a consistent hierarchy of bilayer perturbation (R6W > R9C > WT > L5S), reflecting the combined contributions of electrostatic membrane recruitment and mutation-dependent insertion depth[274]. CompEL simulations support an accumulation-dependent interaction mode in compositionally complex membranes, leading to transient proteolipidic defects rather than stable pore formation, in agreement with established models for amphipathic, cationic peptides[269,271,296].

The greatest divergence between simulation and experiment was observed for the L5S variant. Although computational models predicted strong membrane association, experimental leakage was minimal[101,274]. This highlights the importance of peptide stability and solution behavior, as L5S is more rapidly degraded than other variants, reducing its effective membrane engagement[275].

Co-aggregation experiments with Aβ1–42 further illustrate how DynA variants influence aggregation behavior. Thioflavin T assays showed limited effects on ordered fibril kinetics, consistent with previous observations[98]. In contrast, Bis-ANS measurements revealed substantial increases in hydrophobic surface exposure, particularly for L5S, indicating the formation of non-fibrillar, amorphous co-assemblies. This uncoupling of ordered assembly from hydrophobic

exposure reinforces the view that aggregation pathways can be redirected without enhancing fibrillization.

Overall, this work delineates how specific sequence features of DynA-derived peptides govern secondary structure stability, membrane interaction modes, and aggregation behavior. The results provide a biophysical framework for understanding how modest sequence perturbations modulate peptide association with lipid bilayers and influence aggregation pathways during co-assembly, offering general insights applicable to amphipathic, membrane-active peptides and aggregation-prone systems more broadly[98,275].

GENERAL DISCUSSION

1. General Discussion

The neurotoxicity of amyloid-β (Aβ) in Alzheimer's disease (AD) is initiated, and in large part perpetuated, at the neuronal membrane. Soluble Aβ oligomers insert into lipid bilayers, forming pores, thinning the membrane, and triggering calcium influx, oxidative stress, and synaptic dysfunction, the final common pathway of Aβ-induced neurodegeneration[175]. Yet this lethal sequence is not inevitable. Endogenous neuropeptides physically engage the hydrophobic domains of Aβ monomers and early oligomers, sterically hindering their insertion into membranes, stabilizing non-toxic conformations, and reducing pore formation[93]. In healthy brain, this natural proteostasis buffering system preserves membrane integrity[297]. In AD, however, the protective neuropeptide network collapses: levels of endogenous neuropeptides drop dramatically in the hippocampus, cortex, and other AD niches; the remaining peptides are sequestered into plaques or degraded faster[64], and their capacity to antagonize Aβ is progressively lost[298]. Without this molecular shield, Aβ oligomers converge on membranes, initiating the downstream cascade of tau hyperphosphorylation, neuritic degeneration, and clinical dementia[299].

The vulnerability of Aβ to self-assembly is encoded in its primary sequence. Three structural domains drive aggregation: APRs with high β-sheet propensity; CHC (residues 16–21: KLVFFA), the principal nucleation site; and the C-terminal amyloid core (residues 29–42), which stabilizes mature fibrils[300]. Endogenous neuropeptides preferentially dock onto these same hotspots, particularly the CHC and APR1; masking them and preventing the intermolecular contacts

required for nucleation and elongation. When neuropeptide levels fall, these hotspots are exposed, Aβ rapidly forms toxic oligomers, membrane disruption accelerates, and the amyloid cascade unfolds toward synaptic loss, neuronal death, and clinical AD[62].

This doctoral thesis interrogates this protective network from three complementary angles, each representing a distinct endogenous peptide system: Neurokinin A (NKA), Angiotensin II (AngII), and Dynorphin A (DynA) with its SCA23-linked clinical variants. Together, the three investigations build a mechanistic framework in which heterotypic neuropeptide-Aβ cross-interactions emerge as a previously underestimated checkpoint in amyloid proteostasis, one whose failure may represent among the earliest molecular events that converts physiological Aβ processing into pathological aggregation.

1.1. NKA–$A\beta_{42}$: Aromatic gating of the amyloid nucleation site

The first investigation established that NKA, a tachykinin neuropeptide co-expressed with Aβ in hippocampal and cortical circuits and implicated in the brain-gut axis, directly interacts with $A\beta_{42}$ through a combination of aromatic and hydrophobic contacts. Computational docking and molecular dynamics simulations converged on the CHC and APR1 regions of $A\beta_{42}$ as the primary NKA binding interface, consistent with the general principle that neuropeptides with amphipathic character preferentially engage Aβ's aggregation hotspots. The FXGLM motif of NKA, and specifically its phenylalanine residue; was identified as the central mediator of this interaction through π-π stacking and hydrogen bonding with Phe19 and Phe20 of $A\beta_{42}$, contacts that directly disrupt the face-to-face aromatic registry essential for Aβ dimerization and early oligomer nucleation.

The functional consequences of this interaction were characterized at multiple levels. ThT fluorescence kinetics demonstrated a dose-dependent attenuation of $A\beta_{42}$ fibrillation at a 2:1 NKA:Aβ stoichiometry, accompanied by a shift in secondary structure propensity from random coil toward more ordered, helical conformations as monitored by circular dichroism. This structural redirection is mechanistically significant: by stabilizing $A\beta_{42}$ in a helical rather than β-sheet-prone state, NKA effectively delays the conformational transition that underpins nucleation. The Phe-to-Trp substitution variant (NKAW) retained modulatory capacity, confirming that aromatic character at this position is both necessary and sufficient for the interaction, and illustrating how rational single-residue modifications can preserve or tune the neuropeptide's modulatory function. At the cellular level, NKA reduced $A\beta_{42}$-induced toxicity in SH-SY5Y neuronal cells in a dose-dependent fashion, extending the biophysical observations into a biologically relevant context and supporting a direct neuroprotective role that transcends mere kinetic interference with fibrillation.

Taken together, the NKA findings define a mechanism of aromatic gating: NKA's phenylalanine inserts into the π-stacking network of the CHC, preventing the face-to-face intermolecular contacts that seed oligomerization, stabilizing helical Aβ conformers, and reducing membrane-active species. This positions NKA, and by extension the tachykinin family; as endogenous aromatic gatekeepers of the amyloid nucleation site, a role whose disruption during AD-associated neuropeptide depletion would directly accelerate early aggregation events.

1.2. AngII–Aβ: Vascular-amyloid crosstalk and conformation-selective modulation

The second investigation expanded the heterotypic interaction framework to Angiotensin II, the principal effector of the renin-angiotensin system (RAS), whose dysregulation in hypertension and metabolic disease is increasingly recognized as a risk modifier in AD. AngII interacts with both $A\beta_{40}$ and $A\beta_{42}$, with Rosetta docking calculations revealing a strong preference for disordered or α-helical Aβ conformers over β-sheet-rich fibrillar states, a selectivity profile that mirrors, and reinforces, the conformation-dependent mechanism observed for NKA. By binding preferentially to early, structureless Aβ species, AngII intercepts the aggregation pathway at the pre-nucleation stage, reducing the pool of monomers available for β-sheet-competent assembly.

In vitro biophysical assays corroborated the computational predictions. ThT-monitored fibrillization kinetics showed reduced aggregation amplitude and altered lag-phase parameters in the presence of AngII, while Congo Red thermal ramp experiments demonstrated a 3–6°C elevation in the melting temperature of Aβ aggregates, indicating thermodynamic stabilization of non-amyloid states. Membrane leakage assays across liposomes of varying compositions (POPC, POPC:POPG, and POPC:POPG:Chol) revealed a 2–10% reduction in Aβ-induced permeabilization in cholesterol-containing vesicles, consistent with a mechanism in which AngII binding to Aβ monomers reduces the membrane-insertion-competent fraction rather than directly blocking membrane interaction. This modest but reproducible effect in the cholesterol-containing model is noteworthy given that neuronal membranes are cholesterol-enriched, suggesting that even partial masking of Aβ's hydrophobic surface by AngII may translate into biologically meaningful protection in vivo.

The AngII results introduce a vascular-amyloid dimension absent from the tachykinin framework. ACE, a key RAS enzyme, is also a major Aβ-degrading protease; AT1 receptor signaling promotes oxidative stress and neuroinflammation; and RAS dysregulation in hypertension amplifies Aβ production and impairs clearance. The heterotypic AngII–Aβ interaction thus operates within a broader regulatory network where cardiovascular and amyloid pathways converge, and where pharmacological RAS modulation (with AT1 blockers or ACE inhibitors) may partially recapitulate the protective effect of endogenous AngII binding to early Aβ species. This places the AngII–Aβ interaction at the intersection of vascular risk and amyloid proteostasis, and identifies RAS modulation as a tractable therapeutic node within the broader neuropeptide-buffering framework described in this thesis.

1.3. DynA and SCA23 clinical variants: Pathological co-aggregation and synergistic membrane disruption

The dynorphin family provides a natural entry point into the opioid neuropeptide axis of amyloid proteostasis. Big Dynorphin (BigDyn), the 32-residue prodynorphin-derived precursor that encompasses both DynA and DynB, was shown by 2D NMR HSQC to bind monomeric $A\beta_{40}$ in a concentration-dependent manner, inducing progressive resonance attenuation indicative of intermediate-timescale exchange or co-assembly into NMR-invisible species. BigDyn also attenuated $A\beta_{40}$-induced toxicity in SH-SY5Y neuronal cells[98], establishing a neuroprotective role analogous to those reported here for NKA and AngII. Crucially, however, neither DynA nor DynB individually showed detectable specific binding to monomeric $A\beta_{40}$ by NMR, nor did they exert a significant modulatory effect on $A\beta_{40}$ aggregation behavior. This length- and sequence-dependent dissociation within the dynorphin family (BigDyn protective, its shorter cleavage

products largely neutral toward $A\beta_{40}$) raises an immediate and important question: does the picture change when the Aβ isoform is $A\beta_{42}$, with its extended and more aggregation-prone C-terminus, and when the dynorphin variants carry the pathogenic substitutions linked to spinocerebellar ataxia type 23?

The preliminary data presented in this thesis precisely address this question, and the answer is both affirmative and mechanistically unexpected. Wild-type DynA, when co-incubated with $A\beta_{42}$, modestly attenuates the final fibril plateau and mildly accelerates the aggregation half-time, an effect too weak to be detected against $A\beta_{40}$ by NMR in the Gallego-Villarejo study[98], but discernible in the more sensitive ThT kinetic assay against the more aggregation-prone $A\beta_{42}$ isoform. This isoform-dependent difference is itself informative: the extended C-terminus of $A\beta_{42}$, which provides additional hydrophobic surface and lowers the nucleation barrier, may create a more accessible interaction interface for a peptide as amphipathic and cationic as DynA, even in the absence of the high-affinity contacts that BigDyn makes via its full 32-residue scaffold. The SCA23-linked clinical variants, however, deviate from this modest modulatory baseline in a profound and variant-specific manner. DynA L5S, the substitution of leucine for serine at position 5, which reduces hydrophobicity, induced a dramatically approximately fourfold amplification of ThT amplitude and a near-instantaneous nucleation event ($\tau \approx 10$ min at 1:2 molar ratio), indicating that this polarity shift paradoxically redirects $A\beta_{42}$ into rapid, mass-amplified assembly. The R6W and R9C variants displayed intermediate effects on ordered assembly, yet all three mutants generated disproportionately elevated Bis-ANS amplitudes (up to 24-fold above the $A\beta_{42}$-alone control for L5S), revealing that DynA clinical variants primarily steer $A\beta_{42}$ toward amorphous, hydrophobic co-aggregates rather than canonical amyloid fibrils. This uncoupling of

ThT and Bis-ANS signals marks a mechanistic shift of considerable significance: the clinical variants do not merely accelerate fibrillization, they redirect the aggregation pathway toward solvent-exposed co-assemblies whose membrane-disruptive and seeding potential may be substantially greater than that of ordered fibrils.

The membrane permeabilization data provide an independent and complementary line of evidence, extending the framework from aggregation to bilayer integrity. In neutral POPC bilayers, all DynA variants showed negligible leakage, confirming that hydrophobic contacts alone are insufficient to drive membrane disruption in the absence of electrostatic attraction, consistent with DynA's highly cationic character and its documented preference for negatively charged surfaces. Introduction of 30 mol% POPG dramatically sensitized liposomes to DynA-induced disruption, with R6W and R9C achieving near-complete permeabilization at 1:10 peptide-to-lipid ratios. The arginine-to-tryptophan substitution in R6W enhances hydrophobic partitioning through the indole ring's affinity for lipid acyl chains, while R9C reduces net cationic charge and introduces reactive thiol groups capable of forming intermolecular disulfide bridges that stabilize membrane-inserted oligomers. Cholesterol partially attenuated leakage relative to the cholesterol-free anionic system, yet R6W and R9C retained significant disruptive capacity even in this more rigid bilayer, a finding with direct relevance to the cholesterol-enriched environment of neuronal membranes. A consistent activity hierarchy across all membrane compositions: DynA R6W > R9C > L5S ≈ WT; identifies charge reduction and aromatic enhancement as the primary molecular determinants of pathological membrane activity.

Taken together, these preliminary findings construct a coherent and progressively more detailed picture of the dynorphin–Aβ interaction landscape. BigDyn, with its full complement of residues, achieves genuine high-affinity binding to monomeric $A\beta_{40}$ and confers neuroprotection. Wild-type DynA, despite lacking this binding capacity against $A\beta_{40}$ by NMR, exerts a detectable and modest modulatory effect against the more aggregation-prone $A\beta_{42}$, suggesting a length- and isoform-gated threshold for productive interaction. The SCA23 clinical variants then subvert even this limited protective capacity entirely, co-aggregating with $A\beta_{42}$ into amorphous, hydrophobic assemblies and synergistically amplifying membrane disruption. This positions the dynorphin system as a two-faced regulator whose protective potential is concentrated in its longest, intact form (BigDyn), progressively attenuated by proteolytic processing to DynA and DynB, and ultimately inverted into a gain-of-function neurotoxic mechanism by the point mutations responsible for SCA23, a model with significant implications for both the genetic intersection between SCA23 and AD-like pathology and for the design of prodynorphin-derived therapeutic scaffolds.

1.4. An integrated framework: Neuropeptide heterotypic interactions as gatekeepers of the amyloid cascade

A central and unifying theme across all three investigations is the conformation-dependent nature of neuropeptide-Aβ interactions. NKA engages $A\beta_{42}$ preferentially through aromatic contacts that stabilize helical conformers and prevent β-sheet nucleation; AngII binds with highest affinity to disordered and α-helical Aβ, intercepting the pre-nucleation pool; and wild-type DynA exerts its modest modulatory effect through a related preference for early, unstructured Aβ species. This convergence on early Aβ conformers suggests a shared mechanistic

logic: endogenous neuropeptides act as conformation-selective chaperones that intercept the amyloid pathway before oligomeric, membrane-active species accumulate. The critical transition they collectively prevent is the conformational switch from random coil or helix to β-sheet, the thermodynamic gateway to both fibril formation and membrane insertion.

The functional data further illuminate important parallels and distinctions between the three systems. NKA acts directly on both aggregation kinetics and cellular viability, combining biophysical interference with measurable neuroprotection. AngII operates with a stronger vascular-metabolic overlay, linking its modulatory capacity to RAS-mediated regulation of Aβ metabolism, oxidative stress, and blood-brain barrier integrity. The dynorphin system introduces a third logic: the protective capacity of the intact prodynorphin-derived scaffold (BigDyn) is progressively eroded by proteolytic processing to DynA and DynB, and ultimately inverted into neurotoxicity by the SCA23 clinical substitutions, demonstrating how both physiological protein maturation and genetic variation can traverse the spectrum from neuropeptide-as-protector to neuropeptide-as-pathogen within a single peptide family. Across all three systems, the interaction surface on Aβ converges on the CHC and adjacent hydrophobic regions, underscoring these hotspots as the molecular fulcrum around which both protective and pathological neuropeptide effects are organized.

This molecular picture maps coherently onto the amyloid cascade hypothesis. In healthy brain, the neuropeptide network (comprising tachykinins, RAS effectors, opioid peptides, and likely many other co-expressed endogenous peptides) maintains a dynamic equilibrium in which Aβ's aggregation hotspots are partially masked, its conformational landscape is biased toward helical

states, and its membrane-inserting capacity is constrained. In AD, multiple converging failures (transcriptional downregulation, plaque sequestration, accelerated proteolysis, and, in genetic cases, gain-of-function mutations) erode this buffering network, exposing Aβ hotspots and permitting the formation of the oligomeric, β-sheet-rich, membrane-active species that initiate the downstream cascade of tau pathology, synaptic loss, and neurodegeneration.

From a therapeutic standpoint, each of the three neuropeptide systems described here offers a distinct intervention window. The aromatic gating mechanism defined by NKA suggests that phenylalanine-containing peptide mimetics, rationally optimized through substitutions such as the Phe-to-Trp modification explored here, could be designed to competitively occupy Aβ's CHC, preventing nucleation with enhanced affinity or stability. The conformation-selective binding profile of AngII supports the use of RAS modulators to reinforce endogenous buffering of early Aβ states, particularly in patients where cardiovascular risk and amyloid burden co-exist. The dynorphin findings, while preliminary, point to BigDyn's full-length scaffold as a potential neuroprotective template, raise the prospect of designing proteolysis-resistant prodynorphin-derived peptides that preserve its Aβ-modulatory capacity, and highlight the need to account for the gain-of-function membrane toxicity of SCA23 variants in patients carrying PDYN mutations, a population in whom standard amyloid-targeting strategies may need to be complemented by approaches that address the dynorphin-mediated component of membrane disruption.

Limitations of the current work are acknowledged. All three studies rely primarily on in vitro biophysical and cell culture approaches, complemented by in silico modeling; the physiological relevance of the observed interactions at the peptide concentrations used remains to be

confirmed in vivo. The liposome models, while systematically varied in composition, cannot fully recapitulate the asymmetric, protein-rich, and highly organized environment of neuronal membranes. The DynA chapter presents preliminary data whose mechanistic interpretation, particularly the amorphous co-aggregation pathway; requires validation by structural approaches such as cryo-electron microscopy or solid-state NMR. Future work should address these limitations through animal models of AD and SCA23, patient-derived neuronal systems, and structural characterization of the heterotypic assemblies described here.

In essence, this doctoral thesis advances the view that Aβ aggregation in the AD brain is not an isolated, sequence-intrinsic process but the outcome of a dynamic proteostatic equilibrium shaped by the surrounding neuropeptide environment. NKA, AngII, and DynA, three structurally and functionally distinct peptide systems embedded in tachykinin, vascular, and opioid signaling networks respectively, each contribute to this equilibrium through conformation-selective, hotspot-directed heterotypic interactions that collectively buffer the amyloid pathway. Their failure, whether through depletion, sequestration, or pathological mutation, represents not merely an epiphenomenon of AD progression but potentially one of its earliest and most tractable molecular triggers.

CONCLUSIONS

Chapter I: Heterotypic interaction between Neurokinin A and amyloid-β42

1. NKA and $A\beta_{42}$ engage in a direct heterotypic cross-interaction driven by aromatic and hydrophobic contacts. Computational docking and molecular dynamics simulations identified the central hydrophobic core of $A\beta_{42}$ (CHC, residues 16–21: KLVFFA) as the primary binding interface, with the phenylalanine residue within NKA's FXGLM signature motif mediating π-π stacking and hydrogen bonding with Phe19 and Phe20 of $A\beta_{42}$.

2. NKA modulates $A\beta_{42}$ aggregation in a concentration-dependent manner, reducing the final fibril plateau and delaying fibrillization kinetics as monitored by ThT fluorescence assays. At a 2:1 NKA:Aβ stoichiometry, circular dichroism spectroscopy revealed a shift in $A\beta_{42}$ secondary structure from random coil toward more ordered helical conformations, indicating that NKA stabilizes early, non-fibrillogenic Aβ states and interferes with the conformational transition required for nucleation.

3. NKA disrupts the formation of intramolecular salt bridges between Asp23 and Lys28 in $A\beta_{42}$ and shields the aromatic and hydrophobic interactions among $A\beta_{42}$ monomers, thereby preventing early oligomerization steps and inhibiting the cross-β structure formation that underpins fibril growth.

4. The Phe-to-Trp substitution in NKA (NKAW) retains the capacity to modulate $A\beta_{42}$ aggregation, confirming that aromatic character at the phenylalanine position within the FXGLM motif is both necessary and sufficient for the interaction. This result demonstrates that rational single-residue modifications can preserve the neuropeptide's anti-

amyloidogenic function and provides a basis for structure-guided optimization of peptide-based modulators.

5. NKA significantly reduces $A\beta_{42}$-induced toxicity in SH-SY5Y neuroblastoma cells across the stoichiometries tested, demonstrating a neuroprotective effect that extends beyond biophysical interference with fibrillization and supports a direct role for NKA in limiting Aβ-mediated neuronal damage.

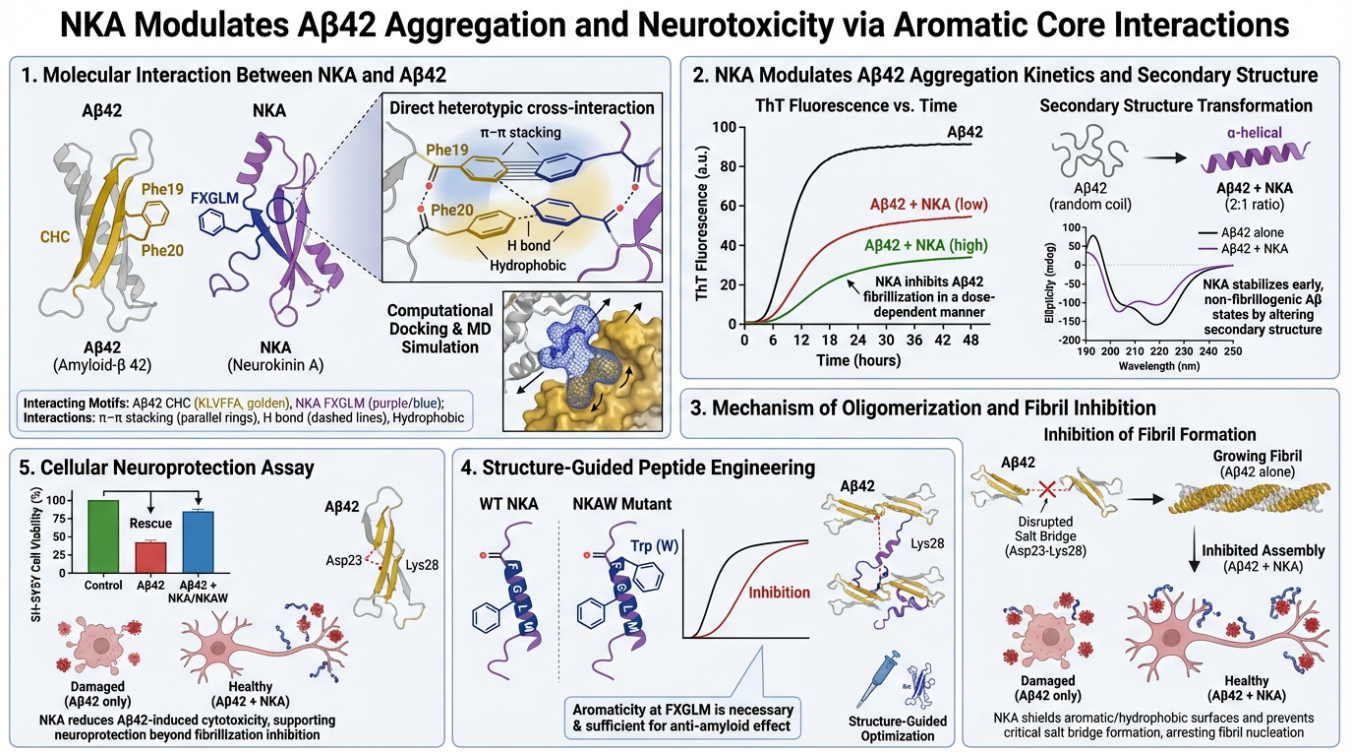


Figure 32. NKA modulates $A\beta_{42}$ aggregation and neurotoxicity. (Created by figurelabs.ai).

Chapter II: Heterotypic interaction between Angiotensin II and amyloid-β peptides

6. AngII interacts with both $A\beta_{40}$ and $A\beta_{42}$ in a conformation-selective manner, preferentially binding disordered and random coil Aβ conformers over α-helical or β-sheet-rich states. Rosetta docking calculations yielded more favorable binding energies for unordered Aβ

conformers (approximately −25 to −2100 REU), indicating that AngII intercepts the amyloid pathway at early, pre-nucleation stages by stabilizing less fibrillogenic Aβ forms.

7. AngII modestly attenuates Aβ aggregation in a dose-dependent manner, reducing the final ThT amplitude, increasing the aggregation half-time (τ), and decreasing the maximum growth rate (r_{max}), consistent with inhibition of fibril formation. Circular dichroism spectroscopy further showed that AngII concentration-dependently preserves random coil structures in $Aβ_{42}$, delaying the structural transition toward β-sheet dominance.

8. AngII increases the melting temperature of Aβ amyloid aggregates in Congo Red thermal ramp assays by 3–6°C, attenuating red-shift shoulders in absorbance spectra and delaying amyloid onset, indicating thermodynamic stabilization of non-amyloid Aβ states in the presence of AngII.

9. AngII mitigates Aβ-induced membrane disruption, reducing liposome leakage induced by aged $Aβ_{40}$ and $Aβ_{42}$ by 2–10% in cholesterol-containing membranes (POPC:POPG:Chol) and to basal levels for $Aβ_{42}$ at a 1:2 peptide ratio. This protective effect is most pronounced in cholesterol-enriched bilayers, consistent with a mechanism in which AngII binding to early Aβ species reduces the pool of membrane-insertion-competent oligomers.

10. Computational docking indicates that AngII interacts primarily with the N-terminal region of Aβ through hydrogen bonds and π-π stacking, with less favorable binding to fibrillar forms near the C-terminus of $Aβ_{40}$ or the hydrophobic regions of $Aβ_{42}$, underscoring

AngII's preferential activity at early aggregation stages and its limited efficacy against mature fibrils.

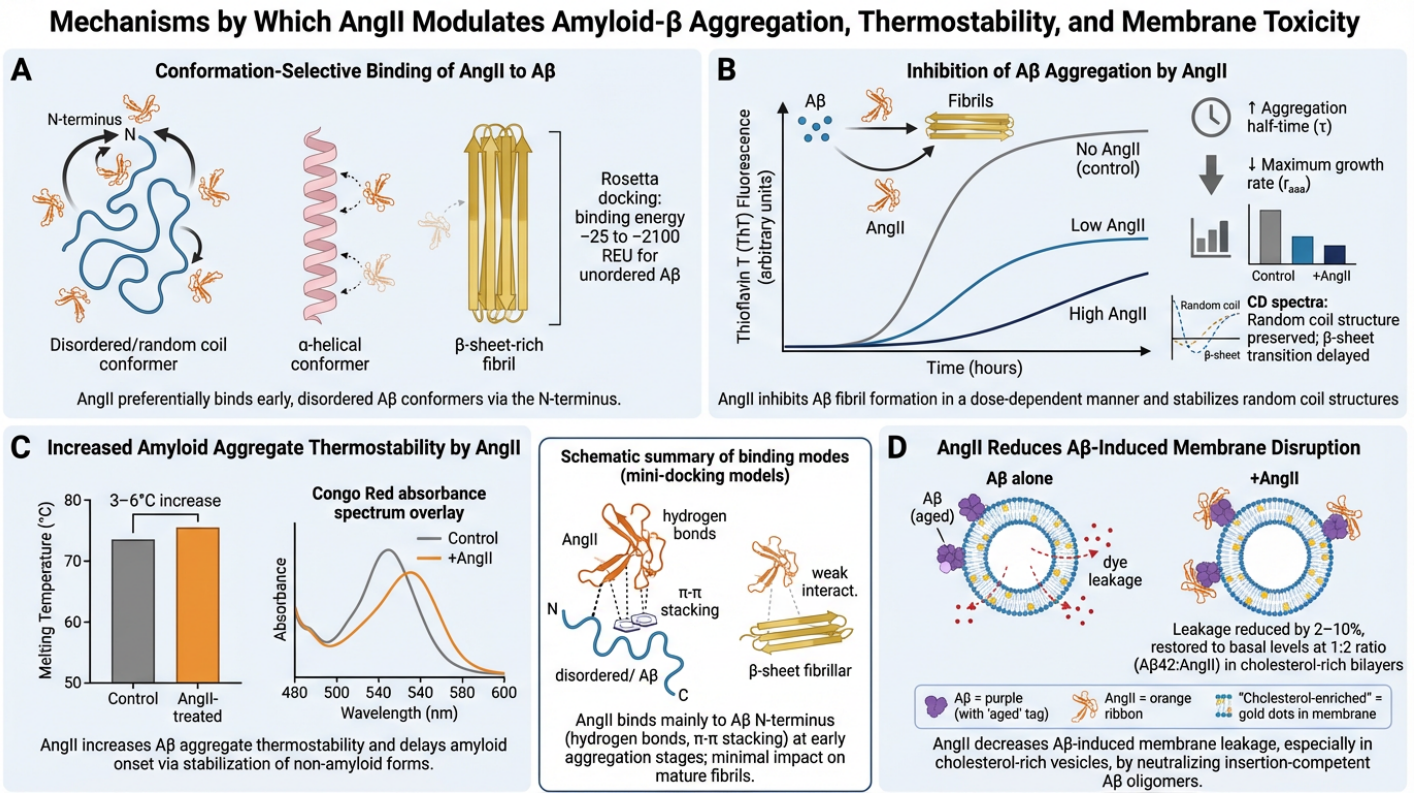


Figure 33. Ang II modulate Aβ aggregation, thermostability and membrane toxicity. (Created by figurelabs.ai).

Chapter III: Heterotypic interaction between Dynorphin A variants and amyloid-β42

11. Wild-type DynA modestly attenuates the final $A\beta_{42}$ fibril plateau and mildly accelerates the aggregation half-time in ThT fluorescence assays, extending to $A\beta_{42}$ the weak modulatory activity previously unreported for DynA against $A\beta_{40}$. This isoform-dependent difference is consistent with the lower nucleation barrier and greater hydrophobic surface area of $A\beta_{42}$, which may lower the threshold for productive DynA interaction.

12. The SCA23-linked clinical variants deviate profoundly from wild-type DynA. DynA L5S induces an approximately fourfold amplification of ThT amplitude and a near-instantaneous nucleation event ($\tau \approx 10$ min at 1:2 molar ratio), while R6W and R9C show intermediate effects on ordered assembly. All three clinical variants generate disproportionately elevated Bis-ANS amplitudes (up to 24-fold above the $A\beta_{42}$-alone control for L5S), indicating that the pathogenic substitutions redirect $A\beta_{42}$ preferentially toward amorphous, hydrophobic co-aggregates rather than canonical amyloid fibrils.

13. The uncoupling of ThT and Bis-ANS kinetic signals in the presence of DynA clinical variants identifies a mechanistic shift: rather than accelerating canonical fibrillization, the pathogenic substitutions steer $A\beta_{42}$ into solvent-exposed, amorphous co-assemblies whose membrane-disruptive and proteotoxic potential may exceed that of ordered fibrils.

14. DynA-induced membrane disruption is strictly dependent on electrostatic attraction: all variants show negligible leakage in neutral POPC bilayers, while introduction of 30 mol% POPG sensitizes membranes and allows R6W and R9C to achieve near-complete permeabilization at 1:10 peptide-to-lipid ratios. Cholesterol partially attenuates but does not abolish this activity, with R6W and R9C retaining significant disruptive capacity in POPC:POPG:Chol bilayers.

15. A consistent activity hierarchy (DynA R6W > R9C > L5S ≈ WT) is observed across all membrane compositions and peptide-to-lipid ratios tested, identifying reduction of net cationic charge (R9C) and aromatic enhancement through tryptophan's indole ring (R6W)

as the primary molecular determinants of pathological membrane activity among the SCA23 clinical variants.

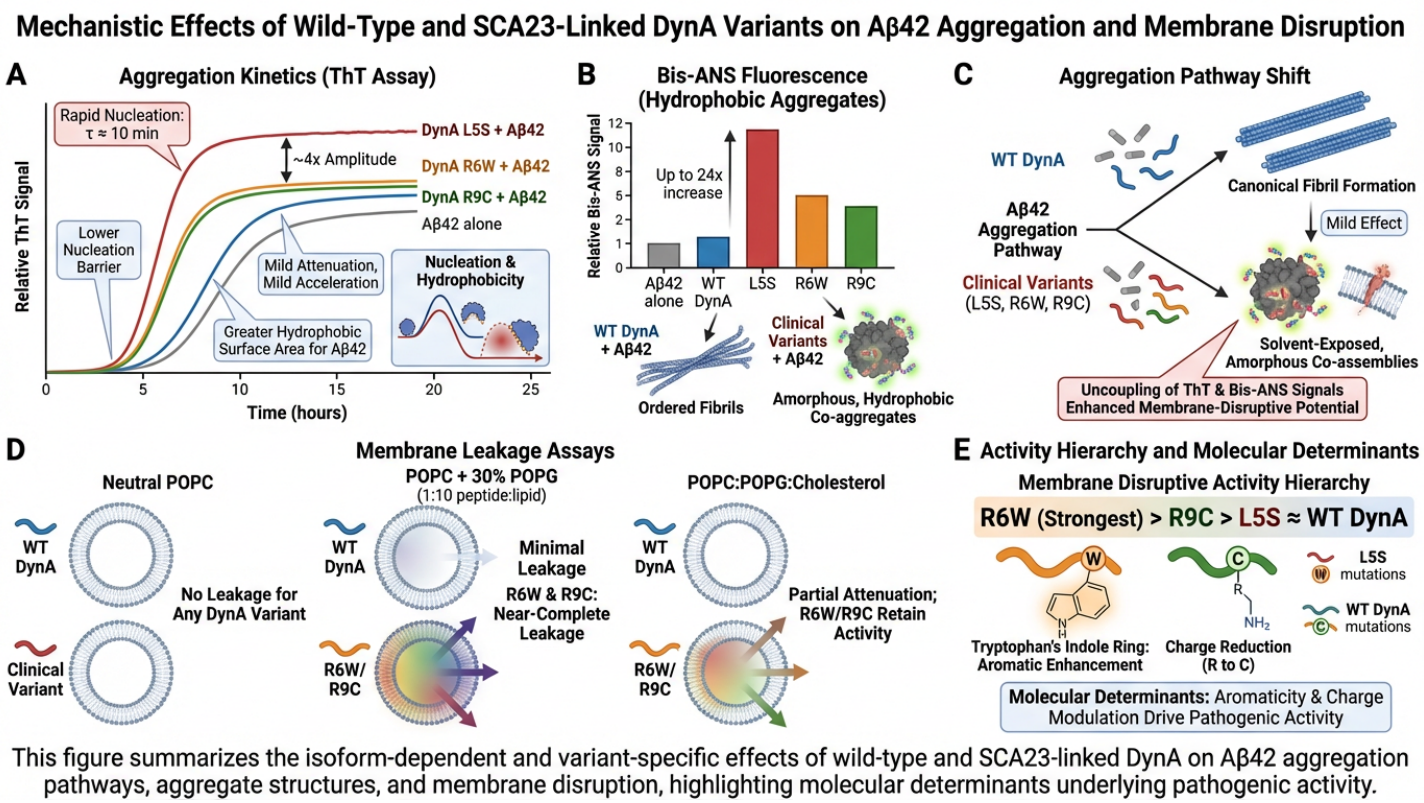


Figure 34. Mechanistic effects of Dyn A variants on Aβ42 aggregation and membrane disruption. (Created by figurelabs.ai).

General conclusions

16. NKA, AngII, and wild-type DynA share a common mechanistic logic as endogenous modulators of the Aβ amyloid pathway: all three preferentially engage early, disordered or helical Aβ conformers, converging on the central hydrophobic core and adjacent aggregation-prone regions as the principal interaction surface, and collectively delaying the conformational transition from random coil or helix to β-sheet that underpins nucleation and fibril growth.

17. The SCA23-linked DynA clinical variants subvert the protective modulatory role of wild-type DynA, redirecting $A\beta_{42}$ toward amorphous, hydrophobic co-aggregates and synergistically amplifying membrane disruption. This gain-of-function neurotoxic mechanism, contrasted with the neuroprotective activity of the full-length prodynorphin-derived precursor BigDyn[98], positions the dynorphin processing state and genetic variant as determinants of whether the opioid neuropeptide system contributes to or counteracts amyloid proteostasis.

18. The three heterotypic neuropeptide-Aβ interactions described in this thesis collectively support the view that endogenous neuropeptide networks constitute a conformation-selective proteostatic checkpoint of the amyloid cascade, whose progressive failure through depletion, sequestration, or pathological mutation may represent one of the earliest molecular events in AD pathogenesis. These findings provide a mechanistic foundation for the rational design of peptide-based therapeutic and diagnostic strategies targeting heterotypic neuropeptide-Aβ interactions in Alzheimer's disease.

FUTURE PERSPECTIVES

Looking ahead, future investigations could explore in vivo models to validate these interactions in physiological contexts, probe the therapeutic efficacy of NKA analogs or Phe modified variants in animal models of AD, and delve into how disruptions in tachykinin signaling might exacerbate amyloid burden.

For Ang II future directions, extending these observations to in vivo settings could assess AngII's impact on plaque formation in transgenic AD models, investigate synergies with existing RAS

inhibitors like ACE blockers for amyloid clearance, and examine whether genetic variations in RAS components correlate with AD risk.

AI Declaration

Figures 32, 33, and 34 in this thesis were generated using the artificial intelligence image generation tool Figurelabs.ai.

During the preparation of Chapter III, COPILOT was used in order to improve the readability of the content. After using this tool/service, the content was reviewed and edited as needed.

REFERENCES

1. Gustavsson, A. et al. Global estimates on the number of persons across the Alzheimer's disease continuum. Alzheimer's & Dementia **19**, 658–670 (2023).
2. Nichols, E. et al. Estimation of the global prevalence of dementia in 2019 and forecasted prevalence in 2050: an analysis for the Global Burden of Disease Study 2019. Lancet Public Health **7**, e105–e125 (2022).
3. Jost, B. C. & Grossberg, G. T. The Evolution of Psychiatric Symptoms in Alzheimer's Disease: A Natural History Study. J. Am. Geriatr. Soc. **44**, 1078–1081 (1996).
4. Merriam, A. E., Aronson, M. K., Gaston, P., Wey, S.-L. & Katz, I. The Psychiatric Symptoms of Alzheimer's Disease. J. Am. Geriatr. Soc. **36**, 7–22 (1988).
5. Koedam, E. L. G. E. et al. Early-Versus Late-Onset Alzheimer's Disease: More than Age Alone. Journal of Alzheimer's Disease **19**, 1401–1408 (2010).
6. Luo, J., Wärmländer, S. K. T. S., Gräslund, A. & Abrahams, J. P. Alzheimer Peptides Aggregate into Transient Nanoglobules That Nucleate Fibrils. Biochemistry **53**, 6302–6308 (2014).
7. Gessel, M. M., Bernstein, S., Kemper, M., Teplow, D. B. & Bowers, M. T. Familial Alzheimer's Disease Mutations Differentially Alter Amyloid β-Protein Oligomerization. ACS Chem. Neurosci. **3**, 909–918 (2012).
8. Porquet, D. et al. Amyloid and tau pathology of familial Alzheimer's disease APP/PS1 mouse model in a senescence phenotype background (SAMP8). Age (Omaha). **37**, 12 (2015).
9. Dong, Y. et al. Hyperphosphorylated tau mediates neuronal death by inducing necroptosis and inflammation in Alzheimer's disease. J. Neuroinflammation **19**, 205 (2022).
10. Milà-Alomà, M. et al. Plasma p-tau231 and p-tau217 as state markers of amyloid-β pathology in preclinical Alzheimer's disease. Nat. Med. https://doi.org/10.1038/s41591-022-01925-w (2022) doi:10.1038/s41591-022-01925-w.
11. Hardy, J. A. & Higgins, G. A. Alzheimer's Disease: The Amyloid Cascade Hypothesis. Science (1979). **256**, 184–185 (1992).
12. Sweeney, M. D., Sagare, A. P. & Zlokovic, B. V. Blood–brain barrier breakdown in Alzheimer disease and other neurodegenerative disorders. Nat. Rev. Neurol. **14**, 133–150 (2018).
13. Gómez-Isla, T. et al. Neuronal loss correlates with but exceeds neurofibrillary tangles in Alzheimer's disease. Ann. Neurol. **41**, 17–24 (1997).
14. Lacor, P. N. et al. Aβ Oligomer-Induced Aberrations in Synapse Composition, Shape, and Density Provide a Molecular Basis for Loss of Connectivity in Alzheimer's Disease. The Journal of Neuroscience **27**, 796–807 (2007).
15. Marsh, J. & Alifragis, P. Synaptic dysfunction in Alzheimer's disease: the effects of amyloid beta on synaptic vesicle dynamics as a novel target for therapeutic intervention. Neural Regen. Res. **13**, 616 (2018).
16. González, A., Geywitz, S. & Maccioni, R. B. Alzheimer's disease: where do we stand now and what are the strategic interventions? Front. Cell. Neurosci. **19**, (2025).

17. Reitz, C. Alzheimer's Disease and the Amyloid Cascade Hypothesis: A Critical Review. Int. J. Alzheimers Dis. **2012**, 1–11 (2012).
18. Glenner, G. G. & Wong, C. W. Alzheimer's disease: Initial report of the purification and characterization of a novel cerebrovascular amyloid protein. Biochem. Biophys. Res. Commun. **120**, 885–890 (1984).
19. Yankner, B. A. et al. Neurotoxicity of a Fragment of the Amyloid Precursor Associated with Alzheimer's Disease. Science (1979). **245**, 417–420 (1989).
20. Goate, A. et al. Segregation of a missense mutation in the amyloid precursor protein gene with familial Alzheimer's disease. Nature **349**, 704–706 (1991).
21. Zhang, J. et al. Recent advances in Alzheimer's disease: mechanisms, clinical trials and new drug development strategies. Signal Transduct. Target. Ther. **9**, 211 (2024).
22. Cohen, S. I. A. et al. Proliferation of amyloid-β42 aggregates occurs through a secondary nucleation mechanism. Proceedings of the National Academy of Sciences **110**, 9758–9763 (2013).
23. Rodriguez Camargo, D. C. et al. Proliferation of Tau 304–380 Fragment Aggregates through Autocatalytic Secondary Nucleation. ACS Chem. Neurosci. **12**, 4406–4415 (2021).
24. Cameron, D. J. et al. Alzheimer's-Related Peptide Amyloid-β Plays a Conserved Role in Angiogenesis. PLoS One **7**, e39598 (2012).
25. Puzzo, D. et al. Picomolar Amyloid-β Positively Modulates Synaptic Plasticity and Memory in Hippocampus. The Journal of Neuroscience **28**, 14537–14545 (2008).
26. Cai, W., Li, L., Sang, S., Pan, X. & Zhong, C. Physiological Roles of β-amyloid in Regulating Synaptic Function: Implications for AD Pathophysiology. Neurosci. Bull. **39**, 1289–1308 (2023).
27. Mori, H., Takio, K., Ogawara, M. & Selkoe, D. J. Mass spectrometry of purified amyloid beta protein in Alzheimer's disease. Journal of Biological Chemistry **267**, 17082–17086 (1992).
28. Kitaguchi, N., Takahashi, Y., Tokushima, Y., Shiojiri, S. & Ito, H. Novel precursor of Alzheimer's disease amyloid protein shows protease inhibitory activity. Nature **331**, 530–532 (1988).
29. Preece, P. et al. Amyloid precursor protein mRNA levels in Alzheimer's disease brain. Molecular Brain Research **122**, 1–9 (2004).
30. Gao, Y. & Pimplikar, S. W. The γ-secretase-cleaved C-terminal fragment of amyloid precursor protein mediates signaling to the nucleus. Proceedings of the National Academy of Sciences **98**, 14979–14984 (2001).
31. Esch, F. S. et al. Cleavage of Amyloid β Peptide During Constitutive Processing of Its Precursor. Science (1979). **248**, 1122–1124 (1990).
32. Roher, A. E. et al. beta-Amyloid-(1-42) is a major component of cerebrovascular amyloid deposits: implications for the pathology of Alzheimer disease. Proceedings of the National Academy of Sciences **90**, 10836–10840 (1993).
33. Suzuki, N. et al. An Increased Percentage of Long Amyloid β Protein Secreted by Familial Amyloid β Protein Precursor (βApp $_{717}$) Mutants. Science (1979). **264**, 1336–1340 (1994).
34. De Strooper, B. et al. Deficiency of presenilin-1 inhibits the normal cleavage of amyloid precursor protein. Nature **391**, 387–390 (1998).

35. Vassar, R. et al. β-Secretase Cleavage of Alzheimer's Amyloid Precursor Protein by the Transmembrane Aspartic Protease BACE. Science (1979). **286**, 735–741 (1999).
36. Benseny-Cases, N., Klementieva, O. & Cladera, J. In vitroOligomerization and Fibrillogenesis of Amyloid-beta Peptides. in 53–74 (2012). doi:10.1007/978-94-007-5416-4_3.
37. Viswanathan, A. & Greenberg, S. M. Cerebral amyloid angiopathy in the elderly. Ann. Neurol. **70**, 871–880 (2011).
38. Eisenberg, D. S. & Sawaya, M. R. Structural Studies of Amyloid Proteins at the Molecular Level. Annu. Rev. Biochem. **86**, 69–95 (2017).
39. Nelson, R. & Eisenberg, D. Recent atomic models of amyloid fibril structure. Curr. Opin. Struct. Biol. **16**, 260–265 (2006).
40. Golde, T. E., Eckman, C. B. & Younkin, S. G. Biochemical detection of Aβ isoforms: implications for pathogenesis, diagnosis, and treatment of Alzheimer's disease. Biochimica et Biophysica Acta (BBA) - Molecular Basis of Disease **1502**, 172–187 (2000).
41. Potter, R. et al. Increased in Vivo Amyloid-β42 Production, Exchange, and Loss in Presenilin Mutation Carriers. Sci. Transl. Med. **5**, (2013).
42. Kuperstein, I. et al. Neurotoxicity of Alzheimer's disease Aβ peptides is induced by small changes in the Aβ42 to Aβ40 ratio. EMBO J. **29**, 3408–3420 (2010).
43. Patterson, B. W. et al. Age and amyloid effects on human central nervous system amyloid-beta kinetics. Ann. Neurol. **78**, 439–453 (2015).
44. Westermark, G. T., Johnson, K. H. & Westermark, P. [1] Staining methods for identification of amyloid in tissue. in 3–25 (1999). doi:10.1016/S0076-6879(99)09003-5.
45. Mantha, A. K., Moorthy, K., Cowsik, S. M. & Baquer, N. Z. Neuroprotective Role of Neurokinin B (NKB) on β-amyloid (25–35) Induced Toxicity in Aging Rat Brain Synaptosomes: Involvement in Oxidative Stress and Excitotoxicity. Biogerontology **7**, 1–17 (2006).
46. Daschil, N. et al. L-type calcium channel blockers and substance P induce angiogenesis of cortical vessels associated with beta-amyloid plaques in an Alzheimer mouse model. Neurobiol. Aging **36**, 1333–1341 (2015).
47. Tams, A. L. M. et al. Decreased Glucose Metabolism and Glutamine Synthesis in the Retina of a Transgenic Mouse Model of Alzheimer's Disease. Cell. Mol. Neurobiol. **42**, 291–303 (2022).
48. Chen, S.-H. et al. Amyloid-beta uptake by blood monocytes is reduced with ageing and Alzheimer's disease. Transl. Psychiatry **10**, 423 (2020).
49. Maarouf, C. L. et al. Impaired hepatic amyloid-beta degradation in Alzheimer's disease. PLoS One **13**, e0203659 (2018).
50. Carare, R. O. Editorial: Clearance Pathways for Amyloid-β. Significance for Alzheimer's Disease and Its Therapy. Front. Aging Neurosci. **9**, (2017).
51. Cheng, Y., Tian, D.-Y. & Wang, Y.-J. Peripheral clearance of brain-derived Aβ in Alzheimer's disease: pathophysiology and therapeutic perspectives. Transl. Neurodegener. **9**, 16 (2020).
52. Vegas-Suárez, S., Simón, J., Martínez-Chantar, M. L. & Moratalla, R. Metabolic Diffusion in Neuropathologies: The Relevance of Brain-Liver Axis. Front. Physiol. **13**, (2022).

53. Darabi, S., Gorgich, E. A. C., Moradi, F. & Rustamzadeh, A. Lipidopathy disrupts peripheral and central amyloid clearance in Alzheimer's disease: Where are our knowledge. IBRO Neurosci. Rep. **18**, 191–199 (2025).
54. Iwata, N. et al. Metabolic Regulation of Brain Aβ by Neprilysin. Science (1979). **292**, 1550–1552 (2001).
55. Eckman, E. A., Reed, D. K. & Eckman, C. B. Degradation of the Alzheimer's Amyloid β Peptide by Endothelin-converting Enzyme. Journal of Biological Chemistry **276**, 24540–24548 (2001).
56. Farris, W. et al. Insulin-degrading enzyme regulates the levels of insulin, amyloid β-protein, and the β-amyloid precursor protein intracellular domain in vivo. Proceedings of the National Academy of Sciences **100**, 4162–4167 (2003).
57. Shibata, M. et al. Clearance of Alzheimer's amyloid-β1-40 peptide from brain by LDL receptor–related protein-1 at the blood-brain barrier. Journal of Clinical Investigation **106**, 1489–1499 (2000).
58. Deane, R. et al. A multimodal RAGE-specific inhibitor reduces amyloid β–mediated brain disorder in a mouse model of Alzheimer disease. Journal of Clinical Investigation **122**, 1377–1392 (2012).
59. Storck, S. E. et al. Endothelial LRP1 transports amyloid-β1–42 across the blood-brain barrier. Journal of Clinical Investigation **126**, 123–136 (2015).
60. Sagare, A. et al. Clearance of amyloid-β by circulating lipoprotein receptors. Nat. Med. **13**, 1029–1031 (2007).
61. Lockwood, G. P. et al. Understanding the Liver's Role in the Clearance of Aβ40. Livers **4**, 253–267 (2024).
62. Petrella, C. et al. Neuropeptides in Alzheimer's Disease: An Update. Curr. Alzheimer Res. **16**, 544–558 (2019).
63. Holzer, P. & Farzi, A. Neuropeptides and the Microbiota-Gut-Brain Axis. in 195–219 (2014). doi:10.1007/978-1-4939-0897-4_9.
64. Chen, X.-Y., Du, Y.-F. & Chen, L. Neuropeptides Exert Neuroprotective Effects in Alzheimer's Disease. Front. Mol. Neurosci. **11**, (2019).
65. Ben-Shushan, S. & Miller, Y. Neuropeptides: Roles and Activities as Metal Chelators in Neurodegenerative Diseases. J. Phys. Chem. B **125**, 2796–2811 (2021).
66. Clavaguera, F. et al. Transmission and spreading of tauopathy in transgenic mouse brain. Nat. Cell Biol. **11**, 909–913 (2009).
67. Ittner, L. M. & Götz, J. Amyloid-β and tau — a toxic pas de deux in Alzheimer's disease. Nat. Rev. Neurosci. **12**, 67–72 (2011).
68. Mattsson-Carlgren, N. et al. Aβ deposition is associated with increases in soluble and phosphorylated tau that precede a positive Tau PET in Alzheimer's disease. Sci. Adv. **6**, (2020).
69. Yang, M.-X. et al. Albumin antagonizes Alzheimer's disease-related Tau pathology and enhances cognitive performance by inhibiting aberrant Tau aggregation. Exp. Neurol. **386**, 115155 (2025).
70. Loch, R. A. et al. Cross interactions between Apolipoprotein E and amyloid proteins in neurodegenerative diseases. Comput. Struct. Biotechnol. J. **21**, 1189–1204 (2023).

71. Ferrari-Souza, J. P. et al. APOEε4 potentiates amyloid β effects on longitudinal tau pathology. Nat. Aging **3**, 1210–1218 (2023).
72. Zhang, H. et al. Longitudinal effects of sex differences and apolipoprotein E genotype on white matter engagement among elderly. Brain Commun. **7**, (2025).
73. Konstantoulea, K. et al. Heterotypic Amyloid β interactions facilitate amyloid assembly and modify amyloid structure. EMBO J. **41**, (2022).
74. Louros, N. et al. Mapping the sequence specificity of heterotypic amyloid interactions enables the identification of aggregation modifiers. Nat. Commun. **13**, 1351 (2022).
75. López de la Paz, M. & Serrano, L. Sequence determinants of amyloid fibril formation. Proceedings of the National Academy of Sciences **101**, 87–92 (2004).
76. Xu, Y. et al. Conformational transition of amyloid β-peptide. Proceedings of the National Academy of Sciences **102**, 5403–5407 (2005).
77. Reidy, M. & Masison, D. C. Mutations in the Hsp90 N Domain Identify a Site that Controls Dimer Opening and Expand Human Hsp90α Function in Yeast. J. Mol. Biol. **432**, 4673–4689 (2020).
78. Xiao, Y. et al. Aβ(1–42) fibril structure illuminates self-recognition and replication of amyloid in Alzheimer's disease. Nat. Struct. Mol. Biol. **22**, 499–505 (2015).
79. Kirkitadze, M. D., Condron, M. M. & Teplow, D. B. Identification and characterization of key kinetic intermediates in amyloid β-protein fibrillogenesis11Edited by F. Cohen. J. Mol. Biol. **312**, 1103–1119 (2001).
80. Valerio, M. et al. pH Effects on the Conformational Preferences of Amyloid β-Peptide (1–40) in HFIP Aqueous Solution by NMR Spectroscopy. ChemMedChem **3**, 833–843 (2008).
81. Abelein, A., Jarvet, J., Barth, A., Gräslund, A. & Danielsson, J. Ionic Strength Modulation of the Free Energy Landscape of $A\beta_{40}$ Peptide Fibril Formation. J. Am. Chem. Soc. **138**, 6893–6902 (2016).
82. Kengwerere, M. K. et al. Structural convergence and membrane interactions of Aβ1-42 along the primary nucleation process studied by solid state NMR. Commun. Chem. **8**, 131 (2025).
83. Sahoo, A. & Matysiak, S. Effects of applied surface-tension on membrane-assisted Aβ aggregation. Physical Chemistry Chemical Physics **23**, 20627–20633 (2021).
84. Österlund, N. et al. Amyloid-β Peptide Interactions with Amphiphilic Surfactants: Electrostatic and Hydrophobic Effects. ACS Chem. Neurosci. **9**, 1680–1692 (2018).
85. Fatafta, H., Kav, B., Bundschuh, B. F., Loschwitz, J. & Strodel, B. Disorder-to-order transition of the amyloid-β peptide upon lipid binding. Biophys. Chem. **280**, 106700 (2022).
86. Shapovalova, K. et al. The Role of Neuropeptide Y in the Pathogenesis of Alzheimer's Disease: Diagnostic Significance and Neuroprotective Functions. Neurol. Int. **16**, 1318–1331 (2024).
87. Cho, P. Y., Joshi, G., Johnson, J. A. & Murphy, R. M. Transthyretin-Derived Peptides as β-Amyloid Inhibitors. ACS Chem. Neurosci. **5**, 542–551 (2014).
88. Li, Z.-H., Li, B., Zhang, X.-Y. & Zhu, J.-N. Neuropeptides and Their Roles in the Cerebellum. Int. J. Mol. Sci. **25**, 2332 (2024).
89. Sharma, D., Kumar, K. & Bisht, G. S. A Mini-Review on Potential of Neuropeptides as Future Therapeutics. Int. J. Pept. Res. Ther. **28**, 39 (2022).

90. Perry, R. H. et al. Neuropeptides in Alzheimer's disease, depression and schizophrenia. J. Neurol. Sci. **51**, 465–472 (1981).
91. Banks, W. A. Peptides and the blood–brain barrier. Peptides (N.Y.). **72**, 16–19 (2015).
92. Williams, D. et al. Somatostatin slows Aβ plaque deposition in aged APPNL-F/NL-F mice by blocking Aβ aggregation. Sci. Rep. **13**, 2337 (2023).
93. Wang, H. et al. Somatostatin binds to the human amyloid β peptide and favors the formation of distinct oligomers. Elife **6**, (2017).
94. Sastre, M. et al. Binding of cystatin C to Alzheimer's amyloid β inhibits in vitro amyloid fibril formation. Neurobiol. Aging **25**, 1033–1043 (2004).
95. Sun, B. et al. Cystatin C-Cathepsin B Axis Regulates Amyloid Beta Levels and Associated Neuronal Deficits in an Animal Model of Alzheimer's Disease. Neuron **60**, 247–257 (2008).
96. Flashner, E., Raviv, U. & Friedler, A. The effect of tachykinin neuropeptides on amyloid β aggregation. Biochem. Biophys. Res. Commun. **407**, 13–17 (2011).
97. Habibnia, M., Catalina-Hernandez, E., Lopez-Martin, M., Masnou-Sanchez, D. & Peralvarez-Marin, A. Decoding the molecular and structural determinants of the neurokinin A and Aβ1-42 peptide cross-interaction in the amyloid cascade pathway. iScience **27**, 111187 (2024).
98. Gallego-Villarejo, L. et al. Big dynorphin is a neuroprotector scaffold against amyloid β-peptide aggregation and cell toxicity. Comput. Struct. Biotechnol. J. **20**, 5672–5679 (2022).
99. Kowall, N. W., Beal, M. F., Busciglio, J., Duffy, L. K. & Yankner, B. A. An in vivo model for the neurodegenerative effects of beta amyloid and protection by substance P. Proceedings of the National Academy of Sciences **88**, 7247–7251 (1991).
100. Campolongo, P. et al. Systemic Administration of Substance P Recovers Beta Amyloid-Induced Cognitive Deficits in Rat: Involvement of Kv Potassium Channels. PLoS One **8**, e78036 (2013).
101. Habibnia, M. et al. Biophysical analysis of angiotensin <scp>II</scp> and amyloid-β cross-interaction in aggregation and membrane disruption. FEBS Lett. **600**, 109–118 (2026).
102. Song, M. et al. VIP Enhances Phagocytosis of Fibrillar Beta-Amyloid by Microglia and Attenuates Amyloid Deposition in the Brain of APP/PS1 Mice. PLoS One **7**, e29790 (2012).
103. Kang, J.-E. et al. Amyloid-β Dynamics Are Regulated by Orexin and the Sleep-Wake Cycle. Science (1979). **326**, 1005–1007 (2009).
104. Croce, N. et al. Neuropeptide Y Protects Rat Cortical Neurons against β-Amyloid Toxicity and Re-establishes Synthesis and Release of Nerve Growth Factor. ACS Chem. Neurosci. **3**, 312–318 (2012).
105. Reich, N. & Hölscher, C. Cholecystokinin (CCK): a neuromodulator with therapeutic potential in Alzheimer's and Parkinson's disease. Front. Neuroendocrinol. **73**, 101122 (2024).
106. Takahashi, J. et al. Intracerebroventricular administration of oxytocin and intranasal administration of the oxytocin derivative improve β-amyloid peptide (25–35)-induced memory impairment in mice. Neuropsychopharmacol. Rep. **42**, 492–501 (2022).

107. Jing, W., Guo, F., Cheng, L., Zhang, J.-F. & Qi, J.-S. Arginine vasopressin prevents amyloid β protein-induced impairment of long-term potentiation in rat hippocampus in vivo. Neurosci. Lett. **450**, 306–310 (2009).
108. Elliott-Hunt, C. R. et al. Endogenous Galanin Protects Mouse Hippocampal Neurons Against Amyloid Toxicity in vitro via Activation of Galanin Receptor-2. Journal of Alzheimer's Disease **25**, 455–462 (2011).
109. Song, J., Choi, S.-M. & Kim, B. C. Adiponectin Regulates the Polarization and Function of Microglia via PPAR-γ Signaling Under Amyloid β Toxicity. Front. Cell. Neurosci. **11**, (2017).
110. Luo, H. et al. Apelin-13 Suppresses Neuroinflammation Against Cognitive Deficit in a Streptozotocin-Induced Rat Model of Alzheimer's Disease Through Activation of BDNF-TrkB Signaling Pathway. Front. Pharmacol. **10**, (2019).
111. Futran-Sheinberg, E. J. et al. Pro- and Anti-Inflammatory Neuropeptides and Glia: The Balance Between Neuroprotection and Neuroinflammation. Neuroglia **6**, 35 (2025).
112. Reichlin, S. Somatostatin. New England Journal of Medicine **309**, 1495–1501 (1983).
113. Severini, C., Petrella, C. & Calissano, P. Substance P and Alzheimer's Disease: Emerging Novel Roles. Curr. Alzheimer Res. **13**, 964–972 (2016).
114. Gahete, M. D. et al. Expression of the Ghrelin and Neurotensin Systems is Altered in the Temporal Lobe of Alzheimer's Disease Patients. Journal of Alzheimer's Disease **22**, 819–828 (2010).
115. Kojro, E. et al. The neuropeptide PACAP promotes ?-secretase pathway for processing Alzheimer amyloid precursor protein. The FASEB Journal **20**, 512–514 (2006).
116. Inutsuka, A. & Yamanaka, A. The physiological role of orexin/hypocretin neurons in the regulation of sleep/wakefulness and neuroendocrine functions. Front. Endocrinol. (Lausanne). **4**, (2013).
117. Faller, P. Copper and Zinc Binding to Amyloid-β: Coordination, Dynamics, Aggregation, Reactivity and Metal-Ion Transfer. ChemBioChem **10**, 2837–2845 (2009).
118. Maynard, C. J., Bush, A. I., Masters, C. L., Cappai, R. & Li, Q.-X. Metals and amyloid-β in Alzheimer's disease. Int. J. Exp. Pathol. **86**, 147–159 (2005).
119. Wallin, C. et al. Metal ion coordination delays amyloid-β peptide self-assembly by forming an aggregation–inert complex. Journal of Biological Chemistry **295**, 7224–7234 (2020).
120. Watamura, N. et al. Somatostatin-evoked Aβ catabolism in the brain: Mechanistic involvement of α-endosulfine-KATP channel pathway. Mol. Psychiatry **27**, 1816–1828 (2022).
121. Saxena, S. K. et al. Neprilysin-Mediated Amyloid Beta Clearance and Its Therapeutic Implications in Neurodegenerative Disorders. ACS Pharmacol. Transl. Sci. **7**, 3645–3657 (2024).
122. Rose, J. B. et al. Neuropeptide Y Fragments Derived from Neprilysin Processing Are Neuroprotective in a Transgenic Model of Alzheimer's Disease. The Journal of Neuroscience **29**, 1115–1125 (2009).
123. Hüttenrauch, M. et al. Neprilysin Deficiency Alters the Neuropathological and Behavioral Phenotype in the 5XFAD Mouse Model of Alzheimer's Disease. Journal of Alzheimer's Disease **44**, 1291–1302 (2015).

124. Rai, S. N. et al. The Role of PI3K/Akt and ERK in Neurodegenerative Disorders. Neurotox. Res. **35**, 775–795 (2019).
125. Mao, Q. et al. The Pathologic Roles and Therapeutic Implications of Ghrelin/GHSR System in Mental Disorders. Depress. Anxiety **2024**, (2024).
126. Xiao, Z. et al. Activation of Neurotensin Receptor 1 Facilitates Neuronal Excitability and Spatial Learning and Memory in the Entorhinal Cortex: Beneficial Actions in an Alzheimer's Disease Model. The Journal of Neuroscience **34**, 7027–7042 (2014).
127. Onoue, S., Endo, K., Ohshima, K., Yajima, T. & Kashimoto, K. The neuropeptide PACAP attenuates β-amyloid (1–42)-induced toxicity in PC12 cells. Peptides (N.Y.). **23**, 1471–1478 (2002).
128. Yamamoto, N., Tanida, M., Kasahara, R., Sobue, K. & Suzuki, K. Leptin inhibits amyloid β-protein fibrillogenesis by decreasing GM1 gangliosides on the neuronal cell surface through PI3K/Akt/mTOR pathway. J. Neurochem. **131**, 323–332 (2014).
129. Henning-Knechtel, A. et al. Designed Cell-Penetrating Peptide Inhibitors of Amyloid-beta Aggregation and Cytotoxicity. Cell Rep. Phys. Sci. **1**, 100014 (2020).
130. Puig, E., Tolchard, J., Riera, A. & Carulla, N. Somatostatin, an In Vivo Binder to Aβ Oligomers, Binds to βPFO $_{Aβ(1–42)}$ Tetramers. ACS Chem. Neurosci. **11**, 3358–3365 (2020).
131. Bode, D. C., Freeley, M., Nield, J., Palma, M. & Viles, J. H. Amyloid-β oligomers have a profound detergent-like effect on lipid membrane bilayers, imaged by atomic force and electron microscopy. Journal of Biological Chemistry **294**, 7566–7572 (2019).
132. Sciacca, M. F. M., La Rosa, C. & Milardi, D. Amyloid-Mediated Mechanisms of Membrane Disruption. Biophysica **1**, 137–156 (2021).
133. Urbanc, B. et al. Structural Basis for Aβ1–42 Toxicity Inhibition by Aβ C-Terminal Fragments: Discrete Molecular Dynamics Study. J. Mol. Biol. **410**, 316–328 (2011).
134. Serra-Batiste, M. et al. Aβ42 assembles into specific β-barrel pore-forming oligomers in membrane-mimicking environments. Proceedings of the National Academy of Sciences **113**, 10866–10871 (2016).
135. Lee, J. et al. Amyloid β Ion Channels in a Membrane Comprising Brain Total Lipid Extracts. ACS Chem. Neurosci. **8**, 1348–1357 (2017).
136. Sciacca, M. F. M. et al. Two-Step Mechanism of Membrane Disruption by Aβ through Membrane Fragmentation and Pore Formation. Biophys. J. **103**, 702–710 (2012).
137. Rosenberry, T. L., Zhou, H.-X., Stagg, S. M. & Paravastu, A. K. Oligomer Formation by Amyloid-β42 in a Membrane-Mimicking Environment in Alzheimer's Disease. Molecules **27**, 8804 (2022).
138. Delgado, D. A. et al. Distinct Membrane Disruption Pathways Are Induced by 40-Residue β-Amyloid Peptides. Journal of Biological Chemistry **291**, 12233–12244 (2016).
139. McLaurin, J. & Chakrabartty, A. Membrane Disruption by Alzheimer β-Amyloid Peptides Mediated through Specific Binding to Either Phospholipids or Gangliosides. Journal of Biological Chemistry **271**, 26482–26489 (1996).
140. Chi, E. Y., Frey, S. L. & Lee, K. Y. C. Ganglioside G $_{M1}$ -Mediated Amyloid-beta Fibrillogenesis and Membrane Disruption. Biochemistry **46**, 1913–1924 (2007).
141. Di Scala, C. et al. Common molecular mechanism of amyloid pore formation by Alzheimer's β-amyloid peptide and α-synuclein. Sci. Rep. **6**, 28781 (2016).

142. Fernández-Pérez, E. J. et al. Effect of Cholesterol on Membrane Fluidity and Association of Aβ Oligomers and Subsequent Neuronal Damage: A Double-Edged Sword. Front. Aging Neurosci. **10**, (2018).
143. Rudajev, V. & Novotny, J. Cholesterol as a key player in amyloid β-mediated toxicity in Alzheimer's disease. Front. Mol. Neurosci. **15**, (2022).
144. Krause, M. R. & Regen, S. L. The Structural Role of Cholesterol in Cell Membranes: From Condensed Bilayers to Lipid Rafts. Acc. Chem. Res. **47**, 3512–3521 (2014).
145. Pantelopulos, G. A., Abraham, C. B. & Straub, J. E. Cholesterol and Lipid Rafts in the Biogenesis of Amyloid-β Protein and Alzheimer's Disease. Annu. Rev. Biophys. **53**, 455–486 (2024).
146. Hane, F., Drolle, E., Gaikwad, R., Faught, E. & Leonenko, Z. Amyloid-β Aggregation on Model Lipid Membranes: An Atomic Force Microscopy Study. Journal of Alzheimer's Disease **26**, 485–494 (2011).
147. Viles, J. H. Imaging Amyloid-β Membrane Interactions: Ion-Channel Pores and Lipid-Bilayer Permeability in Alzheimer's Disease. Angew. Chem. Int. Ed. **62**, (2023).
148. Advances in Enzymology and Related Areas of Molecular Biology. vol. 64 (Wiley, 1991).
149. Reviews in Computational Chemistry. vol. 17 (Wiley, 2001).
150. Dodero, V. I. Biomolecular studies by circular dichroism. Frontiers in Bioscience **16**, 61 (2011).
151. De Carlo, S. & Harris, J. R. Negative staining and cryo-negative staining of macromolecules and viruses for TEM. Micron **42**, 117–131 (2011).
152. Goodhew, P. J., Humphreys, J. & Humphreys, J. Electron Microscopy and Analysis. (CRC Press, 2000). doi:10.1201/9781482289343.
153. Goldstein, J. I. et al. Scanning Electron Microscopy and X-Ray Microanalysis. (Springer New York, New York, NY, 2018). doi:10.1007/978-1-4939-6676-9.
154. Gras, S. L., Waddington, L. J. & Goldie, K. N. Transmission Electron Microscopy of Amyloid Fibrils. in 197–214 (2011). doi:10.1007/978-1-60327-223-0_13.
155. Kollmer, M. et al. Cryo-EM structure and polymorphism of Aβ amyloid fibrils purified from Alzheimer's brain tissue. Nat. Commun. **10**, 4760 (2019).
156. Gade Malmos, K. et al. ThT 101: a primer on the use of thioflavin T to investigate amyloid formation. Amyloid **24**, 1–16 (2017).
157. Arosio, P., Knowles, T. P. J. & Linse, S. On the lag phase in amyloid fibril formation. Physical Chemistry Chemical Physics **17**, 7606–7618 (2015).
158. Morris, A. M., Watzky, M. A., Agar, J. N. & Finke, R. G. Fitting Neurological Protein Aggregation Kinetic Data via a 2-Step, Minimal/"Ockham's Razor" Model: The Finke−Watzky Mechanism of Nucleation Followed by Autocatalytic Surface Growth. Biochemistry **47**, 2413–2427 (2008).
159. Watzky, M. A. & Finke, R. G. Transition Metal Nanocluster Formation Kinetic and Mechanistic Studies. A New Mechanism When Hydrogen Is the Reductant: Slow, Continuous Nucleation and Fast Autocatalytic Surface Growth. J. Am. Chem. Soc. **119**, 10382–10400 (1997).
160. Meisl, G. et al. Molecular mechanisms of protein aggregation from global fitting of kinetic models. Nat. Protoc. **11**, 252–272 (2016).

161. Mosmann, T. Rapid colorimetric assay for cellular growth and survival: Application to proliferation and cytotoxicity assays. J. Immunol. Methods **65**, 55–63 (1983).
162. Arunachalam, K. & Sreeja, P. S. MTT Assay Protocol. in 271–276 (2025). doi:10.1007/978-1-0716-4518-5_45.
163. Williams, T. L. & Serpell, L. C. Membrane and surface interactions of Alzheimer's Aβ peptide – insights into the mechanism of cytotoxicity. FEBS J. **278**, 3905–3917 (2011).
164. Qiang, W. & Doherty, K. E. Model Phospholipid Liposomes to Study the β-Amyloid-Peptide-Induced Membrane Disruption. in 355–367 (2018). doi:10.1007/978-1-4939-7811-3_23.
165. Akbarzadeh, A. et al. Liposome: classification, preparation, and applications. Nanoscale Res. Lett. **8**, 102 (2013).
166. Grad, P., Agmo Hernández, V. & Edwards, K. Avoiding artifacts in liposome leakage measurements via cuvette- and liposome-surface modifications. J. Liposome Res. **32**, 237–249 (2022).
167. Bazett-Jones, D. P. & Ottensmeyer, F. P. Phosphorus Distribution in the Nucleosome. Science (1979). **211**, 169–170 (1981).
168. Gilchrist, A. M. et al. Supramolecular methods: the 8-hydroxypyrene-1,3,6-trisulfonic acid (HPTS) transport assay. Supramol. Chem. **33**, 325–344 (2021).
169. Kaddah, S., Khreich, N., Kaddah, F., Charcosset, C. & Greige-Gerges, H. Cholesterol modulates the liposome membrane fluidity and permeability for a hydrophilic molecule. Food and Chemical Toxicology **113**, 40–48 (2018).
170. Bangham, A. D., Standish, M. M. & Watkins, J. C. Diffusion of univalent ions across the lamellae of swollen phospholipids. J. Mol. Biol. **13**, 238-IN27 (1965).
171. Barnadas-Rodríguez, R. & Sabés, M. Factors involved in the production of liposomes with a high-pressure homogenizer. Int. J. Pharm. **213**, 175–186 (2001).
172. Rodríguez, R. B. i & Xamaní, M. S. i. Liposomes Prepared by High-Pressure Homogenizers. in 28–46 (2003). doi:10.1016/S0076-6879(03)67004-7.
173. Stetefeld, J., McKenna, S. A. & Patel, T. R. Dynamic light scattering: a practical guide and applications in biomedical sciences. Biophys. Rev. **8**, 409–427 (2016).
174. Burns, A. & Iliffe, S. Alzheimer's disease. BMJ **338**, b158–b158 (2009).
175. Selkoe, D. J. & Hardy, J. The amyloid hypothesis of Alzheimer's disease at 25 years. EMBO Mol. Med. **8**, 595–608 (2016).
176. Aubrey, L. D. et al. Quantification of amyloid fibril polymorphism by nano-morphometry reveals the individuality of filament assembly. Commun. Chem. **3**, 125 (2020).
177. Hampel, H. et al. The Amyloid-β Pathway in Alzheimer's Disease. Mol. Psychiatry **26**, 5481–5503 (2021).
178. Bai, R., Guo, J., Ye, X.-Y., Xie, Y. & Xie, T. Oxidative stress: The core pathogenesis and mechanism of Alzheimer's disease. Ageing Res. Rev. **77**, 101619 (2022).
179. Litus, E. et al. Serotonin Promotes Serum Albumin Interaction with the Monomeric Amyloid β Peptide. Int. J. Mol. Sci. **22**, 5896 (2021).
180. Luo, J., Wärmländer, S. K. T. S., Gräslund, A. & Abrahams, J. P. Cross-interactions between the Alzheimer Disease Amyloid-β Peptide and Other Amyloid Proteins: A Further Aspect of the Amyloid Cascade Hypothesis. Journal of Biological Chemistry **291**, 16485–16493 (2016).

181. Press-Sandler, O. & Miller, Y. Assessments of the Effect of Neurokinin B on Toxic Aβ Aggregates in Alzheimer's Disease with the Molecular Mechanisms' Action. ACS Chem. Neurosci. **11**, 3418–3429 (2020).
182. Qiu, P. et al. The Eph/ephrin system symphony of gut inflammation. Pharmacol. Res. **197**, 106976 (2023).
183. Martin, C. R., Osadchiy, V., Kalani, A. & Mayer, E. A. The Brain-Gut-Microbiome Axis. Cell. Mol. Gastroenterol. Hepatol. **6**, 133–148 (2018).
184. Liu, X. et al. Tachykinin Neuropeptides and Amyloid β (25–35) Assembly: Friend or Foe? J. Am. Chem. Soc. **144**, 14614–14626 (2022).
185. Severini, C. The Tachykinin Peptide Family. Pharmacol. Rev. **54**, 285–322 (2002).
186. Otsuka, M. & Yoshioka, K. Neurotransmitter functions of mammalian tachykinins. Physiol. Rev. **73**, 229–308 (1993).
187. Steinhoff, M. S., von Mentzer, B., Geppetti, P., Pothoulakis, C. & Bunnett, N. W. Tachykinins and Their Receptors: Contributions to Physiological Control and the Mechanisms of Disease. Physiol. Rev. **94**, 265–301 (2014).
188. Munekata, E., Kubo, K., Tanaka, H. & Osakada, F. Structure-activity studies of heptapeptide derivatives related to substance P, neurokinin A, B and other tachykinins on smooth muscles. Peptides (N.Y.). **8**, 169–173 (1987).
189. Martinez, M., Frank, A. & Hernanz, A. Relationship of interleukin-1β and β2-microglobulin with neuropeptides in cerebrospinal fluid of patients with dementia of the Alzheimer type. J. Neuroimmunol. **48**, 235–240 (1993).
190. Perry, E. K. et al. Neurochemical activities in human temporal lobe related to aging and Alzheimer-type changes. Neurobiol. Aging **2**, 251–256 (1981).
191. Calvo, N., Reiriz, J., Pérez-Navarro, E. & Alberch, J. Tachykinins protect cholinergic neurons from quinolinic acid excitotoxicity in striatal cultures. Brain Res. **740**, 323–328 (1996).
192. Teuchner, B. et al. Secretoneurin and the tachykinins substance P and neurokinin-A/B in NMDA-induced excitotoxicity in the rat retina. Regul. Pept. **165**, 123–127 (2010).
193. Salthun-Lassalle, B., Traver, S., Hirsch, E. C. & Michel, P. P. Substance P, Neurokinins A and B, and Synthetic Tachykinin Peptides Protect Mesencephalic Dopaminergic Neurons in Culture via an Activity-Dependent Mechanism. Mol. Pharmacol. **68**, 1214–1224 (2005).
194. Chen, L.-, Yung, K. & Chan, Y. Neurokinin Peptides and Neurokinin Receptors as Potential Therapeutic Intervention Targets of Basal Ganglia in the Prevention and Treatment of Parkinsons Disease. Curr. Drug Targets **5**, 197–206 (2004).
195. Nässel, D. R., Zandawala, M., Kawada, T. & Satake, H. Tachykinins: Neuropeptides That Are Ancient, Diverse, Widespread and Functionally Pleiotropic. Front. Neurosci. **13**, (2019).
196. Sun, W. et al. Structural insights into the activation of neurokinin 2 receptor by neurokinin A. Cell Discov. **8**, 72 (2022).
197. Claudino dos Santos, J. C., Lima, M. P. P., Brito, G. A. de C. & Viana, G. S. de B. Role of enteric glia and microbiota-gut-brain axis in parkinson disease pathogenesis. Ageing Res. Rev. **84**, 101812 (2023).
198. Thomasi, B. et al. Enteric glia as a player of gut-brain interactions during Parkinson's disease. Front. Neurosci. **17**, (2023).

199. Gasteiger, E. et al. Protein Identification and Analysis Tools on the ExPASy Server. in The Proteomics Protocols Handbook 571–607 (Humana Press, Totowa, NJ, 2005). doi:10.1385/1-59259-890-0:571.
200. Chaudhury, S. et al. Benchmarking and Analysis of Protein Docking Performance in Rosetta v3.2. PLoS One **6**, e22477 (2011).
201. Pettersen, E. F. et al. UCSF Chimera—A visualization system for exploratory research and analysis. J. Comput. Chem. **25**, 1605–1612 (2004).
202. Hosseinzadeh, P. et al. Comprehensive computational design of ordered peptide macrocycles. Science (1979). **358**, 1461–1466 (2017).
203. Huang, J. et al. CHARMM36m: an improved force field for folded and intrinsically disordered proteins. Nat. Methods **14**, 71–73 (2017).
204. McGibbon, R. T. et al. MDTraj: A Modern Open Library for the Analysis of Molecular Dynamics Trajectories. Biophys. J. **109**, 1528–1532 (2015).
205. Phillips, J. C. et al. Scalable molecular dynamics with NAMD. J. Comput. Chem. **26**, 1781–1802 (2005).
206. Heinig, M. & Frishman, D. STRIDE: a web server for secondary structure assignment from known atomic coordinates of proteins. Nucleic Acids Res. **32**, W500–W502 (2004).
207. Wahlström, A., Hugonin, L., Perálvarez-Marín, A., Jarvet, J. & Gräslund, A. Secondary structure conversions of Alzheimer's Aβ(1–40) peptide induced by membrane-mimicking detergents. FEBS J. **275**, 5117–5128 (2008).
208. Perálvarez-Marín, A. et al. Influence of Residue 22 on the Folding, Aggregation Profile, and Toxicity of the Alzheimer's Amyloid β Peptide. Biophys. J. **97**, 277–285 (2009).
209. Côté, S., Laghaei, R., Derreumaux, P. & Mousseau, N. Distinct Dimerization for Various Alloforms of the Amyloid-Beta Protein: $A\beta_{1-40}$, $A\beta_{1-42}$, and $A\beta_{1-40}$ (D23N). J. Phys. Chem. B **116**, 4043–4055 (2012).
210. Singh, P. K. & Maji, S. K. Amyloid-Like Fibril Formation by Tachykinin Neuropeptides and Its Relevance to Amyloid β-Protein Aggregation and Toxicity. Cell Biochem. Biophys. **64**, 29–44 (2012).
211. Yankner, B. A., Duffy, L. K. & Kirschner, D. A. Neurotrophic and Neurotoxic Effects of Amyloid β Protein: Reversal by Tachykinin Neuropeptides. Science (1979). **250**, 279–282 (1990).
212. Mantha, A. K., Moorthy, K., Cowsik, S. M. & Baquer, N. Z. Neuroprotective Role of Neurokinin B (NKB) on β-amyloid (25–35) Induced Toxicity in Aging Rat Brain Synaptosomes: Involvement in Oxidative Stress and Excitotoxicity. Biogerontology **7**, 1–17 (2006).
213. Luo, J. & Abrahams, J. P. Cyclic Peptides as Inhibitors of Amyloid Fibrillation. Chemistry – A European Journal **20**, 2410–2419 (2014).
214. Valls-Comamala, V. et al. The antigen-binding fragment of human gamma immunoglobulin prevents amyloid β-peptide folding into β-sheet to form oligomers. Oncotarget **8**, 41154–41165 (2017).
215. Gazit, E. A possible role for π-stacking in the self-assembly of amyloid fibrils. The FASEB Journal **16**, 77–83 (2002).

216. Kepp, K. P., Robakis, N. K., Høilund-Carlsen, P. F., Sensi, S. L. & Vissel, B. The amyloid cascade hypothesis: an updated critical review. Brain vol. 146 3969–3990 Preprint at https://doi.org/10.1093/brain/awad159 (2023).
217. Francis, P. T., Palmer, A. M., Snape, M. & Wilcock, G. K. The Cholinergic Hypothesis of Alzheimer's Disease: A Review of Progress. J Neurol Neurosurg Psychiatry vol. 66 (1999).
218. Hampel, H. et al. Revisiting the Cholinergic Hypothesis in Alzheimer's Disease: Emerging Evidence from Translational and Clinical Research. The journal of prevention of Alzheimer's disease vol. 6 2–15 Preprint at https://doi.org/10.14283/jpad.2018.43 (2019).
219. Yang, J. et al. Differentiating Ab40 and Ab42 in amyloid plaques with a small molecule fluorescence probe †. https://doi.org/10.1039/d0sc02060e (2020) doi:10.1039/d0sc02060e.
220. Gottfries, C.-G., Frederiksen, O. & Heilig, M. EUROPEAN NEURO-PSYCHOPHARMACOLOGY ELSEVIER Neuropeptides and Alzheimer's Disease. European Neuropsychopharmacology vol. 5 (1995).
221. Yan, X., Ma, Y., Yan, L., Li, S. & Xu, Y. Neuropeptides as Potential Biomarkers in Vascular Dementia. Journal of Integrative Neuroscience vol. 23 Preprint at https://doi.org/10.31083/j.jin2303066 (2024).
222. Terry, A. V. & Buccafusco, J. J. The Cholinergic Hypothesis of Age and Alzheimer's Disease-Related Cognitive Deficits: Recent Challenges and Their Implications for Novel Drug Development. J. Pharmacol. Exp. Ther. **306**, 821–827 (2003).
223. GUO, D. F., SUN, Y. L., HAMET, P. & INAGAMI, T. The angiotensin II type 1 receptor and receptor-associated proteins. Cell Res. **11**, 165–180 (2001).
224. Kehoe, P. G. The Coming of Age of the Angiotensin Hypothesis in Alzheimer's Disease: Progress Toward Disease Prevention and Treatment? Journal of Alzheimer's Disease **62**, 1443–1466 (2018).
225. Wright, J. W., Kawas, L. H. & Harding, J. W. The development of small molecule angiotensin IV analogs to treat Alzheimer's and Parkinson's diseases. Progress in Neurobiology vol. 125 26–46 Preprint at https://doi.org/10.1016/j.pneurobio.2014.11.004 (2015).
226. Bai, H.-Y. et al. Angiotensin II and Amyloid-β Synergistically Induce Brain Vascular Smooth Muscle Cell Senescence. Am. J. Hypertens. **34**, 552–562 (2021).
227. Ashby, E. L., Miners, J. S., Kehoe, P. G. & Love, S. Effects of Hypertension and Anti-Hypertensive Treatment on Amyloid-β (Aβ) Plaque Load and Aβ-Synthesizing and Aβ-Degrading Enzymes in Frontal Cortex. Journal of Alzheimer's Disease **50**, 1191–1203 (2016).
228. Zhu, D. et al. Central Angiotensin II Stimulation Promotes β Amyloid Production in Sprague Dawley Rats. PLoS One **6**, e16037 (2011).
229. Takeda, S. & Morishita, R. Angiotensin Receptor Blocker Protects Alzheimer's Disease Brain From Ischemic Insult. Am. J. Hypertens. **30**, 110–111 (2017).
230. Takeda, S. et al. Angiotensin Receptor Blocker Prevented β-Amyloid-Induced Cognitive Impairment Associated With Recovery of Neurovascular Coupling. Hypertension **54**, 1345–1352 (2009).

231. Perálvarez-Marín, A. et al. Influence of residue 22 on the folding, aggregation profile, and toxicity of the Alzheimer's amyloid β peptide. Biophys. J. **97**, 277–285 (2009).
232. Gomara, M. J. et al. Peptide Assembly on the Membrane Determines the HIV-1 Inhibitory Activity of Dual-Targeting Fusion Inhibitor Peptides. Sci. Rep. https://doi.org/10.1038/s41598-019-40125-4 (2019) doi:10.1038/s41598-019-40125-4.
233. London, N., Raveh, B., Cohen, E., Fathi, G. & Schueler-Furman, O. Rosetta FlexPepDock web server - High resolution modeling of peptide-protein interactions. Nucleic Acids Res. **39**, (2011).
234. Lyskov, S. et al. Serverification of Molecular Modeling Applications: The Rosetta Online Server That Includes Everyone (ROSIE). PLoS One **8**, (2013).
235. Raveh, B., London, N. & Schueler-Furman, O. Sub-angstrom modeling of complexes between flexible peptides and globular proteins. Proteins: Structure, Function and Bioinformatics **78**, 2029–2040 (2010).
236. Vivekanandan, S., Brender, J. R., Lee, S. Y. & Ramamoorthy, A. A partially folded structure of amyloid-beta(1-40) in an aqueous environment. Biochem. Biophys. Res. Commun. **411**, 312–316 (2011).
237. Coles, M., Bicknell, W., Watson, A. A., Fairlie, D. P. & Craik, D. J. Solution Structure of Amyloid-Peptide(1-40) in a Water-Micelle Environment. Is the Membrane-Spanning Domain Where We Think It Is? †, ‡. (1998).
238. Fu, Z. et al. An electrostatic cluster guides Aβ40 fibril formation in sporadic and Dutch-type cerebral amyloid angiopathy. J. Struct. Biol. **216**, (2024).
239. Santoro, A., Grimaldi, M., Buonocore, M., Stillitano, I. & D'Ursi, A. M. Exploring the early stages of the amyloid aβ(1–42) peptide aggregation process: An nmr study. Pharmaceuticals **14**, (2021).
240. Tomaselli, S. et al. The α-to-β conformational transition of Alzheimer's Aβ-(1-42) peptide in aqueous media is reversible: A step by step conformational analysis suggests the location of β conformation seeding. ChemBioChem **7**, 257–267 (2006).
241. Gremer, L. et al. Fibril structure of amyloid-β(1–42) by cryo–electron microscopy. Science (1979). **358**, 116–119 (2017).
242. Adams, R. et al. Extending the half-life of a fab fragment through generation of a humanized anti-human serum albumin Fv domain: An investigation into the correlation between affinity and serum half-life. MAbs **8**, 1336–1346 (2016).
243. Abramson, J. et al. Accurate structure prediction of biomolecular interactions with AlphaFold 3. Nature **630**, 493–500 (2024).
244. Klunk, W. E., Pettegrew, J. W. & Abraham3, D. J. Quantitative Evaluation of Congo Red Binding to Amyloid-like Proteins with a Beta-pleated Sheet Conformation. Klunk, W. E., Pettegrew, J. W., & Abraham, D. J. (1989). Quantitative evaluation of congo red binding to amyloid-like proteins with a beta-pleated sheet conformation. The journal of histochemistry and cytochemistry **37**, 1273–1281 (1989).
245. Nutini, A. Amyloid oligomers and their membrane toxicity - A perspective study. Progress in Biophysics and Molecular Biology vol. 187 9–20 Preprint at https://doi.org/10.1016/j.pbiomolbio.2024.01.002 (2024).

246. Peters, C., Bascuñán, D., Opazo, C. & Aguayo, L. G. Differential Membrane Toxicity of amyloid-β Fragments by Pore Forming Mechanisms. Journal of Alzheimer's Disease **51**, 689–699 (2016).
247. Serra-Batiste, M. et al. Aβ42 assembles into specific β-barrel pore-forming oligomers in membrane-mimicking environments. Proc. Natl. Acad. Sci. U. S. A. **113**, 10866–10871 (2016).
248. Banerjee, S., Hashemi, M., Zagorski, K. & Lyubchenko, Y. L. Cholesterol in Membranes Facilitates Aggregation of Amyloid β Protein at Physiologically Relevant Concentrations. ACS Chem. Neurosci. **12**, 506–516 (2021).
249. Nguyen, T. H., Nguyen, P. H., Ngo, S. T. & Derreumaux, P. Effect of Cholesterol Molecules on Aβ1-42 Wild-Type and Mutants Trimers. Molecules **27**, 1395 (2022).
250. Brown, A. M. & Bevan, D. R. Molecular Dynamics Simulations of Amyloid β -Peptide (1-42): Tetramer Formation and Membrane Interactions. Biophys. J. **111**, 937–949 (2016).
251. Picón-Pagès, P. et al. Human Albumin Impairs Amyloid β-peptide Fibrillation Through its C-terminus: From docking Modeling to Protection Against Neurotoxicity in Alzheimer's disease. Comput. Struct. Biotechnol. J. **17**, 963–971 (2019).
252. Grammatopoulos, T. N., Outeiro, T. F., Hyman, B. T. & Standaert, D. G. Angiotensin II protects against α-synuclein toxicity and reduces protein aggregation in vitro. Biochem. Biophys. Res. Commun. **363**, 846–851 (2007).
253. Yakovleva, T. et al. Dysregulation of dynorphins in Alzheimer disease. Neurobiol. Aging **28**, 1700–1708 (2007).
254. Lundin, S. K. et al. Association between risk of Alzheimer's disease and related dementias and angiotensin receptor Ⅱ blockers treatment for individuals with hypertension in high-volume claims data. EBioMedicine **109**, 105378 (2024).
255. Zou, K. et al. Angiotensin-Converting Enzyme Converts Amyloid β-Protein 1–42 ($A\beta_{1-42}$) to $A\beta_{1-40}$, and Its Inhibition Enhances Brain Aβ Deposition. The Journal of Neuroscience **27**, 8628–8635 (2007).
256. Miners, J. S. et al. Aβ-degrading enzymes in Alzheimer's disease. in Brain Pathology vol. 18 240–252 (2008).
257. Zhu, D. et al. Central angiotensin II stimulation promotes β amyloid production in Sprague Dawley rats. PLoS One **6**, (2011).
258. Park, L. et al. Brain Perivascular Macrophages Initiate the Neurovascular Dysfunction of Alzheimer Aβ Peptides. Circ. Res. **121**, 258–269 (2017).
259. Kehoe, P. G., Wong, S., Al Mulhim, N., Palmer, L. E. & Miners, J. S. Angiotensin-converting enzyme 2 is reduced in Alzheimer's disease in association with increasing amyloid-β and tau pathology. Alzheimers Res. Ther. **8**, (2016).
260. Kehoe, P. G., Hibbs, E., Palmer, L. E. & Miners, J. S. Angiotensin-III is Increased in Alzheimer's Disease in Association with Amyloid-β and Tau Pathology. Journal of Alzheimer's Disease **58**, 203–214 (2017).
261. Habibnia, M., Catalina-Hernandez, E., Barnadas-Rodríguez, R. & Peralvarez-Marin, A. Electrostatic control of membrane disruption and amorphous coaggregation by dynorphin A variants. Biochem. Biophys. Res. Commun. **827**, 154059 (2026).
262. BAKALKIN, G. Y. et al. Amino acid sequence pattern in the regulatory peptides. Int. J. Pept. Protein Res. **38**, 505–510 (1991).

263. Yakovleva, T. et al. Dysregulation of dynorphins in Alzheimer disease. Neurobiol. Aging **28**, 1700–1708 (2007).
264. Fischli, W., Goldstein, A., Hunkapiller, M. W. & Hood, L. E. Two “big” dynorphins from porcine pituitary. Life Sci. **31**, 1769–1772 (1982).
265. Fischli, W., Goldstein, A., Hunkapiller, M. W. & Hood, L. E. Isolation and amino acid sequence analysis of a 4,000-dalton dynorphin from porcine pituitary. Proceedings of the National Academy of Sciences **79**, 5435–5437 (1982).
266. Ménard, C., Herzog, H., Schwarzer, C. & Quirion, R. Possible Role of Dynorphins in Alzheimer’s Disease and Age-Related Cognitive Deficits. Neurodegener. Dis. **13**, 82–85 (2014).
267. Hauser, K. F., Foldes, J. K. & Turbek, C. S. Dynorphin A (1–13) Neurotoxicity in Vitro: Opioid and Non-Opioid Mechanisms in Mouse Spinal Cord Neurons. Exp. Neurol. **160**, 361–375 (1999).
268. Marinova, Z. et al. Translocation of Dynorphin Neuropeptides across the Plasma Membrane. Journal of Biological Chemistry **280**, 26360–26370 (2005).
269. Hugonin, L., Vukojević, V., Bakalkin, G. & Gräslund, A. Membrane leakage induced by dynorphins. FEBS Lett. **580**, 3201–3205 (2006).
270. Hugonin, L., Vukojević, V., Bakalkin, G. & Gräslund, A. Calcium influx into phospholipid vesicles caused by dynorphin neuropeptides. Biochimica et Biophysica Acta (BBA) - Biomembranes **1778**, 1267–1273 (2008).
271. Alvero-Gonzalez, L. M. et al. Probing electrophysiological activity of amphiphilic Dynorphin A in planar neutral membranes reveals both ion channel-like activity and neuropeptide translocation. Bioelectrochemistry **154**, 108527 (2023).
272. Bakalkin, G. et al. Prodynorphin Mutations Cause the Neurodegenerative Disorder Spinocerebellar Ataxia Type 23. The American Journal of Human Genetics **87**, 593–603 (2010).
273. Wu, F. et al. Spinocerebellar ataxia type 23 (SCA23): a review. J. Neurol. **268**, 4630–4645 (2021).
274. Madani, F. et al. Perturbations of model membranes induced by pathogenic dynorphin A mutants causing neurodegeneration in human brain. Biochem. Biophys. Res. Commun. **411**, 111–114 (2011).
275. Smeets, C. J. L. M. et al. Altered secondary structure of Dynorphin A associates with loss of opioid signalling and NMDA-mediated excitotoxicity in SCA23. Hum. Mol. Genet. ddw130 (2016) doi:10.1093/hmg/ddw130.
276. Lind, J., Gräslund, A. & Mäler, L. Membrane Interactions of Dynorphins ′. Biochemistry **45**, 15931–15940 (2006).
277. Björnerås, J., Gräslund, A. & Mäler, L. Membrane Interaction of Disease-Related Dynorphin A Variants. Biochemistry **52**, 4157–4167 (2013).
278. Catalina-Hernandez, E., Lopez-Martin, M., Aguilella-Arzo, M. & Peralvarez-Marin, A. Membrane disruption potential of endogenous opioid neuropeptide Dynorphin A and related clinical variants. Int. J. Biol. Macromol. **316**, 144567 (2025).
279. Jo, S., Kim, T., Iyer, V. G. & Im, W. CHARMM-GUI: A web-based graphical user interface for CHARMM. J. Comput. Chem. **29**, 1859–1865 (2008).

280. Wu, E. L. et al. CHARMM-GUI Membrane Builder toward realistic biological membrane simulations. J. Comput. Chem. **35**, 1997–2004 (2014).
281. Lee, J. et al. CHARMM-GUI Input Generator for NAMD, GROMACS, AMBER, OpenMM, and CHARMM/OpenMM Simulations Using the CHARMM36 Additive Force Field. J. Chem. Theory Comput. **12**, 405–413 (2016).
282. Kutzner, C., Grubmüller, H., De Groot, B. L. & Zachariae, U. Computational Electrophysiology: The Molecular Dynamics of Ion Channel Permeation and Selectivity in Atomistic Detail. Biophys. J. **101**, 809 (2011).
283. Bekker, H. et al. Gromacs - a parallel computer for molecular dynamics simulations. PHYSICS COMPUTING '92 252–256 (1993).
284. Van Der Spoel, D. et al. GROMACS: fast, flexible, and free. J. Comput. Chem. **26**, 1701–1718 (2005).
285. Berendsen, H. J. C., van der Spoel, D. & van Drunen, R. GROMACS: A message-passing parallel molecular dynamics implementation. Comput. Phys. Commun. **91**, 43–56 (1995).
286. Páll, S., Abraham, M. J., Kutzner, C., Hess, B. & Lindahl, E. Tackling Exascale Software Challenges in Molecular Dynamics Simulations with GROMACS. Lecture Notes in Computer Science (including subseries Lecture Notes in Artificial Intelligence and Lecture Notes in Bioinformatics) **8759**, 3–27 (2015).
287. Lindahl, E., Hess, B. & van der Spoel, D. GROMACS 3.0: A package for molecular simulation and trajectory analysis. J. Mol. Model. **7**, 306–317 (2001).
288. Abraham, M. J. et al. GROMACS: High performance molecular simulations through multi-level parallelism from laptops to supercomputers. SoftwareX **1–2**, 19–25 (2015).
289. Hess, B., Kutzner, C., Van Der Spoel, D. & Lindahl, E. GROMACS 4: Algorithms for Highly Efficient, Load-Balanced, and Scalable Molecular Simulation. J. Chem. Theory Comput. **4**, 435–447 (2008).
290. Pronk, S. et al. GROMACS 4.5: a high-throughput and highly parallel open source molecular simulation toolkit. Bioinformatics **29**, 845–854 (2013).
291. Kluyver, T. et al. Jupyter Notebooks – a publishing format for reproducible computational workflows. in 20th International Conference on Electronic Publishing (01/01/16) (eds. Loizides, F. & Scmidt, B.) 87–90 (IOS Press, 2016). doi:10.3233/978-1-61499-649-1-87.
292. Hunter, J. D. Matplotlib: A 2D Graphics Environment. Comput. Sci. Eng. **9**, 90–95 (2007).
293. Humphrey, W., Dalke, A. & Schulten, K. VMD: Visual molecular dynamics. J. Mol. Graph. **14**, 33–38 (1996).
294. Gomara, M. J. et al. Peptide Assembly on the Membrane Determines the HIV-1 Inhibitory Activity of Dual-Targeting Fusion Inhibitor Peptides. Sci. Rep. **9**, 3257 (2019).
295. Hugonin, L., Barth, A., Gräslund, A. & Perálvarez-Marín, A. Secondary structure transitions and aggregation induced in dynorphin neuropeptides by the detergent sodium dodecyl sulfate. Biochimica et Biophysica Acta (BBA) - Biomembranes **1778**, 2580–2587 (2008).
296. Perini, D. A., Aguilella-Arzo, M., Alcaraz, A., Perálvarez-Marín, A. & Queralt-Martín, M. Dynorphin A induces membrane permeabilization by formation of proteolipidic pores. Insights from electrophysiology and computational simulations. Comput. Struct. Biotechnol. J. **20**, 230–240 (2022).

297. Hetz, C. Adapting the proteostasis capacity to sustain brain healthspan. Cell **184**, 1545–1560 (2021).
298. Jászberényi, M., Thurzó, B., Jayakumar, A. R. & Schally, A. V. The Aggravating Role of Failing Neuropeptide Networks in the Development of Sporadic Alzheimer's Disease. Int. J. Mol. Sci. **25**, 13086 (2024).
299. Bloom, G. S. Amyloid-β and Tau. JAMA Neurol. **71**, 505 (2014).
300. Bieschke, J. Natural Compounds May Open New Routes to Treatment of Amyloid Diseases. Neurotherapeutics **10**, 429–439 (2013).